Title

Modulation of turn-related activity in the superior colliculus by ongoing behavioral and cognitive dynamics

ISBN

9798247945994

Author

Wilhite, Cameron

Publication Date

2026-06-03

Peer reviewed|Thesis/dissertation

MODULATION OF TURN-RELATED ACTIVITY IN THE SUPERIOR COLLICULUS BY ONGOING BEHAVIORAL AND COGNITIVE DYNAMICS

by
Cameron Wilhite

DISSERTATION
Submitted in partial satisfaction of the requirements for degree of
DOCTOR OF PHILOSOPHY

in

Neuroscience

in the

GRADUATE DIVISION
of the
UNIVERSITY OF CALIFORNIA, SAN FRANCISCO

Approved:

DocuSigned by:
Michael Stryker
15DFF21E2A5440C...
Chair

DocuSigned by:
Massimo Scanziani

DocuSigned by:
Loren Frank

DocuSigned by:
Christoph Kirst
FC0925D4E50F484...

Committee Members

ACKNOWLEDGEMENTS

Making it through a Ph.D. requires a lot of help. There are several people I would like to thank who have helped me more than most.

My most special thanks goes to Massimo Scanziani, for taking me into his lab and teaching me how to do science, how to write, and how to think deeply about scientific problems.

I also owe a great debt to Loren Frank, who opened my eyes to how the brain thinks about future possibilities, along with helping me see my results in a broader context.

For helpful discussions and suggestions along the way, I would like to thank my committee members Michael Stryker and Christoph Kirst, as well as other members of the Scanziani and Frank labs, past and present, including: Yuta Senzai, Satoru Miura, Riccardo Beltramo, Sarah Ruediger, Guy Bouvier, Josh Brenner, Gal Atlan, Amir Levi, Chinmay Purandare, Josue Regalado, Xinxin Ge, Moritz Stingl, Sophie Grutzner, Alison Comrie, Abhilasha Joshi, and Kyu Hyun Lee. For technical assistance, I would like to thank Leo Ruan and Ying Wu. I would also like to thank Pooja Saraf, Madan Mukundan, Patricia Veitch, and Lucita Nacionales for making this process unfold as seamless as possible.

I am grateful to my advisors from Tucson, Stephen Cowen and Russell Witte, for introducing me to neuroscience and to the hippocampal community.

Most importantly, I would like to thank my mother Rose, father Mike, and brothers Quin and Trey for their unwavering support and encouragement. Lastly, I would like to thank my partner Deanna, for whose love I am forever grateful.

MODULATION OF TURN-RELATED ACTIVITY IN THE SUPERIOR COLLICULUS BY ONGOING BEHAVIORAL AND COGNITIVE DYNAMICS

Cameron Alex Wilhite

ABSTRACT

The superior colliculus (SC) is a highly conserved sensorimotor midbrain structure implicated in the control of orienting movements. Yet, despite decades of research, it remains unclear how neural activity in this structure unfolds during internally-driven behaviors like spatial navigation, when orienting movements need to be coordinated with other ongoing behavioral and cognitive processes. This dissertation aims to address this gap.

By recording from neurons in the intermediate and deep motor layers of the SC (dSC) of mice navigating a Y-maze, it is demonstrated that: 1) About 30% of neurons fire selectively for left or right turns at the maze bifurcation (left- or right-preferring 'turn cells'). 2) Turn cell activity is rhythmically modulated during locomotion, firing in-phase with the ongoing stepping cycle of the animal, such that left and right turn cells fire at opposite phases of the stepping cycle. 3) Simultaneous recordings from turn cells and populations of hippocampal place cells reveal that turn cell activity is also modulated in directional coordination with hippocampal representations of possible future paths (i.e., hippocampal 'sweeps'). Critically, hippocampal sweeps prior to the bifurcation can predict turn cell activity at the bifurcation. 4) Consistent with an influence of hippocampal sweeps on turn cell activity, sweeps are associated with biases in the animal's trajectory toward the represented path. 5) The remaining 70% of neurons in the dSC either exhibit no turn-

selective firing at the maze bifurcation or exhibit turn-selective firing that depends on the animal's starting position on the maze and its upcoming trajectory. Notably, these neurons can exhibit firing that encodes trajectories between two specific maze arms or trajectories converging on a single maze arm.

Thus, during navigation, neural activity in the motor layers of the SC reflects not only multiple aspects of ongoing behavior—such as turns, steps, and trajectories—but also ongoing cognitive processes, such as internal representations of possible future paths. These results are consistent with the interpretation that the SC functions as a 'movement template', organized as an entire sequence of goal-directed movements, which can be used by higher brain centers for intentional actions (Ewert, 1970; Ingle, 1970; Schaefer, 1970). Drawing on 19th-century psychology, particularly the notion of 'ideo-motor' action (Carpenter, 1852; James, 1890), it is further hypothesized that the SC plays a central role in transforming cognitive inputs into orienting movements, thereby linking thoughts to actions.

References

Carpenter, W. B. (1852). On the influence of suggestion in modifying and directing muscular movement, independently of volition. *Royal Institution of Great Britain*.

Ewert, J. P. (1970). Neural mechanisms of prey-catching and avoidance behavior in the toad (Bufo bufo L.). *Brain, Behavior and Evolution*, *3*(1), 36–56.

Ingle, D. (1970). Visuomotor functions of the frog optic tectum. *Brain, Behavior and Evolution*, *3*(1), 57–71.

James, W. (1890). *The Principles of Psychology (Vol. 2)*. Henry Holt & Company.

Schaefer, K. P. (1970). Unit analysis and electrical stimulation in the optic tectum of rabbits and cats. *Brain, Behavior and Evolution*, *3*(1), 222–240.

TABLE OF CONTENTS

LIST OF FIGURES

CHAPTER 2:

CHAPTER 3:

CHAPTER 1: THE SUPERIOR COLLICULUS AS A MOTOR OUTPUT STRUCTURE FOR ORIENTING

Introduction

In January of 1870, a young ophthalmologist named E. Adamük published a study that would influence neuroscience for decades to come. Working in anesthetized cats, Adamük applied electrical stimulation to a small structure at the roof of the midbrain known as the *corpora quadrigemina*, a structure that had been described previously (Soemmering, 1778; Willis, 1664) but whose function was unknown. What Adamük found was simple yet striking: stimulation of the right side of this structure, particularly the anterior part, triggered both eyes to move to the left, and stimulation of the left side, also the anterior part, triggered both eyes to move to the right:

> The main finding of these experiments is that both eyes share a common motor innervation, which originates from the anterior colliculi [superior colliculi] of the corpora quadrigemina. The right one of these colliculi governs the movements of both eyes to the left, and the left one governs those of both eyes to the right. By stimulating various points of each colliculus, one can elicit a great variety of movements, but always in both eyes simultaneously and in the same direction. If stimulation is prolonged, the head also turns in the same direction as the eyes.

More than 150 years ago, Adamük discovered the motor function of the superior colliculus (SC), providing some of the earliest direct evidence that this structure is involved in the generation of orienting movements. Adamük titled his report *Über die Innervation der Augenbewegungen*, or *On the Innervation of Eye Movements,* publishing it in two pages (Adamük, 1870).

Since Adamük, more than a century and a half of research across several species has established the SC as a core motor output structure in the organization and control of orienting movements. Yet, despite this extensive research, surprisingly little is known

about how this structure operates during freely-moving, naturalistic behaviors, when orienting movements need to be coordinated with other ongoing motor and cognitive processes. This first chapter therefore has two goals: to introduce the SC as a motor output structure for orienting, and to highlight this critical gap in our understanding of how it operates.

1.1 Inputs and outputs of the SC

The mammalian SC, or optic tectum in non-mammalian vertebrates, is a highly-conserved sensorimotor structure located at the roof of the midbrain. The SC is a layered structure, commonly divided into two parts: a visuosensory part confined to the superficial layers (sSC) and a motor part spanning the intermediate and deep layers (dSC) (Basso & May, 2017). The sSC receives direct input from the retina and sends projections to the dSC, which in turn projects to brainstem motor nuclei that innervate muscles involved in orienting (May, 2006). Thus, the SC is situated very close to the sensorimotor periphery, sitting just one synapse from the retina and two synapses from the muscles involved in orienting.

1.2 Lesion studies

Given its inputs and outputs, early lesion studies demonstrated that the SC supports visually-guided orienting behaviors. Sprague and Meikle found that cats with unilateral SC lesions were blind to stimuli in the contralateral visual field and had motor deficits concerning orienting movements of the eyes and head (Sprague & Meikle, 1965). Similarly, Schneider found that hamsters with unilateral SC lesions were unable to orient toward objects presented in the contralateral visual field, while bilateral lesions abolished their ability to orient toward objects entirely (Schneider, 1969). Together, these lesion

studies provided early evidence that the SC is necessary for orienting toward external (visual) stimuli.

1.3 Stimulation studies

More than 70 years after Adamük first stimulated the SC to evoke contraversive eye movements, Apter (Apter, 1945, 1946) extended this work by demonstrating that the surface of the SC (i.e., the superficial or sSC) contains a sensory map of the contralateral visual field, and that activating a given point on that map evokes eye movements toward the corresponding location in visual space. To establish this, Apter first mapped the projection from the retina to the SC in anesthetized cats by activating the retina with small spots of light presented at precise locations in the visual field and recording the evoked potentials on the SC surface (Apter, 1945). Apter then demonstrated that chemically activating different points on the SC surface evoked eye movements toward the corresponding location of the visual field (Apter, 1946). This tight correspondence between the location of sensory input and its evoked motor output provided early evidence that the SC is topographically organized with its sensory and motor maps aligned.

Similarly, in head-fixed primates, both Robinson as well as Schiller and Stryker used electrical stimulation in the SC to demonstrate that the direction and amplitude of evoked eye movements depend on the site of stimulation (Robinson, 1972; Schiller & Stryker, 1972), and that this motor map is aligned with the visual map (Schiller & Stryker, 1972). Furthermore, this work demonstrated that the stimulus threshold for evoking eye movements was substantially lower in the dSC compared to the sSC (Schiller & Stryker, 1972), consistent with the dSC serving as a motor output channel for orienting.

While the stimulation studies outlined above have primarily focused on eye movements, Adamük found that SC stimulation also caused the head to turn in the same direction as the eyes (Adamük, 1870), suggesting that the SC may be involved in coordinating orienting movements more broadly. Consistent with this view, stimulation studies in rodents using electrical (Sahibzada et al., 1986) and optogenetic approaches (Masullo et al., 2019; Zahler et al., 2023)—including activation of genetically-defined neurons that project along the tecto-spinal tract (Masullo et al., 2019)—have shown that SC stimulation evokes head turns and that the direction and amplitude of evoked head turns depend on the site of stimulation. Thus, the SC drives both eye and head movements, potentially through the same output channels (Zahler et al., 2023), for the coordinated control of orienting.

In line with these reports, various studies have found that prolonged SC stimulation can drive much longer sequences of orienting behaviors involving the entire body. In rabbits and cats, SC stimulation can elicit sequences of orienting movements that involve the ears, head, body, and limbs (Schaefer, 1970). Likewise, prolonged stimulation of the optic tectum elicits prey catching sequences in toads and frogs (Ewert, 1970, 1974; Ingle, 1970) and triggers bouts of locomotion and steering in lampreys (Saitoh et al., 2007). Prolonged stimulation is thought to mimic a sustained visual stimulus, which may evoke goal-directed movements toward the fictive target (Saitoh et al., 2007).

Thus, the SC contains sensorimotor maps that drive orienting movements of a specific direction and size. Moreover, the SC may play a role not only in generating

discrete orienting movements, but also in integrating them into coordinated sequences of action.

1.4 Recording studies

Given that SC stimulation evokes orienting movements, multiple groups in the 1970s began recording from SC neurons in alert, head-fixed monkeys making eye movements to visual stimuli. Of note, Wurtz and Goldberg, Schiller and Koerner, and Schiller and Stryker found that neurons in the dSC of rhesus monkeys discharged in association with eye movements of a specific direction and size (Schiller & Koerner, 1971; Schiller & Stryker, 1972; Wurtz & Goldberg, 1971, 1972). Notably, consistent with the stimulation studies above, these neurons discharged preferentially for contraversive eye movements relative to the recorded dSC hemisphere.

In rodents, recent studies have also demonstrated that neurons in the dSC discharge in association with head-body movements (i.e., turns) of a specific direction. Felsen and Mainen found that, in rats performing an odor-guided nose-poke task in which animals were required to sample an odor and then turn to an adjacent reward port, dSC neurons discharged preferentially in association with left or right turns (Felsen & Mainen, 2008, 2012). Similarly, studies in freely-moving rodents have shown that dSC neurons, including genetically-defined neurons that project along the tecto-spinal tract (Masullo et al., 2019), increase their activity in association with left or right head and body turns (Cooper et al., 1998; Rose, 1985; Senzai & Scanziani, 2024; Sharp et al., 2025; Wilson et al., 2018). As in primates, most neurons in the rodent dSC exhibit firing that is selective for contraversive turns.

In summary, neurons in the dSC discharge in association with orienting movements of specific directions, with a bias for contraversive movements relative to the recorded hemisphere.

1.5 Other sensory and motor inputs to the SC

In addition to input from the retina, the sSC also receives input from visual cortical regions, including inputs from V1 and higher visual areas (Harvey & Worthington, 1990; J. S. Lund et al., 1975; R. D. Lund, 1964; Olavarria & Van Sluyters, 1982). The dSC, in contrast, receives input from non-visual sensory areas, including somatosensory inputs from the trigeminal complex and S1/barrel cortex (Castro-Alamancos & Favero, 2016; Huerta et al., 1981; Killackey & Erzurumlu, 1981; Wise & Jones, 1977), as well as auditory inputs from the inferior colliculus and auditory cortex (Butler et al., 2018; Edwards et al., 1979; K Harting & Van Lieshout, 2000; Paula-Barbosa & Sousa-Pinto, 1973). Given these inputs, cells in the dSC have been shown to exhibit responses to tactile and auditory stimuli (Meredith & Stein, 1986). Interestingly, these responses are also organized into topographic maps of tactile and auditory space that are spatially aligned with the visual maps residing in the superficial layers (Dräger & Hubel, 1976; Finlay et al., 1978; Knudsen & Konishi, 1978; Palmer & King, 1982). In addition to these sensory inputs, the dSC also receives direct input from multiple motor-associated regions, such as the motor cortex and SNr (Fries, 1985; Graybiel, 1978)

Thus, beyond direct input from the retina, the SC receives substantial input from multiple sensory and motor areas across the neuraxis, indicating that it functions as a hub for general sensorimotor integration and transformation (Meredith & Stein, 1986).

1.6 Role of the SC in higher cognitive functions

The research presented thus far has established the SC as a sensorimotor structure involved in stimulus-guided orienting, consistent with its inputs and outputs. However, the SC also receives input from higher-order cortical areas such as the secondary motor cortex, retrosplenial cortex, and anterior cingulate cortex (Campagner et al., 2023; Duan, Pan, et al., 2021; Foreman & Stevens, 1987), suggesting a role for this structure in integrating cognitive inputs related to orienting.

Consistent with this integrative role, many studies have observed preparatory activity in the dSC that ramps up prior to orienting movements. For example, Munoz and Wurtz identified 'buildup' cells in the primate dSC that exhibit ramping activity hundreds of milliseconds before eye movements (Munoz & Wurtz, 1995). Similarly, in rodents, dSC neurons have been shown to increase their firing prior to the onset of head turns (Felsen & Mainen, 2008, 2012; Senzai & Scanziani, 2024; Sharp et al., 2025). Such preparatory activity has been shown to underlie processes that intervene between sensation and action including shifts of attention and decision making (Basso & May, 2017).

Related to attention, it has been theorized that the neurons involved in preparing orienting movements are also those that control shifts of attention (Rizzolatti et al., 1987). Consistent with this hypothesis, recordings from buildup cells in the dSC of head-fixed monkeys revealed responses that were modulated with the intention to make eye movements toward specified locations in visual space (Kustov & Robinson, 1996). Thus, the neural mechanisms controlling orienting movements may overlap with those underlying visuospatial attention.

Related to decision-making, Duan et al. found that, in rats performing a nose-poke task requiring them to decide to orient either toward or away from an adjacent reward port based on audio-visual cues, dSC neurons began to ramp up and encode animals' choice prior to neurons in frontal cortical regions implicated in motor preparation. Such early encoding of choice suggests that activity in the dSC may in fact lead the decision-making process (Duan, Pagan, et al., 2021).

Furthermore, the SC has been shown to play a role in higher-order cognitive processes, independent of its role in spatial orienting and attention. For example, recent experiments in monkeys performing a visual categorization task have shown that SC neurons, including those in the intermediate layers, exhibit robust encoding of abstract visual categories (Peysakhovich et al., 2024). Importantly, the visual categorization task required monkeys to maintain central gaze fixation and report their decisions with manual responses and not eye movements. These results suggest that the SC may play a key role in higher-order cognition, independent of its role in spatial orienting.

Taken together, these results indicate that dSC activity is modulated not only in association with overt orienting movements, but also in association with internal cognitive processes such as spatial attention, decision making, and abstract categorization.

1.7 Dissertation overview

Since Adamük's original study, results from over 150 years of research across multiple species have established the SC as a core motor output structure in the generation and control of orienting movements. Furthermore, growing evidence suggests that the SC plays a key role in higher-order cognitive processes.

Yet, as the literature above demonstrates, the SC has been primarily studied in head-fixed or movement-restricted animals performing orienting movements in response to external stimuli. Accordingly, little is known about how motor-related activity in the SC unfolds during freely-moving, internally-driven behaviors like spatial navigation, when orienting movements need to be coordinated with other ongoing behavioral processes and guided by the animal's internal goals and plans.

This dissertation aims to address this gap. **Chapter 2** examines whether turn-related activity in the dSC is coordinated with other aspects of ongoing behavior, specifically locomotor stepping during navigation. We discover that, in mice navigating a Y-maze, turn-related activity in the dSC is tightly phase-locked to the ongoing stepping rhythm of the animal, such that neurons selective for left and right turns at the maze bifurcation (left- or right-preferring 'turn cells') fire at opposite phases of the stepping cycle. Notably, this phase opposition is already evident during straight locomotion, before the animal initiates a turn. By aligning the activity of left and right turn cells to opposite phases of the stepping cycle, the SC may create alternating windows of opportunity for left and right turns, facilitating the seamless execution of turns during locomotion. **Chapter 3** investigates whether dSC turn cell activity is coordinated with the internal cognitive processes of the navigating animal. We reveal that turn cell activity is modulated in coordination with mental simulations of spatial possibilities as decoded from the hippocampal navigation system. Specifically, hippocampal representations of possible left or right future paths predict increased firing rates of turn cells with matching left or right turn preference. This coordination between the hippocampus and the SC may provide a potential pathway for mental simulations of possible futures (i.e., plans) to guide

actions. **Chapter 4** examines the extent to which dSC activity is modulated by the animal's starting position on the maze and its upcoming trajectory. We find that many neurons in the dSC exhibit spatially selective, trajectory-dependent firing that goes beyond simple turn direction selectivity. Lastly, **Chapter 5** discusses these findings alongside two existing theories: one from neuroscience concerning the function of the SC as a 'movement template' organized as a sequence of goal-directed movements (Ewert, 1970; Ingle, 1970; Schaefer, 1970), and one from psychology concerning 'ideo-motor' action, the principle that the mere thought of a movement immediately triggers the movement itself (Carpenter, 1852; James, 1890). We advance a hypothesis of SC function that integrates these two frameworks and conclude with a list of outstanding questions for future work.

The central takeaway of this dissertation is that orienting-related activity in the SC, possibly one of the best understood motor outputs of this structure, is highly integrated with the ongoing behavior and cognitive state of the organism as it navigates through its world.

References

Adamük, E. (1870). Über die Innervation der Augenbewegungen. *Zbl. Med. Wiss.*, *8*, 65–67.

Apter. (1945). Projection of the retina on superior colliculus of cats. *Journal of Neurophysiology*, *8*(2), 123–134.

Apter. (1946). Eye movements following strychninization of the superior colliculus of cats. *Journal of Neurophysiology*, *9*(2), 73–86.

Basso, M. A., & May, P. J. (2017). Circuits for action and cognition: A view from the superior colliculus. *Annual Review of Vision Science*, *3*, 197–226.

Butler, B. E., Sunstrum, J. K., & Lomber, S. G. (2018). Modified origins of cortical projections to the superior colliculus in the deaf: Dispersion of auditory efferents. *The Journal of Neuroscience: The Official Journal of the Society for Neuroscience*, *38*(16), 4048–4058.

Campagner, D., Vale, R., Tan, Y. L., Iordanidou, P., Pavón Arocas, O., Claudi, F., Stempel, A. V., Keshavarzi, S., Petersen, R. S., Margrie, T. W., & Branco, T. (2023). A cortico-collicular circuit for orienting to shelter during escape. *Nature*, *613*(7942), 111–119.

Carpenter, W. B. (1852). On the influence of suggestion in modifying and directing muscular movement, independently of volition. *Royal Institution of Great Britain*.

Castro-Alamancos, M. A., & Favero, M. (2016). Whisker-related afferents in superior colliculus. *Journal of Neurophysiology*, *115*(5), 2265–2279.

Cooper, B. G., Miya, D. Y., & Mizumori, S. J. (1998). Superior colliculus and active navigation: role of visual and non-visual cues in controlling cellular representations of space. *Hippocampus*, *8*(4), 340–372.

Dräger, U. C., & Hubel, D. H. (1976). Topography of visual and somatosensory projections to mouse superior colliculus. *Journal of Neurophysiology*, *39*(1), 91–101.

Duan, C. A., Pagan, M., Piet, A. T., Kopec, C. D., Akrami, A., Riordan, A. J., Erlich, J. C., & Brody, C. D. (2021). Collicular circuits for flexible sensorimotor routing. *Nature Neuroscience*, *24*(8), 1110–1120.

Duan, C. A., Pan, Y., Ma, G., Zhou, T., Zhang, S., & Xu, N.-L. (2021). A cortico-collicular pathway for motor planning in a memory-dependent perceptual decision task. *Nature Communications*, *12*(1), 2727.

Edwards, S. B., Ginsburgh, C. L., Henkel, C. K., & Stein, B. E. (1979). Sources of subcortical projections to the superior colliculus in the cat. *The Journal of Comparative Neurology*, *184*(2), 309–329.

Ewert, J. P. (1970). Neural mechanisms of prey-catching and avoidance behavior in the toad (Bufo bufo L.). *Brain, Behavior and Evolution*, *3*(1), 36–56.

Ewert, J. P. (1974). The neural basis of visually guided behavior. *Scientific American*, *230*(3), 34–42.

Felsen, G., & Mainen, Z. F. (2008). Neural substrates of sensory-guided locomotor decisions in the rat superior colliculus. *Neuron*, *60*(1), 137–148.

Felsen, G., & Mainen, Z. F. (2012). Midbrain contributions to sensorimotor decision making. *Journal of Neurophysiology*, *108*(1), 135–147.

Finlay, B. L., Schneps, S. E., Wilson, K. G., & Schneider, G. E. (1978). Topography of visual and somatosensory projections to the superior colliculus of the golden hamster. *Brain Research*, *142*(2), 223–235.

Foreman, N., & Stevens, R. (1987). Relationships between the superior colliculus and hippocampus: Neural and behavioral considerations. *The Behavioral and Brain Sciences*, *10*(1), 101–119.

Fries, W. (1985). Inputs from motor and premotor cortex to the superior colliculus of the macaque monkey. *Behavioural Brain Research*, *18*(2), 95–105.

Graybiel, A. M. (1978). Organization of the nigrotectal connection: an experimental tracer study in the cat. *Brain Research*, *143*(2), 339–348.

Harvey, A. R., & Worthington, D. R. (1990). The projection from different visual cortical areas to the rat superior colliculus. *The Journal of Comparative Neurology*, *298*(3), 281–292.

Huerta, M. F., Frankfurter, A. J., & Harting, J. K. (1981). The trigeminocollicular projection in the cat: patch-like endings within the intermediate gray. *Brain Research*, *211*(1), 1–13.

Ingle, D. (1970). Visuomotor functions of the frog optic tectum. *Brain, Behavior and Evolution*, *3*(1), 57–71.

James, W. (1890). *The Principles of Psychology (Vol. 2)*. Henry Holt & Company.

K Harting, J., & Van Lieshout, D. P. (2000). Projections from the rostral pole of the inferior colliculus to the cat superior colliculus. *Brain Research*, *881*(2), 244–247.

Killackey, H. P., & Erzurumlu, R. S. (1981). Trigeminal projections to the superior colliculus of the rat. *The Journal of Comparative Neurology*, *201*(2), 221–242.

Knudsen, E. I., & Konishi, M. (1978). A neural map of auditory space in the owl. *Science (New York, N.Y.)*, *200*(4343), 795–797.

Kustov, A. A., & Robinson, D. L. (1996). Shared neural control of attentional shifts and eye movements. *Nature*, *384*(6604), 74–77.

Lund, J. S., Lund, R. D., Hendrickson, A. E., Bunt, A. H., & Fuchs, A. F. (1975). The origin of efferent pathways from the primary visual cortex, area 17, of the macaque monkey as shown by retrograde transport of horseradish peroxidase. *The Journal of Comparative Neurology*, *164*(3), 287–303.

Lund, R. D. (1964). Terminal distribution in the superior colliculus of fibres originating in the visual cortex. *Nature*, *204*(4965), 1283–1285.

Masullo, L., Mariotti, L., Alexandre, N., Freire-Pritchett, P., Boulanger, J., & Tripodi, M. (2019). Genetically defined functional modules for spatial orienting in the mouse superior colliculus. *Current Biology*, *29*(17), 2892-2904.e8.

May, P. J. (2006). The mammalian superior colliculus: laminar structure and connections. *Progress in Brain Research*, *151*, 321–378.

Meredith, M. A., & Stein, B. E. (1986). Visual, auditory, and somatosensory convergence on cells in superior colliculus results in multisensory integration. *Journal of Neurophysiology*, *56*(3), 640–662.

Munoz, D. P., & Wurtz, R. H. (1995). Saccade-related activity in monkey superior colliculus. I. Characteristics of burst and buildup cells. *Journal of Neurophysiology*, *73*(6), 2313–2333.

Olavarria, J., & Van Sluyters, R. C. (1982). The projection from striate and extrastriate cortical areas to the superior colliculus in the rat. *Brain Research*, *242*(2), 332–336.

Palmer, A. R., & King, A. J. (1982). The representation of auditory space in the mammalian superior colliculus. *Nature*, *299*(5880), 248–249.

Paula-Barbosa, M. M., & Sousa-Pinto, A. (1973). Auditory cortical projections to the superior colliculus in the cat. *Brain Research*, *50*(1), 47–61.

Peysakhovich, B., Zhu, O., Tetrick, S. M., Shirhatti, V., Silva, A. A., Li, S., Ibos, G., Rosen, M. C., Johnston, W. J., & Freedman, D. J. (2024). Primate superior colliculus is causally engaged in abstract higher-order cognition. *Nature Neuroscience*, *27*(10), 1999–2008.

Rizzolatti, G., Riggio, L., Dascola, I., & Umiltá, C. (1987). Reorienting attention across the horizontal and vertical meridians: evidence in favor of a premotor theory of attention. *Neuropsychologia*, *25*(1A), 31–40.

Robinson, D. A. (1972). Eye movements evoked by collicular stimulation in the alert monkey. *Vision Research*, *12*(11), 1795–1808.

Rose, J. D. (1985). Dorsal-ventral differences in the midbrain distribution of single neurons with head movement-correlated and locomotion-correlated firing in the golden hamster. *Experimental Neurology*, *87*(2), 225–234.

Sahibzada, N., Dean, P., & Redgrave, P. (1986). Movements resembling orientation or avoidance elicited by electrical stimulation of the superior colliculus in rats. *The Journal of Neuroscience: The Official Journal of the Society for Neuroscience*, *6*(3), 723–733.

Saitoh, K., Ménard, A., & Grillner, S. (2007). Tectal control of locomotion, steering, and eye movements in lamprey. *Journal of Neurophysiology*, *97*(4), 3093–3108.

Schaefer, K. P. (1970). Unit analysis and electrical stimulation in the optic tectum of rabbits and cats. *Brain, Behavior and Evolution*, *3*(1), 222–240.

Schiller, P. H., & Koerner, F. (1971). Discharge characteristics of single units in superior colliculus of the alert rhesus monkey. *Journal of Neurophysiology*, *34*(5), 920–936.

Schiller, P. H., & Stryker, M. (1972). Single-unit recording and stimulation in superior colliculus of the alert rhesus monkey. *Journal of Neurophysiology*, *35*(6), 915–924.

Schneider, G. (1969). Two visual systems: Brain mechanisms for localization and discrimination are dissociated by tectal and cortical lesions. *Science*, 895.

Senzai, Y., & Scanziani, M. (2024). The brain simulates actions and their consequences during REM sleep. In *bioRxiv*. https://doi.org/10.1101/2024.08.13.607810

Sharp, S. L., Shin, J., Martins, D. M., Jones, K., & Niell, C. M. (2025). Neural dynamics in superior colliculus of freely moving mice. *Cell Reports*, *44*(10), 116284.

Soemmering, S. T. von. (1778). *De basi encephali et originibus nervorum cranio egredientium*. Prostant apud Abr. Vandenhoeck viduam.

Sprague, J. M., & Meikle, T. H., Jr. (1965). The role of the superior colliculus in visually guided behavior. *Experimental Neurology*, *11*(1), 115–146.

Willis, T. (1664). *Cerebri Anatome: cui accessit nervorum descriptio & usus*. Ja. Flesher, for Jo. Martyn, and Ja. Allestry.

Wilson, J. J., Alexandre, N., Trentin, C., & Tripodi, M. (2018). Three-dimensional representation of motor space in the mouse superior colliculus. *Current Biology*, *28*(11), 1744-1755.e12.

Wise, S. P., & Jones, E. G. (1977). Cells of origin and terminal distribution of descending projections of the rat somatic sensory cortex. *The Journal of Comparative Neurology*, *175*(2), 129–157.

Wurtz, R. H., & Goldberg, M. E. (1971). Superior colliculus cell responses related to eye movements in awake monkeys. *Science (New York, N.Y.)*, *171*(3966), 82–84.

Wurtz, R. H., & Goldberg, M. E. (1972). Activity of superior colliculus in behaving monkey. 3. Cells discharging before eye movements. *Journal of Neurophysiology*, *35*(4), 575–586.

Zahler, S. H., Taylor, D. E., Wright, B. S., Wong, J. Y., Shvareva, V. A., Park, Y. A., & Feinberg, E. H. (2023). Hindbrain modules differentially transform activity of single collicular neurons to coordinate movements. *Cell*, *186*(14), 3062-3078.e20.

CHAPTER 2: DIRECTIONAL ALIGNMENT OF TURN-RELATED ACTIVITY WITH LOCOMOTOR DYNAMICS IN THE SUPERIOR COLLICULUS

Abstract

Fluid behavior requires temporal coordination across brain systems that orchestrate movement. A clear example is locomotion, in which left and right turns are not only precisely coordinated with the ongoing stepping rhythm but occur at opposite phases of the step cycle. The circuits underlying this coordination remain poorly understood. We discover that neuronal activity in the mouse superior colliculus, a conserved midbrain structure involved in turning behavior, is tightly phase-locked to the stepping rhythm. Notably, neurons selective for left and right turns fire at opposite phases of the stepping cycle. Moreover, this phase opposition is already evident during straight locomotion, before the animal initiates a turn. By aligning the activity of left and right turn neurons to opposite phases of the stepping cycle, the superior colliculus may create alternating windows of opportunity for left and right turns, facilitating the seamless execution of turns during locomotion.

Introduction

The precise temporal coordination of distinct movements relative to each other is essential for fluid behavior. Even simple behavior like turning left or right during locomotion relies on the precise orchestration of movements. While such turns unfold seamlessly along the animal's trajectory, they are in fact tightly coordinated with the ongoing locomotor stepping rhythm (Patla et al., 1999, 1991). If humans walking along a straight path are cued to turn in a direction of their choosing, for example, the direction will depend on which foot is planted around the time of the cue (Patla et al., 1999, 1991).

Thus, opposite phases of the stepping cycle favor turns in opposite directions. Coordinating turns with specific phases of the stepping cycle ensures that the animal's center of mass is optimally supported throughout the turn while also minimizing the torque to rotate the body (Patla et al., 1999, 1991; Walter, 2003). The stability and efficiency of turns obtained through this coordination are likely fundamental during pursuit and escape behaviors. The identity of the circuits that maintain this coordination is, however, not well understood.

We addressed this question by recording neuronal activity from the superior colliculus (SC), a conserved midbrain structure that plays a central role in turning behavior (Basso & May, 2017; Isa et al., 2021), in freely moving mice. The intermediate and deep motor layers of the SC (dSC) contain 'turn cells' whose activity reports turn direction (Felsen & Mainen, 2008, 2012; Senzai & Scanziani, 2024; Sharp et al., 2025; Wilson et al., 2018) and whose stimulation triggers turning movements (Masullo et al., 2019; Zahler et al., 2023). To determine whether turn-related activity in these neurons is coupled to the stepping rhythm we recorded from the dSC while monitoring locomotor dynamics of mice engaging in left or right turns. We discover that the activity of a large population of turn cells is profoundly modulated by the stepping rhythm and that their turn direction preference, whether left or right, dictates the stepping phase during which they fire the most. Consequently, left and right turn cells fire preferentially at opposite phases of the stepping rhythm, an alternation which is apparent already during straight locomotion. These results reveal how turn related activity in the superior colliculus, one of the best understood motor functions of this structure, unfolds in tight temporal coordination with the ongoing behavior of the organism.

Results

2.1 Coordination of turns with the step cycle

The coordination between turn direction and the step phase is well established in humans (Patla et al., 1999, 1991), but whether this also occurs in mice has not been verified. We therefore assessed the stepping phase of an animal as it performed left or right turns. To determine the stepping phase, we used the angle between the head and the body of the mouse, because in rodents (Kafkafi et al., 1996), like in other walking tetrapods (Goyens & Aerts, 2018; Mulavara et al., 2002), the head swings from right to left throughout each stepping cycle (**Figure 2.1A, Figure 2.2**; see methods for registration of head-body angle to stepping phase). During locomotion, the amplitude of the head-body angle oscillated between positive and negative ~2.5 degrees (2.64 ± 0.06 deg., average ± s.e.m.; here and throughout unless stated otherwise) at ~5.5 Hz (5.45 ± 0.02 Hz, ~11 steps per second). We subdivided this oscillation into the following phases of the stepping cycle (**Figure 2.1B**, right panel): phase 1/2π, when the head, aligned straight with the body, is moving left and the right forepaw is swinging forward, phase 3/2π when the head, aligned straight with the body, is moving right and the left forepaw is swinging forward and phases 0 and π, when the animal's head is pointing to the right or left, respectively, relative to the body. To obtain consecutive trials in which the animals alternated left and right turns, we trained mice on a Y-maze spatial navigation task (**Figure 2.1C**; see methods) in which two of the three reward ports (located at the ends of the maze arms) were active, with their locations changing uncued across blocks. During each trial, the mouse shuttled from one reward port to another, resulting in repeated left and right turns at the maze bifurcation. Crucially, animals reached the center

point of the maze bifurcation at opposite phases of the stepping cycle depending on the direction of the turn (**Figure 2.1D**, left turns near phase 0 (2π), 6.2 ± 0.1 rad., right turns near phase π, 2.9 ± 0.1 rad., n = 55 sessions, $p < 0.001$ for each turn direction, Rayleigh tests, $p < 0.05$, paired Rayleigh test, mean phase difference: 3.0 rad.). Thus, at the maze bifurcation, left and right turns occur at opposite phases of the stepping cycle, consistent with other organisms (Patla et al., 1999, 1991).

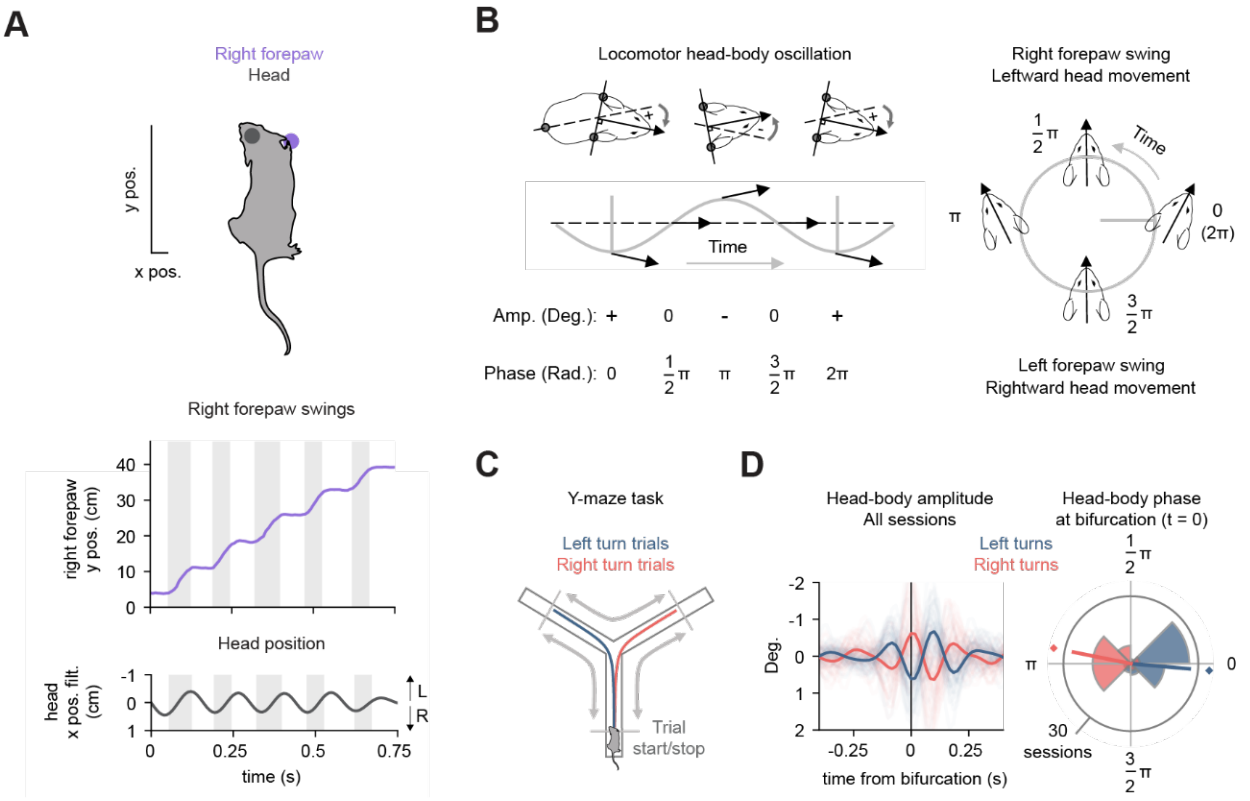

Figure 2.1 Turns are coordinated with the stepping cycle in mice
(A) Left, schematic of mouse with labels on the right forepaw and head (as labeled on frames taken with the bottom view camera; scale bar: 1 cm x, 8 cm y). Right, example pass on linear track. Top: Right forepaw position along the y-axis (y pos.). Gray bands indicate times of right forepaw swings. Bottom: Head position along the x-axis (x pos.) filtered between 4-10 Hz. Note coupling between right forepaw swings and leftward head movements. **(B)** Left, schematic illustration of head-body angle during locomotion. Positive and negative amplitude values reflect right and left head direction relative to the body, respectively. The phase of the head-body oscillation cycle is given in radians. Right, polar plot showing head and forepaw movements associated with each quarter phase of

(Figure caption continued on the next page)

(Figure caption continued from the previous page)

the head-body oscillation cycle. **(C)** Y-maze with average behavioral trajectories of left and right turns across all sessions and mice overlaid (n = 55 sessions, 12 mice). The crossing of the 70% point on the maze arms (gray lines) determines the start and stop of each trial. **(D)** Left, amplitude of head-body angle filtered between 4-8 Hz around the time animals reached the bifurcation across all sessions color coded by turn direction. Time from bifurcation was defined as the time at which the animal's head position crossed the center point of the maze. Dark lines: average over all sessions and animals (n = 55 sessions, 12 mice); light lines: individual sessions. Note similar amplitude yet opposite sign of the head-body angle around the bifurcation. Right, distributions of instantaneous head-body phase at the time the animals reached the bifurcation (t = 0) for each turn direction across sessions. Left turns: $p < 0.001$ Rayleigh test, right turns: $p < 0.001$, Rayleigh test. Paired Rayleigh test between left and right turns: $p < 0.05$).

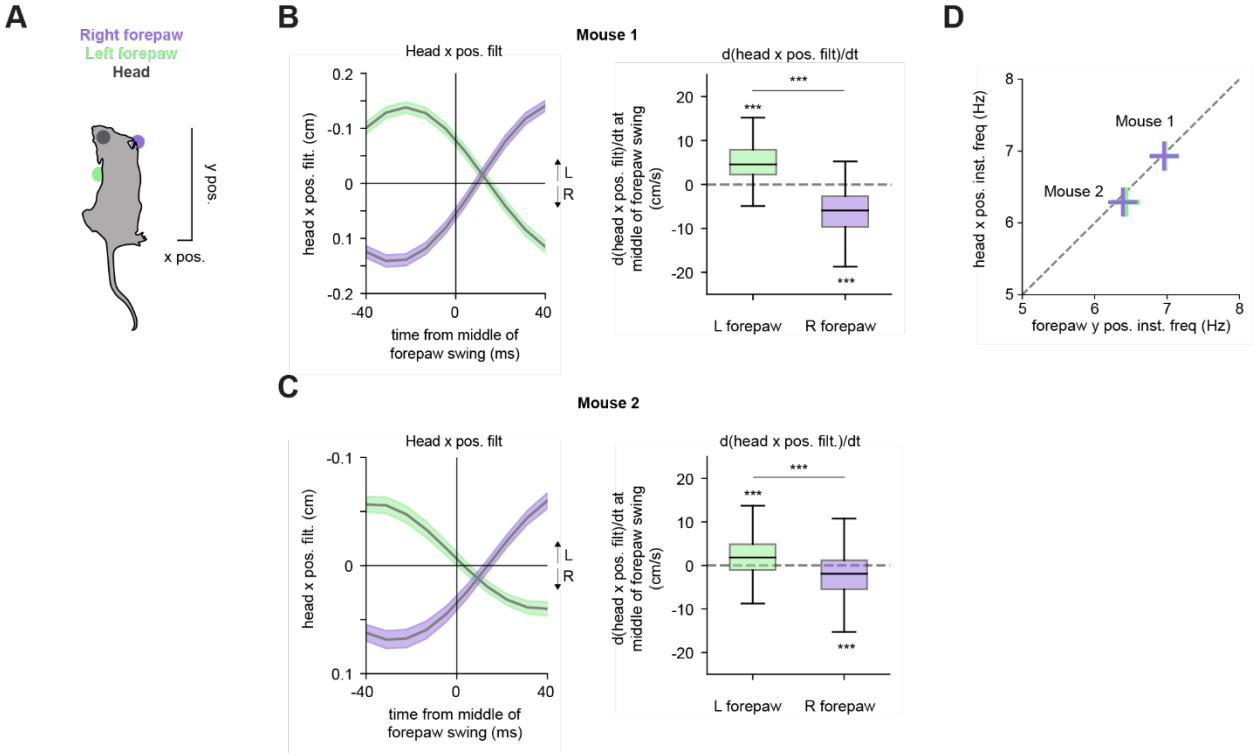

Figure 2.2 Relationship between stepping and left-right head movements in mice
(A) Schematic of mouse with labels on the right forepaw, left forepaw, and head (as labeled on frames from the bottom view camera). **(B)** Left, head position along the x-axis (filtered between 4-10 Hz) for an example mouse (Mouse 1) aligned to the middle of right or left forepaw swings (color code as in (A) thick lines indicate average, shaded bands indicate s.e.m., n = 114 right forepaw swings, 105 left forepaw swings that met criteria (see Methods)). Right, rate of change of head position at the middle of each forepaw

(Figure caption continued on the next page)

(Figure caption continued from the previous page)

swing. Note positive (rightward) rate of change during left forepaw swings and negative (leftward) rate of change during left forepaw swings ($p < 0.001$ for both left and right forepaws, 1-sample t-tests compared to 0, left vs. right: $p < 0.001$, 2-sample t-test). **(C)** Same as in (B) but for another example animal (Mouse 2, n = 293 right forepaw swings, 326 left forepaw swings, $p < 0.001$ for both left and right forepaws, 1-sample t-tests compared to 0, left vs. right: $p < 0.001$, 2-sample t-test). **(D)** Average forepaw oscillation frequency in y position compared to average head oscillation frequency in x position. Both signals were filtered between 4 and 10 Hz.

2.2 Turn cells in the intermediate and deep layers of the SC

Is the activity of turn cells in the dSC modulated in coordination with the stepping cycle and, if so, are left and right turn cells active at opposite phases of the cycle? To address this question, we used silicon probes to record from dSC neurons (**Figure 2.3A, top panel, Figure 2.4**) as mice performed the Y-maze task (**Figure 2.3A, middle panel**). We identified turn cells as neurons whose activity was differentially modulated for left or right turns at the maze bifurcation using the Turn Direction Selectivity Index (TDSI; see Methods), where negative or positive values correspond to left or right turn cells, respectively. Turn cells were defined as cells whose TDSI maintained the same sign and remained significant regardless of which maze arm the animal approached the bifurcation from (**Figures 2.3B** and **2.3C**, 28% of cells, 411/1471 from 12 animals, TDSI for each arm: $p < 0.05$, permutation tests). Turn cell firing peaked around the bifurcation (+18 ± 7 ms, **Figure 2.3D, bottom panel**) and became directionally selective ~300 ms (283 ± 11 ms) before the bifurcation (**Figure 2.3D, top panel**) with a subset (51%, 211/411) achieving selectivity prior to the time at which the animals' behavior diverged between left and right turns (**Figure 2.3A, bottom panel**).

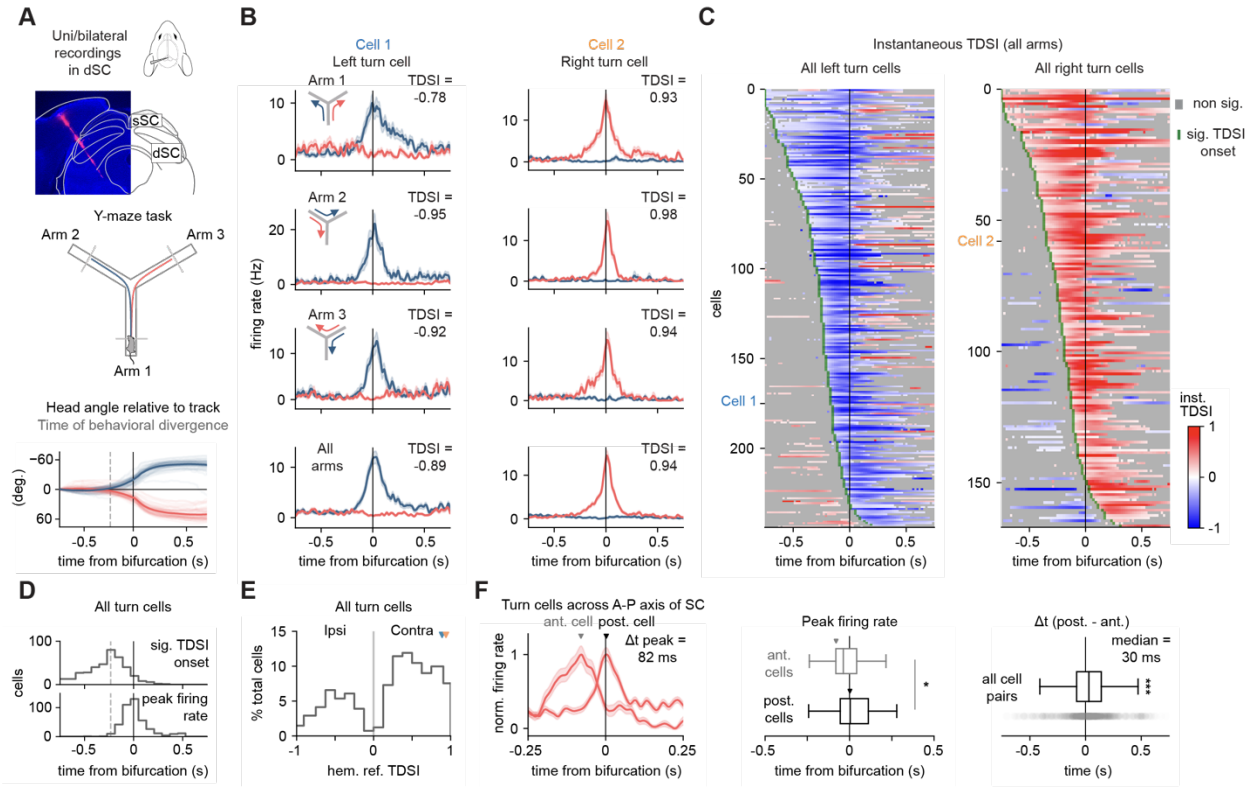

Figure 2.3 Turn cells in the intermediate and deep layers of the SC
(A) Recording configuration and Y-maze task. Top, schematic and histology of an example implantation targeting the intermediate and deep layers of the SC (dSC). Probe track is marked by DiI (pink). sSC superficial layers of the SC. Middle, Y-maze with behavioral trajectories (as in Figure 2.1C). Bottom, angle of the animals' head relative to the track during the task. Dark lines: average over all sessions and animals (n = 55 sessions, 12 mice); light lines: individual sessions. Dashed line: time from the maze bifurcation at which the average head angle relative to the track significantly diverges between right and left turns (-0.25 s). **(B)** Left, example left turn cell (Cell 1). Right, example right turn cell (Cell 2). Thick lines: average firing rates across trials, shaded bands represent s.e.m. Note negative and positive TDSI (Turn Direction Selectivity Index) values for Cell 1 and 2 respectively, across all arms (TDSI: $p < 0.001$ for each arm, permutation tests). **(C)** All left and right turn cells sorted by the time at which the instantaneous TDSI became selective in the cell's preferred turn direction (significant TDSI onset; n = 244 left turn cells, n = 167 right turn cells; 8 right dSC insertions, 34 sessions; 6 left dSC insertions, 28 sessions). **(D)** Distributions of significant TDSI onset times and times of peak firing rate across all turn cells. Dashed lines: average time of behavioral divergence as shown in A. **(E)** Distribution of TDSI values across all turn cells referenced to the recorded dSC hemisphere. Positive and negative hemisphere referenced TDSI values indicate turn cells whose firing is selective for contraversive (e.g. left turn cells in the right dSC) or ipsiversive (e.g. right turn cell in right dSC) turns, respectively. Markers indicate hemisphere referenced TDSI values for Cell 1 and Cell 2.

(Figure caption continued on the next page)

(Figure caption continued from the previous page)

(F) Left, example firing rate curves of two simultaneously recorded right turn cells across the anterior-posterior axis of the left dSC. Note earlier peak firing rate in anterior cell compared to posterior cell. Markers show the time of peak firing rate. Middle, distributions of times of peak firing rate across all anterior and posterior cells ($p < 0.05$, 2-sample t-test). Markers show the peak firing rate for each cell from the left panel. Right, distribution of temporal delays in peak firing rate (posterior – anterior) measured between simultaneously recorded cell pairs (median: 30 ms, IRQ: -8–141 ms, $p < 0.001$, 1-sample t-test compared to 0).

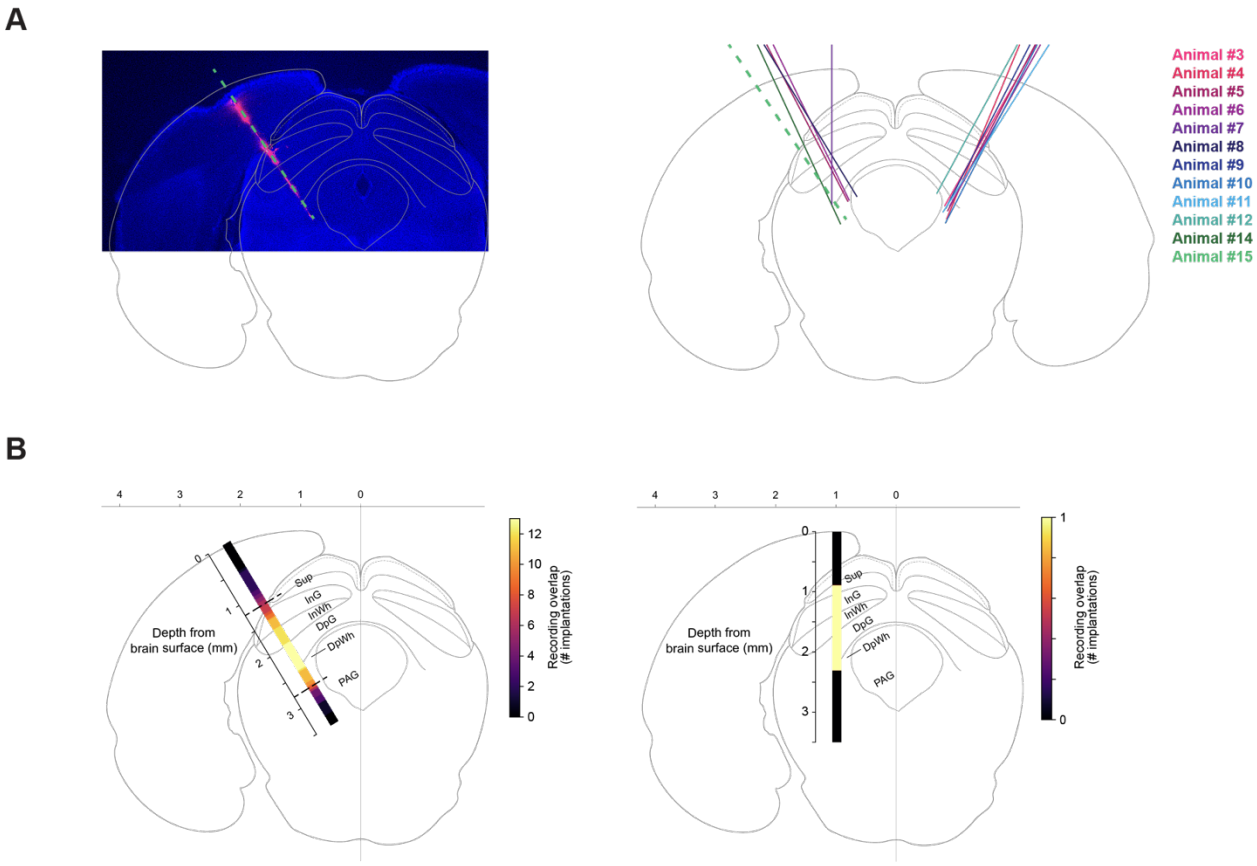

Figure 2.4 Histology and recording site analysis
(A) Left, example coronal section of an implantation targeting the dSC (animal #15). Probe track is marked by DiI (pink) and indicated by a dashed green line. Same as in Figure 2.3A. Right, probe tracks from all implantations (n = 14 implantations from 11 mice (10 unilateral, 2 bilateral)). **(B)** Left, heatmap showing the approximate span of recording depths in the SC across implantations in which the probe was inserted at an angle. Lighter colors indicate higher overlap. Dashed black lines indicate the average depths from the brain surface of the first and last dSC recordings. Note high concentration of recordings between the intermediate gray (InG) and deep white layers (DpWh). Heatmap is oriented

(Figure caption continued on the next page)

(Figure caption continued from the previous page)

at the average implantation angle and average ML/AP coordinates across animals (31°, ML: 2.25 mm, AP: 0 mm from lambda (-4.04 mm from bregma)). Right, heatmap showing the approximate span of recording depths for the vertical implantation. (Sup = superficial layer, InG = intermediate gray layer, InW = intermediate white layer, DpG = deep gray layer, DpWh = deep white layer, PAG = periaqueductal gray, adapted from The Mouse Brain in Stereotaxic Coordinates (Franklin & Paxinos, 2007)).

Consistent with the lateralization of the dSC hemispheres for left and right turns, the majority of turn cells showed selective firing for contraversive turns (**Figure 2.3E**, contraversive (e.g., left turn cells in the right dSC): 69%, 283/411, ipsiversive (e.g., right turn cells in the right dSC): 31%, 128/411). We took advantage of our multiple shank recording configuration, aligned along the anteroposterior axis of the SC, to investigate the spatiotemporal propagation of turn cell activity (Munoz et al., 1991; Munoz & Wurtz, 1995; Port et al., 2000). The activity of cells recorded on anterior shanks peaked significantly earlier than cells on posterior shanks (**Figure 2.3F, left panel**). This was observed both across the population as well as in the temporal delays measured between simultaneously recorded cell pairs (**Figure 2.3F, middle and right panels**, middle panel, $p < 0.05$, 2-sample t-test, right panel, $p < 0.001$, 1-sample t-test; median delay: 30 ms). Thus, during turns, neurons in the dSC show strong turn direction selective firing, and their peak activity propagates posteriorly as the animal proceeds through the turn.

2.3 Turn cell activity is coordinated with the step cycle

We discovered that half of the turn cells (47%, 195/411) exhibited firing that was significantly phase-locked to the stepping cycle (**Figure 2.5A**, example cells). This phase-locked firing was evident throughout the maze, both during straight locomotion as well as during the turn, that is, also outside of periods when turn cells showed direction-selective firing.

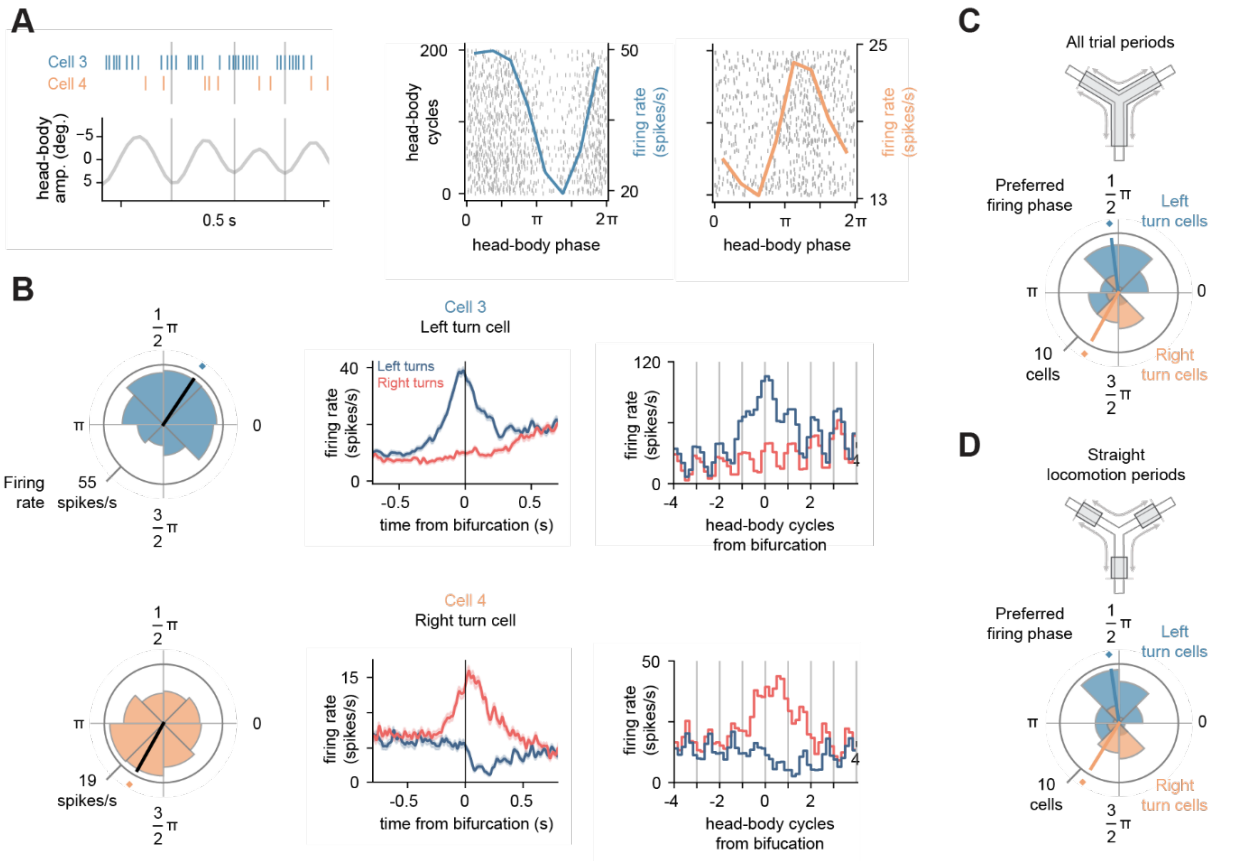

Figure 2.5 Turn cell activity is coupled to the stepping rhythm
(A) Left, spike raster of two simultaneously recorded turn cells, Cell 3 and Cell 4 (top) and ongoing head-body oscillation (bottom). Vertical gray lines indicate phase 0 (2π). Middle and right, spike raster plots of Cell 3 and Cell 4, respectively, aligned to the first 200 head-body oscillation cycles in the session. The overlaid traces are the firing rates averaged over all head-body oscillation cycles in the session (right y-axis). Note that the firing of these two cells is coupled to opposite phases of the head-body oscillation cycle. **(B)** Left, polar plots of the firing of Cell 3 and Cell 4 relative to the phase of the head-body oscillation cycle for the session shown in a. Cell 3: Ln(Z): 7.15, $p < 0.001$, Rayleigh test, preferred firing phase: 0.98 radians; Cell 4: ln(Z): 5.30, $p < 0.001$ Rayleigh test, preferred firing phase: 4.20 radians. Middle, firing rates of Cell 3 and Cell 4 around the time of left and right turns showing their opposite selectivity for turn direction (Cell 3: TDSI = -0.55; Cell 4: TDSI = 0.56). Right, firing rates of Cell 3 and Cell 4 aligned to head-body cycles from turn. Vertical gray lines indicate phase 0 (2π). **(C)** Preferred firing phases of left and right turn cells during all trial periods (left turn cells (TDSI < -0.1), population: $p < 0.01$, right turn cells (TDSI > 0.1), population: $p < 0.05$, Rayleigh tests, left vs. right turn cell populations: $p < 0.05$, permutation test). **(D)** Preferred firing phases of left and right turn cells during straight locomotion periods only (left turn cells, population: $p < 0.01$, right turn cells, population: $p < 0.05$, Rayleigh tests, left vs. right turn cell populations: $p < 0.05$, permutation test). Note that cells maintain the same preferred firing phase during turns and straight locomotion.

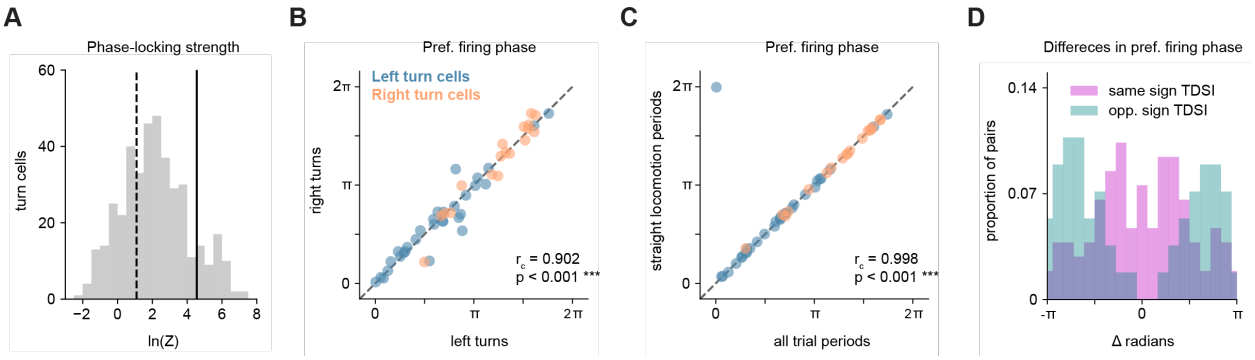

Figure 2.6 Quantification of phase-locking and phase relationships in rhythmically active turn cells
(A) Distribution of log-transformed Rayleigh's Z values across all turn cells (n = 411 cells). Ln(Z) values to the right of the dashed vertical line are significant at $p < 0.05$ (n = 282 cells). Ln(Z) values to the right of the solid vertical line indicate turn cells with the strongest rhythmic activity (n = 49 cells; solid vertical line: mean + SD of ln(Z) values that are significant at the $p < 0.05$ level). **(B)** Correlation between preferred firing phases of left and right turn cells during left vs. right turn trials (rc = 0.902, $p < 0.001$, permutation test). Same populations as in Figure 2.5C. **(C)** Correlation between preferred firing phases of left and right turn cells during all trial periods vs. straight locomotor periods (rc = 0.998, $p < 0.001$, permutation test). Same populations as Figure 2.5C. **(D)** Differences in preferred firing phases between simultaneously recorded cell pairs color coded by whether the pair had TDSI values with the same or opposite sign (same sign pairs (i.e., left turn cell vs. left turn cell), mean angle: 0 ± 0.17 radians; opposite sign pairs (i.e., left turn cell vs. right turn cell), mean angle: -3.06 ± 0.18 radians). Note clustering of same sign pairs around 0 and clustering of opposite sign pairs around ± π (same sign pairs: $p < 0.01$, Rayleigh test; opposite sign pairs: $p < 0.001$, Rayleigh test).

Strikingly, left and right turn cells fired at opposite phases of the stepping cycle (**Figure 2.5B**). By focusing on turn cells with the strongest rhythmic activity (i.e., whose rhythmic activity was most strongly phase-locked to the stepping cycle: ln(Rayleigh Z) > mean + SD of population, 25% of significantly phase-locked cells, 49/195, **Figure 2.6A**, see Methods), we found that left turn cells fired preferentially near phase 1/2π, that is, when the right forepaw is swinging forward and the head is moving left relative to the body (1.7 ± 0.2 rad., n = 31 cells). In contrast, right turn cells fired near the opposite phase, 3/2π, that is, when the left forepaw is swinging forward and the head is moving right relative to the body (4.2 ± 0.3 rad., n = 18 cells; **Figure 2.5C**, $p < 0.05$ for each group,

Rayleigh tests). Preferred firing phases were the same regardless of the direction of the upcoming turn (**Figure 2.6B**, rc = 0.902, $p < 0.001$, permutation test).

Importantly, these cells maintained the same phase preference also during periods of straight locomotion, before and after the animal engaged in the turn (**Figure 2.6C**, rc = 0.998, $p < 0.001$, permutation test). The preferred firing phases of left and right turn cells were significantly different both across the population (**Figure 2.5C**, all trial periods: $p < 0.05$, permutation test, mean phase difference: 2.51 rad.; **Figure 2.5D**, straight locomotion periods: $p < 0.05$, permutation test, mean phase difference: 2.44 rad.) and in the phase differences calculated across simultaneously recorded cell pairs (**Figure 2.6D**). Thus, during locomotion, turn cell activity is rhythmically coupled to the ongoing stepping rhythm, such that left and right turn cells fire at opposite phases of the stepping cycle. Accordingly, the turn direction selectivity of a rhythmically active SC cell is revealed not only around the turn but also during straight locomotion, reflected in its preferred firing phase relative to the stepping cycle.

Discussion

Our study shows that turn-related activity in the dSC, possibly among the best understood motor outputs of this structure, is tightly coupled to ongoing locomotor behavior, such that left and right turn cells preferentially fire at opposite phases of the stepping cycle. To our knowledge this is the first report of oscillatory neuronal activity in the dSC that is coupled to the stepping rhythm. Because of the opposite phases of the stepping cycle at which left and right turn cells fired, their direction preference could be inferred also during straight locomotion. The alignment of turn cell activity to opposite phases of the stepping cycle is likely to alternatively favor left or right turns and may

underlie the seamless coordination observed in vertebrates between turn direction and stepping phase.

The turn cells identified in this study share several characteristics with previously described motor command neurons for orienting movements in the SC: 1) turn cells are located in SC's intermediate and deep layers, layers whose neurons project to brainstem turning centers (Cregg et al., 2020; Usseglio et al., 2020), and whose stimulation elicits turning movements (Masullo et al., 2019; Zahler et al., 2023), 2) turn cell activity primarily encodes contraversive turning movements, consistent with dSC motor signals (Schiller & Stryker, 1972; Senzai & Scanziani, 2024; Sharp et al., 2025; Wurtz & Goldberg, 1971), 3) turn cells become directionally selective before the time at which the animal's behavior diverges between left and right turns, consistent with premotor activity in the dSC (Glimcher & Sparks, 1992; Masullo et al., 2019; Schiller & Stryker, 1972; Senzai & Scanziani, 2024; Sharp et al., 2025; Wurtz & Goldberg, 1971), and 4) turn cells fire similarly at the maze bifurcation regardless of the animal's starting position, indicating that turn cell activity reflects an egocentric, displacement-based motor response. These observations suggest that turn cell activity reported here primarily reflects a motor command for turning.

The basis for the observed rhythmic alternation in the activity of turn cells may lie in the SC's external and internal connectivity. Externally, the dSC receives direct input from motor-associated regions whose activity has been shown to be rhythmically modulated during locomotion (Beloozerova et al., 2023; Drew, 1993; Hirokane et al., 2024). Internally, the dSC contains inhibitory connections both within and between hemispheres (Meredith & Ramoa, 1998; Munoz & Istvan, 1998; Sprague, 1966), which

may support the segregation of turn cell assemblies on opposite phases of the stepping cycle. Locomotor rhythmic activity in the dSC could, however, also originate from sensory inputs (Chinta & Pluta, 2025; Maeda et al., 1979; Meredith & Stein, 1986) that may oscillate in phase with locomotion. Because not all turn cells exhibited activity that was phase-locked to the stepping cycle, the neurons described in this study may constitute a distinct cell type with specific connectivity patterns.

In summary, this study reveals the locking of turn-related activity in the dSC to the stepping rhythm, a temporal modulation that ensures the coordination between motor commands for a specific movement with the ongoing behavior of the organism.

Methods

Experimental model and animals

Neural activity was recorded from twelve male C57BL/6J mice (Jackson Laboratory #000664, 3.5-8 months old). All mice were housed on a reversed cycle (light/dark cycle 12/12h). Mice were housed with littermates before experimentation and singly housed in enriched cages during food-restriction and experimental protocols. All experimental procedures were conducted in accordance with the regulations of the University of California San Francisco Institutional Animal Care and Use Committee (IACUC).

Behavioral training and electrode implantation

The implantation procedure was performed in two phases on two distinct days. First, the implantation of the headplate, and second, the implantation of the silicon probe(s). Mice were implanted under 2% isoflurane anesthesia. The headplate was placed on the skull with dental cement (Unifast LC, GC America; Optibond Universal, Kerr Dental). After post-operative recovery of five days in their home cage, mice were deprived of food to 85% of their baseline weight and pretrained to run on an elevated 1 m linear track for liquid reward (sweetened evaporated soymilk). This training was done to familiarize the mice with running on a track and accessing reward ports. After the mice alternated between the reward ports reliably on the linear track (1-3 days), they were pretrained on the Y-maze task (3-5 days, see *Y-maze task and trial segmentation*). After successful pretraining on the Y-maze, mice underwent the silicon probe implantation surgery. A silicon probe was mounted on a 3D-printed moveable microdrive to record unilaterally or bilaterally from the superior colliculus (SC). In five out of the twelve mice, a

silicon probe was also implanted in the dorsal CA1 region of the hippocampus. Only SC data were analyzed in this study. The types of probes used included: Single-shank probes (Diagnostic Biochips (DBC) P64-4, 64 channels per shank, 20 μm interchannel pitch), four-shank probes (DBC P64-1, 250 μm inter-shank distance, 16 channels per shank, 20 μm interchannel pitch, DBC P128-6, 150 μm inter-shank distance, 32 channels per shank, 25 μm interchannel pitch), and eight-shank probes (DBC P128-8, 150 μm inter-shank distance, 16 channels per shank, 30 μm interchannel pitch). Probe shanks were inserted through a small craniotomy at the coordinates described in the *Electrode insertion, electrode coordinates, histology and recording site assessment* section below. The shanks were initially lowered to 0.7-1.2 mm below the surface of the brain and the microdrive was then fixed, via dental cement, to the headplate. A ground electrode (0.005" diameter stainless wire, A-M systems) was inserted in the cerebellum. After post-operative recovery, mice were placed back on the Y-maze training protocol for 1-5 days while the shanks were lowered to the intermediate and deep SC (dSC). This protocol ensured that peak Y-maze performance coincided with the time at which the recording sites reached the dSC. Mice remained on food restriction for the remainder of the experiment to ensure engagement with the Y-maze task.

Electrophysiological recordings and video tracking

The data presented in this paper are from three to eight 45-140 min sessions per mouse on the Y-maze task. For the stepping analysis, two implanted mice also ran on a transparent linear track (**Figure 2.1, Figure 2.2**, see *Transparent linear track task and stepping analysis*). Electrophysiological data were acquired using an Intan RHD2000 system (Intan Technologies LLC) band-pass filtered between 0.1 Hz and 7.5 kHz and

digitized at 20 kHz. Spike sorting was performed semi-automatically, using Kilosort 2.0 (Pachitariu et al., 2023). This was followed by manual adjustment of the waveform clusters using the software Phy. For the Y-maze task, video data was acquired at 60 frames per second using a CMOS camera (Basler acA1300-200um) placed above the maze. For the transparent linear track task, video was acquired at 124 frames per second using a CMOS camera (Basler acA1300-200um) with a wide-angle lens placed below the track. A machine-learning algorithm, DeepLabCut (Mathis et al., 2018), was trained to track features of the probe housing and distinct body parts of the mice (Y-maze: microdrive probe base (head), left and right ears, base of the tail, transparent linear track: forepaws, under-head/chin area). For position analysis and trial segmentation on the Y-maze, the probe base position (head position) was used as the actual position of the mouse.

Y-maze task and trial segmentation

Mice navigated an elevated Y-maze with equally spaced arms (arm length: 45 cm, arm width: 5 cm) in search of liquid food reward (sweetened evaporated soymilk), which was dispensed from two out of three ports at the ends of each arm. The task consisted of six to eight 50-80 trial blocks, with the locations of the active ports switching in an uncued manner between blocks. The active ports were chosen randomly within each block, with no block containing the same two active ports as the previous block. Animals could not visit the same port on two consecutive trials to receive a reward, so mice learned to alternate between the active ports. For trial segmentation, we first used the track_linearization package (LorenFrankLab, 2024) to map the animal's position on the Y-maze to a simplified one-dimensional representation with a corresponding maze arm

identifier. We then defined a track "position threshold" at 70% of the length of each maze arm (31.5 cm measured outward from the center of the maze or 13.5 cm measured inward from the end of the arm). Trials were defined as periods from when the animal, after leaving a reward port, crossed the position threshold of one arm, made a turn, and crossed the position threshold of another arm without entering any other arms. The time at which an animal reached the bifurcation was defined as the time at which the animal's linearized head position transitioned from one arm to another at the center point of the maze. Animals took ~1.5 seconds to complete each trial (median: 1.57 s, IQR: 1.27-1.98 s, n = 24207 trials across 12 mice).

Head angle relative to the track and time of behavioral divergence

Head angle relative to the track was defined as the angle between the animal's head direction vector (given by the vector perpendicular to the line connecting the ears) and the midline of the track segment from which the animal approached the bifurcation. The time of behavioral divergence was defined as the time at which the animal's head angle relative to the track significantly diverged between left and right turns. To determine the average time of behavioral divergence across sessions and animals (n = 55 sessions, 12 animals, **Figure 2.3A, bottom panel**), we calculated a Behavioral Divergence Index (BDI) as the difference between session-averaged head angles relative to the track for left and right turn trials. BDI was calculated within 200 ms windows advanced in 20 ms steps from 0.85 s before to 0.85 s after the time at which the animal reached the bifurcation. BDI significance was assessed using a permutation test: for each window, a null distribution was generated by randomly permuting left and right turn labels across sessions (10,000 permutations) and recalculating BDI from the resulting averages.

Windows were considered significant only when the observed BDI was more extreme than all shuffled values ($p < 1/10{,}000$). The time of behavioral divergence was defined as the earliest time window belonging to a continuous sequence of such significant windows.

Head-body oscillation and phase estimation

Head-body angle was defined as the angle between the animal's head direction vector (given by the vector perpendicular to the line connecting the ears) and its body vector (given by the line connecting the midpoint between the ears and the base of the tail). To determine the average frequency of the locomotor head-body oscillation, head-body angle traces for each trial were extracted, smoothed with a Savitzky–Golay filter (50 ms, first-order) and bandpass filtered between 3 and 12 Hz (Butterworth, third-order). For all other analyses, head-body angle traces were smoothed and bandpass filtered between 4 and 8 Hz (Butterworth, third-order). Furthermore, trials were included only if they exhibited sufficient power in the head-body angle oscillation signal. To quantify this, for each trial in a given session, power spectral density was estimated using Welch's method and the peak spectral power within the 4-8 Hz range was identified. To ensure that trials had sufficient power for spike-phase estimation, trials whose peak power fell more than one standard deviation below the mean peak power across trials in that session were excluded from analysis.

To estimate the phase of the head-body oscillation at the time of discrete behavioral or neural events (i.e., turns or spikes), we used a Hilbert transform-based interpolation approach. Head-body angle traces were first smoothed and filtered as described above. Peaks and troughs of the filtered signal were then identified (scipy.signal.find_peaks, prominence = 1^{o} amplitude) and the instantaneous phase was

obtained using the Hilbert transform. The oscillatory signal was then segmented into half-cycles (peak-to-trough and trough-to-peak). Event times were assigned a phase by identifying the half-cycle in which the event occurred and linearly interpolating the Hilbert phase within that interval. Events occurring exactly at peaks or troughs were assigned phases of 0 and π, respectively. Full oscillatory cycles, defined by successive peaks, with durations outside the expected range (i.e., cycles faster than 8 Hz or slower than 4 Hz) were excluded from analysis.

Transparent linear track task and stepping analysis

For stepping analysis, implanted mice (n = 2) shuttled back and forth on a transparent linear track (width: 12.7 cm (x), length: 91.4 cm (y)) for liquid food reward (sweetened evaporated soymilk). Video was recorded from below using a wide-angle lens and DeepLabCut was used to track the animals' forepaws and under-head/chin area (head position) for analyzing locomotor dynamics. Due to video distortions at the edges of the track associated with the wide-angle lens, only periods when the mouse was directly above the camera (within a 12.7 cm (x) by 32 cm (y) area) and locomoting uninterrupted were analyzed.

Forepaw swings were defined as periods when either forepaw advanced in the y-direction at speeds greater than 37.65 cm/s (3 pixels/frame). These times were then used as temporal references to examine lateral movements of the head during forepaw swings. Head position in the x-direction was filtered between 4 and 10 Hz (Butterworth, third-order). During locomotion, the head shifted laterally during each forepaw swing, such that a right forepaw swing was linked to a leftward head movement and vice-versa (**Figure 2.3A**). Notably, this same pattern (i.e., contralateral coupling between forepaw swings

and head movements) has been well characterized across a variety of walking tetrapods including lizards, rats, and humans (Goyens & Aerts, 2018; Kafkafi et al., 1996; Mulavara et al., 2002). To quantify the direction of head movement during forepaw swings, we aligned the filtered head position in the x-direction to the middle of each forepaw swing and calculated the instantaneous change in head position (d(head x pos. filt.)/dt, **Figure 2.2B**). In both mice, left forepaw swings were associated with positive (i.e., rightward) changes in head position while right forepaw swings were associated with negative (i.e., leftward) changes in head position (**Figure 2.2B** and **2.2C**). Furthermore, when both the forepaw and head movement signals were filtered between 4 and 10 Hz, their instantaneous frequencies were correlated across mice (**Figure 2.2D**). Thus, the left-right oscillation of the head characteristic of locomotion provides a reliable proxy for the stepping cycle in mice.

Electrode insertion, electrode coordinates, histology and recording site assessment

In six mice, the right SC was targeted; in four mice, the left SC was targeted; and in two mice both the right and the left SC were targeted simultaneously. Lambda was used as the skull reference for all SC craniotomies. In five mice, the SC was targeted by drilling a craniotomy at anteroposterior (AP, from lambda): 0 mm, mediolateral (ML): ± 2.0 mm. The silicon probes(s) were then inserted at a 30^{o} angle from vertical (i.e., a 30^{o} medial tilt along the coronal plane). In six mice, the SC was targeted by a craniotomy at AP: 0 mm, ML: ± 2.5 mm and the silicon probe(s) were inserted at a 32^{o} angle from vertical. In one mouse, the SC was targeted by a craniotomy at AP: 0 mm, ML: -1.0 mm and the silicon probe was inserted vertically with a 10^{o} anterior tilt. All probes were inserted with their shanks running along the anterior-posterior axis of the SC. Prior to

implantation, the backs of all probe shanks were coated with DiI solution (Fisher, V22885) for probe track localization using a fluorescence microscope (**Figure 2.3A, Figure 2.4A**). The shanks were initially lowered to 0.7-1.2 mm below the surface of the brain (dorsoventral, DV) and advanced over consecutive days to reach the dSC. The dSC was targeted using DV coordinates. Once the dSC was reached, probes were advanced between sessions (days) to record from different neurons. For implantations in which the probe was inserted at an angle (n = 13 implantations from 11 mice (9 unilateral, 2 bilateral)), the average depth for the first dSC recording was DV: -1.20 ± 0.11 mm measured from the topmost channel of the probe while the average depth for the last dSC recording was DV: -2.83 ± 0.07 mm measured from the bottommost channel of the probe (**Figure 2.4B, left panel**). For the single vertical implantation, the recordings spanned from DV: -0.88 to -2.30 mm (**Figure 2.4B, right panel**).

For anatomical analysis, mice were perfused transcardially with phosphate-buffered saline (PBS) and then with 4% paraformaldehyde (PFA) in PBS. Brains were extracted, stored in 4% PFA overnight at 4^{o}C and subsequently cut with a vibratome to 100 µm thick coronal sections. Slices were mounted in a Vectashield mounting medium containing DAPI (Vector Laboratories H1500) and fluorescence images were acquired with an Olympus MVX10 MacroView microscope. Probe tracks were identified using the DiI signal.

Turn Direction Selectivity Index (TDSI) and turn cells

Turn selectivity was quantified using a Turn Direction Selectivity Index (TDSI), calculated as the difference between the average firing rates during right and left turns divided by their sum ((Right FR - Left FR) / (Right FR + Left FR)) over a 200 ms window

centered on the time of the cell's peak firing rate. Thus, right turn cells were defined by positive TDSI values and left turn cells were defined by negative TDSI values. To obtain firing rates, spike trains were converted to binary vectors and smoothed using convolution with a Gaussian kernel (50 ms window width). The resulting spike density functions were normalized by the kernel width to express firing rate in spikes per second and averaged across trials. To determine the time window for the TDSI calculation, we first defined a wide window of ± 0.5 s around the time at which the animal reached the bifurcation and, for each neuron, identified within this window the time of peak firing rate for either left or right turns (whichever was greater), using the neuron's average firing rate across all arms. TDSI was then computed across each maze arm within a narrow window of ± 0.1 s (200 ms) centered on this peak firing time.

TDSI significance was assessed using a permutation test. For each neuron and maze arm, left and right turn trials were pooled together and randomly reassigned into two groups whose sizes matched the original sample sizes. TDSI was then recomputed within the narrow window centered on the same actual peak firing time. This procedure was repeated 1000 times to generate a shuffled distribution of TDSI values. For right turn cells, the p-value was defined as the fraction of shuffled TDSI values that were greater than or equal to the observed TDSI, or less than or equal to the observed TDSI for left turn cells. Turn cells were defined as neurons whose TDSI retained the same sign and remained significant ($p < 0.05$) regardless of which maze arm the animal approached the bifurcation from.

Instantaneous TDSI and significant TDSI onset

We computed instantaneous TDSI across the entire trial period (Felsen & Mainen, 2008) to determine the time at which turn cells became directionally selective (significant TDSI onset). TDSI was calculated within 200 ms windows advanced in 20 ms steps from 0.85 s before to 0.85 s after the time at which the animal reached the bifurcation. TDSI significance was assessed with a permutation test: for each window, left and right turn labels were randomly permuted across trials and TDSI was recomputed. This process was repeated 500 times to generate a null distribution for each window. Windows were considered significant when the observed TDSI was more extreme than all shuffled values ($p < 1/500$). Significant TDSI onset was defined as the earliest time point at which a turn cell exhibited two consecutive significant TDSI windows in the expected direction (e.g., for a left turn cell, two consecutive significant TDSI windows with negative TDSI values).

Spatiotemporal spread of turn cell activity

Previous reports in cats and monkeys have shown that motor-related activity in the dSC spreads across the anterior-posterior axis of the SC during eye movements (Munoz et al., 1991; Munoz & Wurtz, 1995; Port et al., 2000). Notably, this activity was found to spread anteriorly during eye movements, where cells related to fixation are located (Munoz et al., 1991). To assess the spatiotemporal spread of activity across the mouse dSC during turns, we analyzed peak firing times of turn cells recorded on four-shank probes that spanned the anterior-posterior axis of the SC. Only recordings that contained two or more turn cells recorded on different shanks were analyzed. Cells were assigned to anterior or posterior groups based on shank position. We then compared the peak firing

times relative to the bifurcation between anterior and posterior groups, as well as the temporal delays in peak firing times measured between simultaneously recorded cell pairs. We found a consistent, posterior spread of dSC activity during turns (**Figure 2.3F**). These results suggest that, as in cats and primates, neural activity spreads across the motor map of the SC in mice during orienting movements. However, in contrast to cats and primates, this activity spreads posteriorly. The difference in the direction of the spread may reflect the difference between ballistic eye movements and controlled locomotor turns.

Phase-locking analysis of turn cell activity to the head-body oscillation cycle

The phase of the head-body oscillation cycle at the time of each spike was estimated using a Hilbert transform-based interpolation approach (see *Head-body oscillation and phase estimation*). A cell's preferred firing phase was defined as the circular mean of all spikes pooled across all trial periods (see *Circular statistics*). Preferred firing phases were also calculated separately for spikes occurring during left or right turns, and straight locomotor periods (**Figure 2.6B** and **2.6C**). To obtain firing rates relative to the head-body oscillation cycle, spike counts were first divided by the total number of cycles and then by the average time per bin based on the average head-body oscillation frequency across animals (5.5 Hz). Phase locking of turn cell activity was assessed via a Rayleigh's test for circular uniformity (see *Circular statistics*).

Head-body cycles from turn

The unwrapped phase of the head-body oscillation signal was obtained for each trial via the Hilbert transform and referenced to the cycle containing the turn. Specifically, the nearest peak of the head-body oscillation signal relative to the turn was used as cycle

zero by subtracting its phase value from the unwrapped signal. Preceding or following peaks were defined as cycles -1, +1, etc. Spike times were then assigned a phase value by linearly interpolating the unwrapped phase at each spike time. Phase-aligned spike counts were then binned (bin width = π/3) and divided by the number of trials. To obtain firing rates, these spike counts per trial were further divided by the average time per bin based on the average head-body oscillation frequency across animals (5.5 Hz). Analyses were done separately for left and right turn trials.

Straight locomotor periods

Straight locomotor periods were defined as periods in which the animal traversed the outer region of the maze, away from the bifurcation. Specifically, we defined a region comprising the outer 50% of the previously defined 70% arm segment length used for trial segmentation (i.e. from 13.5 to 29.75 cm inward from the end of the arm; see *Y-maze task and trial segmentation*). Preferred firing phases during straight locomotion were estimated using only spikes that occurred when the animal was in these regions of the maze, during both inward and outward traversals.

Circular statistics

To quantify the relationship between rhythmic turn cell firing and the head-body oscillation cycle, we employed several circular statistical analyses. Spike times were first converted to phase (see *Head-body oscillation and phase estimation*). The preferred firing phase was calculated as the circular mean of all spike phases, determined by the angle of the mean resultant vector. To determine the strength of phase-locking and its statistical significance, we calculated a Rayleigh's Z statistic for each cell, a standard method for assessing phase-locking between neuronal spiking and local field potential oscillations

(Siapas et al., 2005). Rayleigh's Z statistic uses the formula $Z = nR^2$, where n is the number of spikes and R is the mean resultant length. The associated p-value of the Rayleigh's test was estimated as $p = e^{(-Z)}$; this approximation quantifies the probability that the observed clustering of spikes during the stepping cycle occurred by chance, assuming a null hypothesis of uniform circular distribution. For $n > 50$, $p = e^{(-Z)}$ is adequate (Siapas et al., 2005). To account for multiple comparisons across the population of 411 turn cells, a Bonferroni-corrected significance threshold was applied (a = 0.05/411). A cell was considered significantly phase-locked if its p-value was less than this adjusted alpha level (47% of turn cells, 195/411).

To identify the population of turn cells with the strongest rhythmic activity (**Figure 2.5C**), we employed a two-step filtering process. First, we identified all cells with a Rayleigh Z statistic meeting a nominal significance threshold of $p < 0.05$ (69% of turn cells, 282/411). To normalize the distribution of these values, we calculated the natural log of their Rayleigh Z scores ($\ln(Z)$). We then defined a 'high-strength' subpopulation consisting of cells whose $\ln(Z)$ exceeded the mean + SD of this distribution (mean: 3.11, SD: 1.45, mean + SD: 4.56). This secondary filter ensured that subsequent phase analyses focused on neurons with consistently high phase-locking strength (~25% of significantly phase-locked turn cells, 49/195, **Figure 2.6A**).

To assess whether the preferred firing phases of left and right turn cells within this high-strength population were significantly different (**Figure 2.5C**), we calculated the mean circular difference between the two groups. The observed difference was computed as the angular distance between the circular means of each group, mapped to the range $[0, \pi]$ to represent the shortest distance on the circle. Statistical significance was

assessed using a permutation test (n = 1,000 shuffles). For each shuffle, the turn cell identities (left or right) were randomly shuffled while maintaining the original sample sizes and a null distribution of angular differences was generated. The p-value was defined as the proportion of shuffled iterations where the angular difference was greater than or equal to the observed difference. Differences were considered significant if $p < 0.05$.

To assess differences between paired phase measurements (e.g., stepping phase at the time at which the animal reached the bifurcation for left vs. right turns; **Figure 2.1D**), we computed circular differences between paired observations and applied a Rayleigh test ($p = e^{(-Z)}$, as above) to assess whether these differences were non-uniformly distributed. Paired Rayleigh tests were considered significant if $p < 0.05$, indicating a consistent directional shift between conditions.

Correlations between distributions of preferred firing phases (**Figure 2.6B**, left vs. right turn trials, **Figure 2.6C**, all trial periods vs. straight locomotor periods) were quantified using a circular correlation coefficient (r_c) that is robust to phase wrapping. This metric measures the degree to which deviations from the mean phase in one distribution co-vary with deviations from the mean phase in the other. Correlations were computed using the circcorrcoeff function in astropy.stats in Python. Significance was assessed using a permutation test (n = 10,000 shuffles). For each shuffle, one of the input variables was randomly shuffled and a null distribution of resulting r_c values was generated. The p-value was defined as the proportion of shuffled iterations where the r_c was greater than or equal to the observed r_c.

Quantification and statistical analysis

All analyses and statistical tests were implemented using custom Python scripts (Python version 3.8.5). Statistical tests used and p-values are provided throughout the text and in figure legends.

References

Basso, M. A., & May, P. J. (2017). Circuits for action and cognition: A view from the superior colliculus. *Annual Review of Vision Science*, *3*, 197–226.

Beloozerova, I. N., Nilaweera, W. U., Viana Di Prisco, G., & Marlinski, V. (2023). Signals from posterior parietal area 5 to motor cortex during locomotion. *Cerebral Cortex (New York, N.Y.: 1991)*, *33*(4), 1014–1043.

Chinta, S., & Pluta, S. R. (2025). Whisking and locomotion are jointly represented in superior colliculus neurons. *PLoS Biology*, *23*(4), e3003087.

Cregg, J. M., Leiras, R., Montalant, A., Wanken, P., Wickersham, I. R., & Kiehn, O. (2020). Brainstem neurons that command mammalian locomotor asymmetries. *Nature Neuroscience*, *23*(6), 730–740.

Drew, T. (1993). Motor cortical activity during voluntary gait modifications in the cat. I. Cells related to the forelimbs. *Journal of Neurophysiology*, *70*(1), 179–199.

Felsen, G., & Mainen, Z. F. (2008). Neural substrates of sensory-guided locomotor decisions in the rat superior colliculus. *Neuron*, *60*(1), 137–148.

Felsen, G., & Mainen, Z. F. (2012). Midbrain contributions to sensorimotor decision making. *Journal of Neurophysiology*, *108*(1), 135–147.

Franklin, K. B. J., & Paxinos, G. (2007). *The mouse brain in stereotaxic coordinates* (3rd ed.). Academic Press.

Glimcher, P. W., & Sparks, D. L. (1992). Movement selection in advance of action in the superior colliculus. *Nature*, *355*(6360), 542–545.

Goyens, J., & Aerts, P. (2018). Head stabilisation in fast running lizards. *Zoology (Jena, Germany)*, *127*, 114–120.

Hirokane, K., Nakamura, T., Terashita, T., Kubota, Y., Hu, D., Yagi, T., Graybiel, A. M., & Kitsukawa, T. (2024). Representation of rhythmic chunking in striatum of mice executing complex continuous movement sequences. *Cell Reports*, *43*(6), 114312.

Isa, T., Marquez-Legorreta, E., Grillner, S., & Scott, E. K. (2021). The tectum/superior colliculus as the vertebrate solution for spatial sensory integration and action. *Current Biology*, *31*(11), R741–R762.

Kafkafi, N., Levi-Havusha, S., Golani, I., & Benjamini, Y. (1996). Coordination of side-to-side head movements and walking in amphetamine-treated rats: a stereotyped motor pattern as a stable equilibrium in a dynamical system. *Biological Cybernetics*, *74*(6), 487–495.

LorenFrankLab. (2024). *track_linearization: 2D to 1D position linearization using HMMs*. https://github.com/LorenFrankLab/track_linearization

Maeda, M., Shibazaki, T., & Yoshida, K. (1979). Labyrinthine and visual inputs to the superior colliculus neurons. *Progress in Brain Research*, *50*, 735–743.

Masullo, L., Mariotti, L., Alexandre, N., Freire-Pritchett, P., Boulanger, J., & Tripodi, M. (2019). Genetically defined functional modules for spatial orienting in the mouse superior colliculus. *Current Biology*, *29*(17), 2892-2904.e8.

Mathis, A., Mamidanna, P., Cury, K. M., Abe, T., Murthy, V. N., Mathis, M. W., & Bethge, M. (2018). DeepLabCut: markerless pose estimation of user-defined body parts with deep learning. *Nature Neuroscience*, *21*(9), 1281–1289.

Meredith, M. A., & Ramoa, A. S. (1998). Intrinsic circuitry of the superior colliculus: pharmacophysiological identification of horizontally oriented inhibitory interneurons. *Journal of Neurophysiology*, *79*(3), 1597–1602.

Meredith, M. A., & Stein, B. E. (1986). Visual, auditory, and somatosensory convergence on cells in superior colliculus results in multisensory integration. *Journal of Neurophysiology*, *56*(3), 640–662.

Mulavara, A. P., Verstraete, M. C., & Bloomberg, J. J. (2002). Modulation of head movement control in humans during treadmill walking. *Gait & Posture*, *16*(3), 271–282.

Munoz, D. P., & Istvan, P. J. (1998). Lateral inhibitory interactions in the intermediate layers of the monkey superior colliculus. *Journal of Neurophysiology*, *79*(3), 1193–1209.

Munoz, D. P., Pélisson, D., & Guitton, D. (1991). Movement of neural activity on the superior colliculus motor map during gaze shifts. *Science (New York, N.Y.)*, *251*(4999), 1358–1360.

Munoz, D. P., & Wurtz, R. H. (1995). Saccade-related activity in monkey superior colliculus. II. Spread of activity during saccades. *Journal of Neurophysiology*, *73*(6), 2334–2348.

Pachitariu, M., Sridhar, S., & Stringer, C. (2023). Solving the spike sorting problem with Kilosort. In *bioRxiv*. https://doi.org/10.1101/2023.01.07.523036

Patla, A. E., Adkin, A., & Ballard, T. (1999). Online steering: coordination and control of body center of mass, head and body reorientation. *Experimental Brain Research*, *129*(4), 629–634.

Patla, A. E., Prentice, S. D., Robinson, C., & Neufeld, J. (1991). Visual control of locomotion: strategies for changing direction and for going over obstacles. *Journal of Experimental Psychology. Human Perception and Performance*, *17*(3), 603–634.

Port, N. L., Sommer, M. A., & Wurtz, R. H. (2000). Multielectrode evidence for spreading activity across the superior colliculus movement map. *Journal of Neurophysiology*, *84*(1), 344–357.

Schiller, P. H., & Stryker, M. (1972). Single-unit recording and stimulation in superior colliculus of the alert rhesus monkey. *Journal of Neurophysiology*, *35*(6), 915–924.

Senzai, Y., & Scanziani, M. (2024). The brain simulates actions and their consequences during REM sleep. In *bioRxiv*. https://doi.org/10.1101/2024.08.13.607810

Sharp, S. L., Shin, J., Martins, D. M., Jones, K., & Niell, C. M. (2025). Neural dynamics in superior colliculus of freely moving mice. *Cell Reports*, *44*(10), 116284.

Siapas, A. G., Lubenov, E. V., & Wilson, M. A. (2005). Prefrontal phase locking to hippocampal theta oscillations. *Neuron*, *46*(1), 141–151.

Sprague, J. M. (1966). Interaction of cortex and superior colliculus in mediation of visually guided behavior in the cat. *Science (New York, N.Y.)*, *153*(3743), 1544–1547.

Usseglio, G., Gatier, E., Heuzé, A., Hérent, C., & Bouvier, J. (2020). Control of orienting movements and locomotion by projection-defined subsets of brainstem V2a neurons. *Current Biology*, *30*(23), 4665-4681.e6.

Walter, R. M. (2003). Kinematics of 90 degrees running turns in wild mice. *The Journal of Experimental Biology*, *206*(Pt 10), 1739–1749.

Wilson, J. J., Alexandre, N., Trentin, C., & Tripodi, M. (2018). Three-dimensional representation of motor space in the mouse superior colliculus. *Current Biology*, *28*(11), 1744-1755.e12.

Wurtz, R. H., & Goldberg, M. E. (1971). Superior colliculus cell responses related to eye movements in awake monkeys. *Science (New York, N.Y.)*, *171*(3966), 82–84.

Zahler, S. H., Taylor, D. E., Wright, B. S., Wong, J. Y., Shvareva, V. A., Park, Y. A., & Feinberg, E. H. (2023). Hindbrain modules differentially transform activity of single collicular neurons to coordinate movements. *Cell*, *186*(14), 3062-3078.e20.

CHAPTER 3: HIPPOCAMPAL REPRESENTATIONS OF POSSIBLE FUTURES PREDICT MOTOR OUTPUT IN THE SUPERIOR COLLICULUS

Abstract

The ability to represent possible futures allows animals to evaluate different options and act accordingly. The hippocampus can express representations of possible future paths, but the brain structures involved in transforming these representations into actions remain unknown. Here we show that hippocampal representations of possible future paths predict motor-related activity in the superior colliculus (SC), a midbrain structure involved in turning. By recording simultaneously from hippocampal neurons and from left- or right-preferring 'turn cells' in the motor layers of the SC in navigating mice, we found that hippocampal representations of left or right possible future paths predicted increased firing rates of SC turn cells with matching left or right turn preference. This relationship was also evident in the animals' behavior: when the hippocampus represented future paths that were not ultimately taken, movement trajectories were nonetheless biased toward those paths, demonstrating that animals partially enacted possible futures that were represented but not selected. These results reveal a coordination between a cognitive and a motor structure and provide a potential pathway for mental simulations of possible futures to influence actions.

Introduction

Animals navigating their environments can mentally represent possible future paths (Comrie et al., 2022; Johnson & Redish, 2007; Kay et al., 2020). While the expression of these representations allows animals to evaluate multiple options and act accordingly (Comrie et al., 2022; O'Keefe, 2025; Redish, 2016; Wikenheiser & Redish,

2015), the neural circuits involved in transforming these representations into actions remain unknown.

The hippocampus is capable of representing hypothetical scenarios, including possible future options (Comrie et al., 2022; Johnson & Redish, 2007; Kay et al., 2020). During locomotion, individual cycles of the ~8 Hz theta rhythm can include spatial representations that sweep ahead of the animal's current location toward possible future locations, including possible future paths (Johnson & Redish, 2007; Kay et al., 2020; Vollan et al., 2025). Whether the expression of these representations leaves a specific and measurable impression on activity in regions that drive action is not known.

To address this, we recorded simultaneously from the hippocampus and the superior colliculus (SC), a conserved midbrain structure involved in turning behavior (Basso & May, 2017; Isa et al., 2021), as mice navigated a Y-maze. We recorded from the intermediate and deep layers of the SC (dSC), layers that contain motor command neurons for left or right turns (Felsen & Mainen, 2008, 2012; Senzai & Scanziani, 2024; Sharp et al., 2025; Wilson et al., 2018). Furthermore, the dSC is known to integrate diverse inputs related to turning (Campagner et al., 2023; Dean et al., 1989; Evans et al., 2018), raising the possibility that hippocampal representations of possible futures are transmitted to the dSC to influence turning actions. Such a mechanism would imply a consistent, predictive relationship between hippocampal representations of left or right future paths and the activity of dSC neurons associated with left or right turns.

To investigate this relationship, we took advantage of the fact that, as animals approach a bifurcation on a maze, the hippocampus can generate representations that sweep either toward the path the animal ultimately takes or toward the alternative path.

Thus, for a given path taken by the animal, we can determine whether the activity of dSC neurons varies depending on the direction of hippocampal sweeps. We show that hippocampal representations of future paths predict increased firing rates of dSC neurons with matching turn preference. Moreover, we show that this relationship manifests in behavior: hippocampal representations of future paths are associated with deviations in the animal's trajectory toward the represented path. These results reveal a coordination between cognitive representations of possible future paths and motor commands that steer the animal toward those paths, suggesting a pathway for mental simulations of possible futures to influence actions.

Results

3.1 Simultaneous monitoring of CA1 and SC turn cell activity

We used silicon probes to record from both hippocampal CA1 and dSC neurons as mice performed a Y-maze spatial navigation task (**Figure 3.1A, Figure 3.2**). Each task session consisted of multiple trial blocks of 50-80 trials during which two of the three reward ports (located at the ends of the maze arms) were active, with their locations changing uncued across blocks. This trial block design was chosen to maintain cognitive engagement with the task. During each trial, the mouse navigated from one reward port to the other and, across trials, consistently shuttled between the two active ports, resulting in turns at the maze bifurcation.

We first characterized the CA1 representation of position as animals traversed the Y-maze. We used a state-space decoding algorithm (Denovellis et al., 2021) to estimate the locations represented in the firing patterns of hippocampal neurons (1 ms bins, n = 2642 hippocampal CA1 neurons across 5 animals). We confirmed accurate decoding of

position (absolute error = 3.8 ± 0.2 cm, average ± s.e.m.; here and throughout unless stated otherwise). Furthermore, as animals approached the bifurcation, we observed non-local spatial representations that swept left or right ahead of the animal, reflecting possible future paths along the left of right arm of the maze (**Figure 3.1B, middle panels**).

Next, we focused on 'turn cells' in the dSC, a population of neurons that exhibited turn-direction selective firing around the maze bifurcation. We defined turn cells as neurons that showed significant firing rate modulation around turns (significant Turn Direction Selectivity Index or TDSI, see Methods), consistently in the same direction, regardless of which maze arm the animal came from. As observed in our previous study (**Chapter 2**), turn cells accounted for ~30% of dSC cells (167/552 from 5 animals, **Figure 3.3A**). Turn cell firing peaked around the bifurcation (+34 ± 172 ms, average ± s.d., **Figure 3.3C, bottom panel**) and became directionally selective ~250 ms before the bifurcation (-248 ± 216 ms, average ± s.d., **Figure 3.3C, top panel**). A subset of turn cells (25%, 41/167) became directionally selective prior to the time at which the animals' behavior diverged between left and right turns (**Figure 3.3B**) in line with premotor activity previously reported in the dSC (Glimcher & Sparks, 1992; Masullo et al., 2019; Schiller & Stryker, 1972; Senzai & Scanziani, 2024; Sharp et al., 2025; Wurtz & Goldberg, 1971). Furthermore, consistent with the lateralization of the dSC hemispheres for left and right turns (Schiller & Stryker, 1972; Senzai & Scanziani, 2024; Sharp et al., 2025; Wurtz & Goldberg, 1971), about two thirds of turn cells showed selective firing for contraversive turns relative to the recorded SC hemisphere (**Figure 3.3D**, contraversive: 72%, 120/167, ipsiversive: 28%, 47/167). Together, these observations are consistent with these cells functioning as motor command neurons for turning.

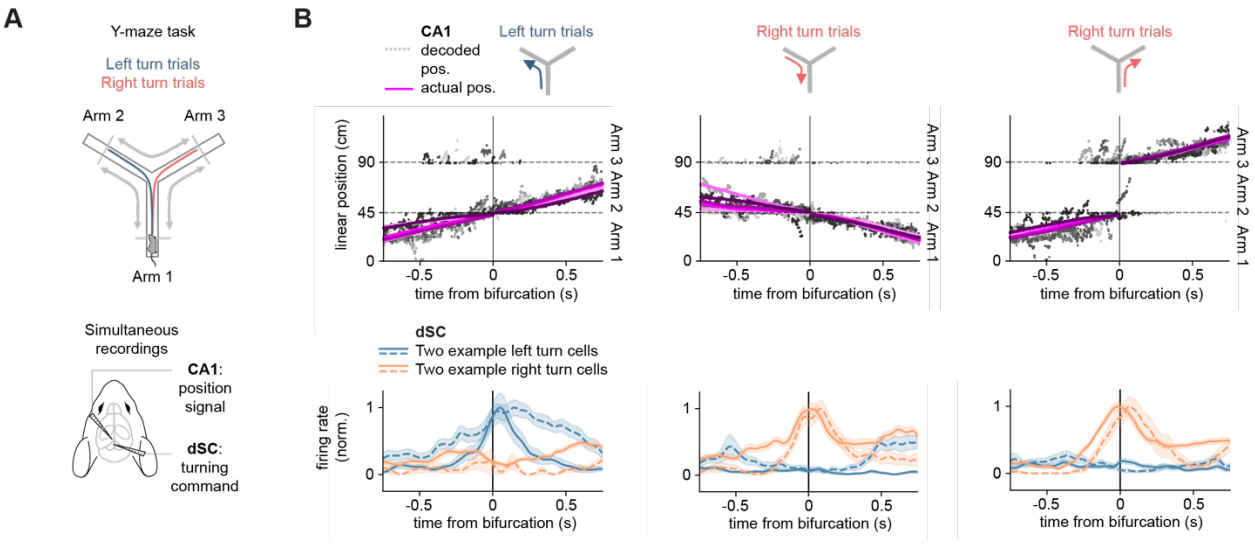

Figure 3.1 Simultaneous monitoring of hippocampal spatial representations and SC turn cell activity during a Y-maze task

(A) Top, Y-maze with average behavioral trajectories of left and right turns across all sessions and mice overlaid (n = 20 sessions, 5 mice). The crossing of the 70% point on the maze arms (gray lines) determines the start and stop of each trial. Bottom, recording configuration targeting both the dorsal CA1 region of the hippocampus and the intermediate and deep layers of the SC (dSC). **(B)** Top, example sets of maze traversals (5 trials each) as the animal approached the bifurcation from three different maze arms (left panel: left turn trials from arm 1 to arm 2, middle panel: right turn trials from arm 2 to arm 1, right panel: right turn trials from arm 1 to arm 3). Gray scatter points: decoded position from CA1 taken as the peak of the probability distribution at each time point (y-axis, linearized position). Pink lines: the animal's actual position. Line shading is matched across decoded and actual positions within each trial (i.e., lightest gray trial corresponds to lightest pink trial). Note that, prior to the bifurcation, the decoded position periodically sweeps ahead, representing both the path ultimately taken by the animal and, on some trials, the alternative path. Bottom, two example left turn cells and two example right turn cells recorded simultaneously from the dSC. Thick and dashed lines indicate the average firing rates of two individual cells of the same turn preference (blue: left turn cells, orange: right turn cells) while shaded bands represent s.e.m. (left panel: all left turn trials from arm 1 to arm 2, middle panel: all right turn trials from arm 2 to arm 1, right panel: all right turn trials from arm 1 to arm 3). Note how each turn cell fires similarly at the maze bifurcation regardless of which maze arm the animal approaches the bifurcation from.

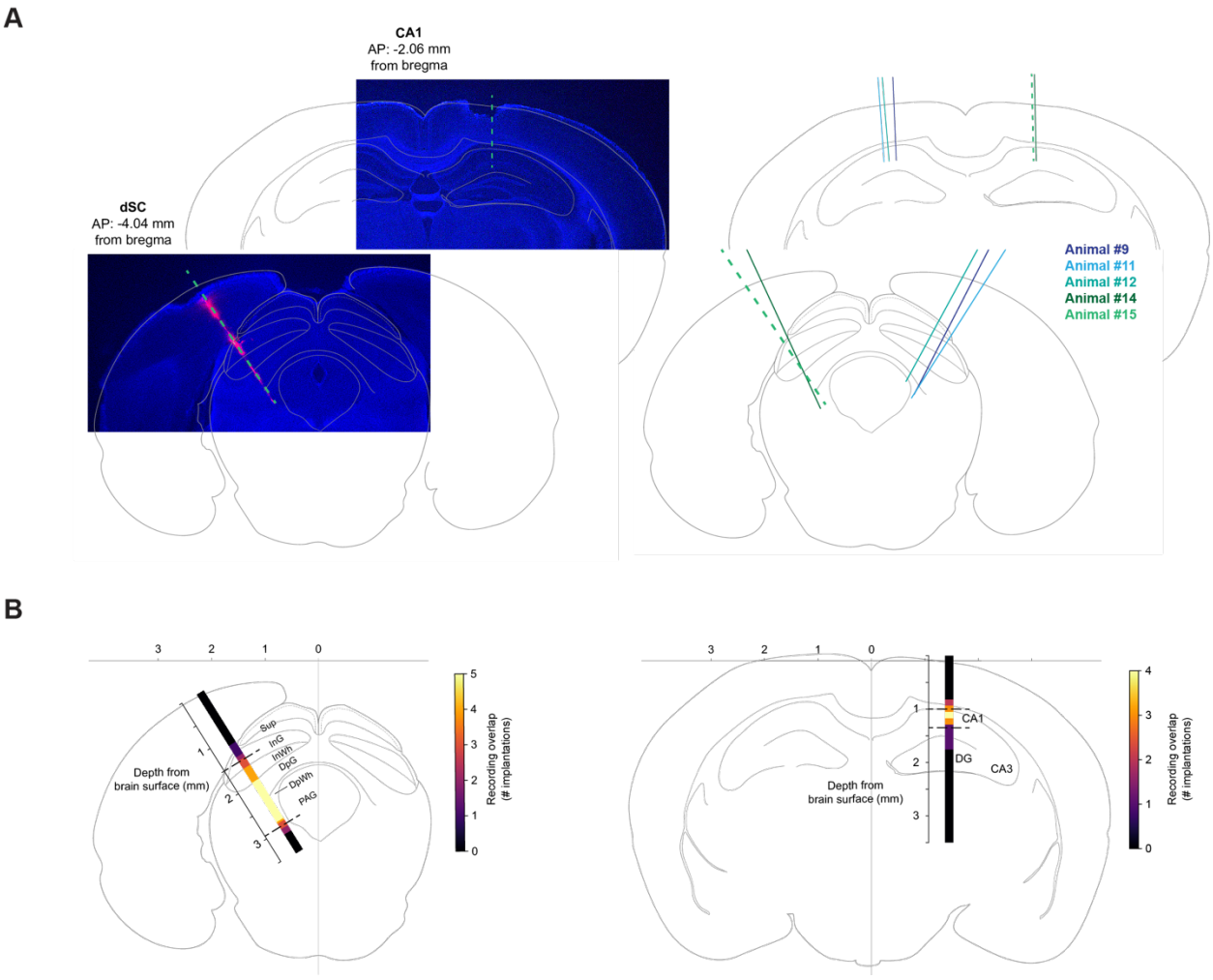

Figure 3.2 Histology and recording site analysis
(A) Left, example coronal sections of probe implantations targeting the dSC and dorsal CA1 regions in an example animal (animal #15). Probe track in dSC is marked by DiI (pink) and indicated by a dashed green line. Probe track in CA1 is indicated by dashed green line. Right, probe tracks in dSC and dorsal CA1 across all implantations (n = 5 implantations from 5 mice). **(B)** Left, heatmap showing the approximate span of recording depths in the SC across implantations. Lighter colors indicate higher overlap. Dashed black lines indicate the average depths from the brain surface of the first and last dSC recordings. Note high concentration of recordings between the intermediate gray (InG) and deep white layers (DpWh). Heatmap is oriented at the average implantation angle and ML/AP coordinates across animals. (Sup = superficial layer, InG = intermediate gray layer, InW = intermediate white layer, DpG = deep gray layer, DpWh = deep white layer, PAG = periaqueductal gray). Right, same as left panel but for CA1 implantations. All outlines of histological sections were adapted from The Mouse Brain in Stereotaxic Coordinates (Franklin & Paxinos, 2007).

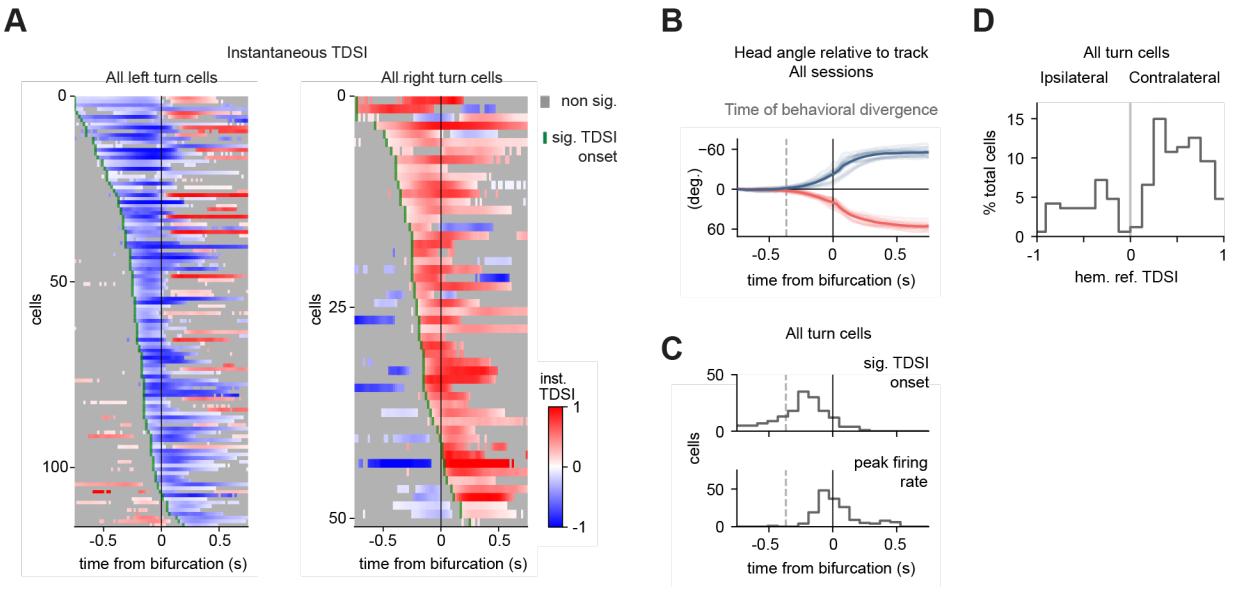

Figure 3.3 Characterization of SC turn cells from hippocampal recording sessions **(A)** All left and right turn cells sorted by the time at which the instantaneous TDSI became selective in the cell's preferred turn direction (significant TDSI onset; n = 116 left turn cells, n = 51 right turn cells; 3 right dSC insertions, 12 sessions; 2 left dSC insertions, 7 sessions). **(B)** Angle of the animals' head relative to the track during the task. Dark lines: average over all sessions and animals (n = 19 sessions, 5 mice); light lines: individual sessions. Dashed line: time from the maze bifurcation at which the average head angle relative to the track significantly diverges between right and left turns (-0.37 s). **(C)** Distributions of significant TDSI onset times and times of peak firing rate across all turn cells. Dashed lines: average time of behavioral divergence as shown in (B). **(D)** Distribution of TDSI values across all turn cells referenced to the recorded dSC hemisphere. Positive and negative hemisphere referenced TDSI values indicate turn cells whose firing is selective for contraversive (e.g. left turn cells in the right dSC) or ipsiversive (e.g. right turn cell in right dSC) turns, respectively.

3.2 Turn cell activity is modulated in coordination with hippocampal representations of future paths

Is turn cell activity modulated according to hippocampal representations of future paths? To address this question, we identified periods during which, as the animal approached the bifurcation, the hippocampal representation of position swept ahead, representing future paths along the left or right arm (**Figure 3.5A** and **3.5B**, see Methods).

As expected (Comrie et al., 2024; Andrew E. Papale et al., 2016), most hippocampal sweeps were directed toward the path the animal would ultimately take ('ipsi sweeps', 73.7 ± 1.8%) and the rest toward the alternative path ('contra sweeps'). Contra sweeps occurred earlier relative to the turn and swept farther ahead of the animal compared to ipsi sweeps (**Figure 3.4A** and **3.4B**). Moreover, while the onsets of both ipsi and contra sweeps occurred preferentially during late phases of the ~8.5 Hz (8.49 ± 0.07 Hz) hippocampal theta rhythm, contra sweeps exhibited weaker phase locking compared to ipsi sweeps (**Figure 3.4C**). Lastly, consistent with recent results in rats (Comrie et al., 2024), the expression of contra sweeps was transiently increased following block switches compared to ipsi sweeps (**Figure 3.4D**).

To determine whether, for a given turn direction taken by the animal, dSC turn cell activity varied depending on the direction of hippocampal sweeps, we focused on trials with only left or right sweeps, excluding trials with sweeps in both directions and trials without sweeps. We computed the Sweep Direction Selectivity Index (SDSI, see Methods) that quantified, for turns in a given direction, the difference in firing rates seen on trials with sweeps in the same versus the opposite direction.

Strikingly, the activity of a third of turn cells was significantly modulated around the time of the bifurcation depending on the direction of hippocampal sweeps (34%, 56/167, $p < 0.05$, permutation test, **Figure 3.5C**, cell 1, SDSI: $p < 0.01$, **Figure 3.5D**, cell 2, SDSI: $p < 0.05$, permutation tests, **Figure 3.6**, additional examples). Moreover, there was a strong positive correlation between TDSI and SDSI (**Figure 3.5E**, TDSI vs. SDSI, $n = 56$ cells, Pearson $r = 0.61$, $p < 0.001$). Indeed, most of these cells fired more on average during trials with sweeps in their preferred turn direction compared to trials with sweeps

in their non-preferred turn direction (‘sweep-selective turn cells’, 75%, 42/56). Of these, most cells (62%, 26/42) exhibited sweep direction selective firing during trials in which the animal turned in the cell’s preferred direction.

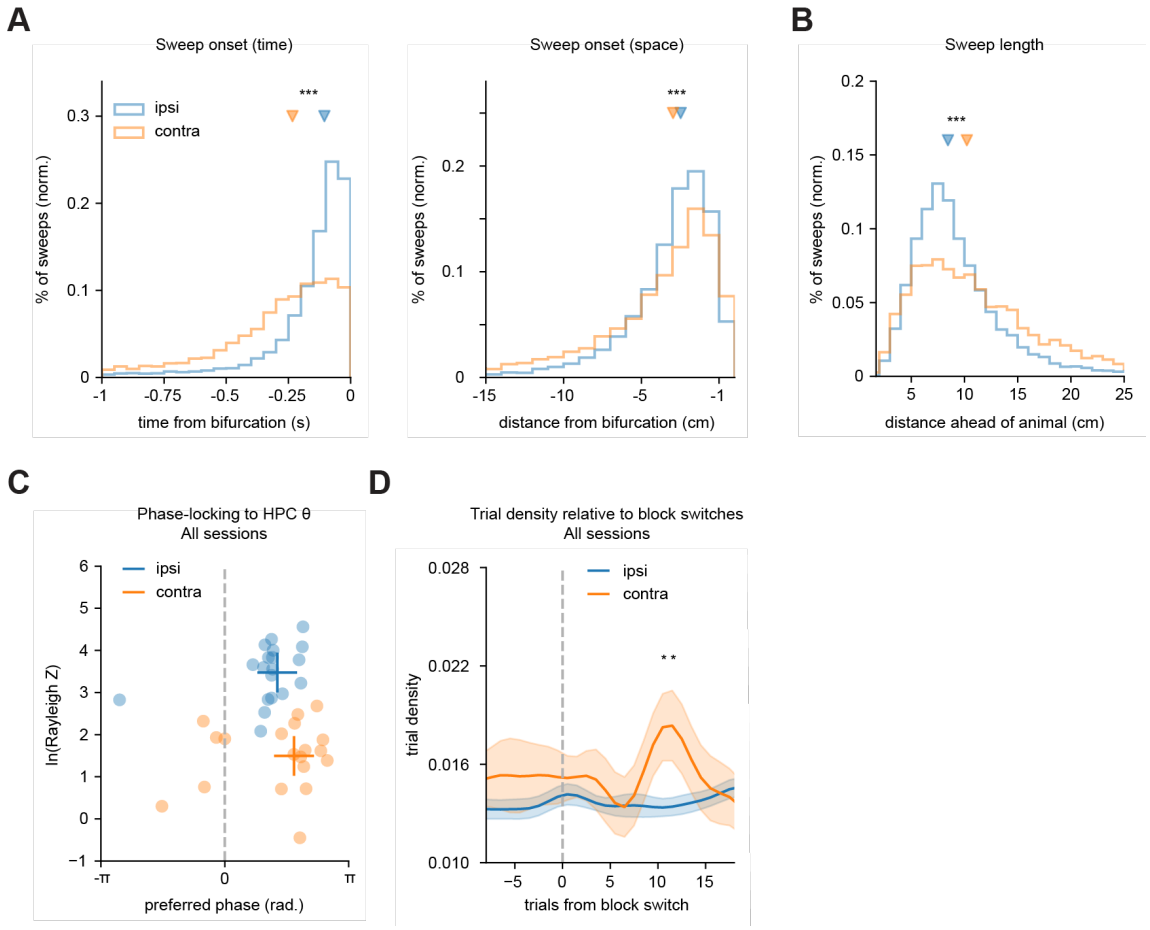

Figure 3.4 Ipsi and contra sweep parameters
(A) Left, distributions of sweep onset times relative to the turn for ipsi and contra sweeps (ipsi sweeps, blue, n = 9178 sweeps, median: -105 ms, IQR: -54 to -201 ms, contra sweeps, orange, n = 3002 sweeps, median: -234 ms, IQR: -115 to -403 ms, $p < 0.001$, Mann-Whitney U test). Right, distributions of the animals’ distance from the turn at the onset of ipsi and contra sweeps (ipsi sweeps, median: -3.47 cm, IQR: -2.21 to -5.40 cm, contra sweeps, median: -3.96 cm, IQR: -2.20 to -7.31 cm, $p < 0.001$, Mann-Whitney U test). **(B)** Distributions of sweep distance from the animal’s position for ipsi and contra sweeps (ipsi sweeps, median: 8.45 cm, IQR: 6.47-11.29 cm, contra sweeps, median: 10.23 cm, IQR: 6.76-14.93 cm, $p < 0.001$, Mann-Whitney U test, $p < 0.001$, Mann-Whitney U test). Sweep distance was calculated as the average difference between the animal’s actual and decoded positions during the duration of the sweep. **(C)** Phase-locking of

(Figure caption continued on the next page)

(Figure caption continued from the previous page)

sweeps to late phases (0 to π rad.) of the hippocampal theta cycle across sessions (n = 19 sessions, ipsi, pref. phase: +1.33 ± 0.13 rad., contra, pref. phase: +1.76 ± 0.26 rad., ipsi vs. contra: $p > 0.05$, permutation test). X-axis indicates hippocampal theta phase where phase 0 corresponds to the trough of the theta cycle recorded at the CA1 pyramidal cell layer. Y-axis indicates strength of phase-locking. Note that, while both types of sweeps were phase-locked to late phases of theta, contra sweeps were more weakly phase-locked compared to ipsi sweeps (ipsi, ln(Rayleigh Z): 3.48 ± 0.15, contra, ln(Rayleigh Z): 1.49 ± 0.18, ipsi vs. contra: $p < 0.001$, paired t-test). Markers indicate average values. **(D)** Density of trials containing only ipsi or contra sweeps aligned to block switches across sessions (n = 19 sessions). Traces were normalized by the number of trials of each type (ipsi or contra) per session and smoothed with a Gaussian kernel (2 bins). Thick lines represent the mean and shaded bands represent s.e.m. Note the transient increase in the density of contra sweep trials following block switches relative to ipsi sweep trials ($p < 0.05$ per bin, permutation tests), consistent with recent findings in rats showing an increased proportion of representations of alternative possibilities during periods of increased cognitive demand (Comrie et al., 2024).

To determine whether the activity of dSC neurons can be bidirectionally modulated, that is increase or decrease their firing in coordination with sweep direction, we analyzed the firing rates of each sweep-selective turn cell around the time of the bifurcation across three distinct trial types: trials with sweeps 1) only in the cell's preferred direction, 2) only in the cell's non-preferred direction, and 3) in both directions, all relative to trials without sweeps. This analysis revealed a clear bidirectional modulation of dSC firing rates relative to the no-sweep condition: sweep-selective turn cells fired more during trials with sweeps only in their preferred direction, less during trials with sweeps only in their non-preferred direction, and showed no significant change during trials with sweeps in both directions (**Figure 3.5F**, preferred/non-preferred only: $p < 0.001$, both: $p > 0.05$, 1-sample t-tests). Together, these results reveal that the activity of dSC turn cells is modulated in coordination with hippocampal representations of future paths.

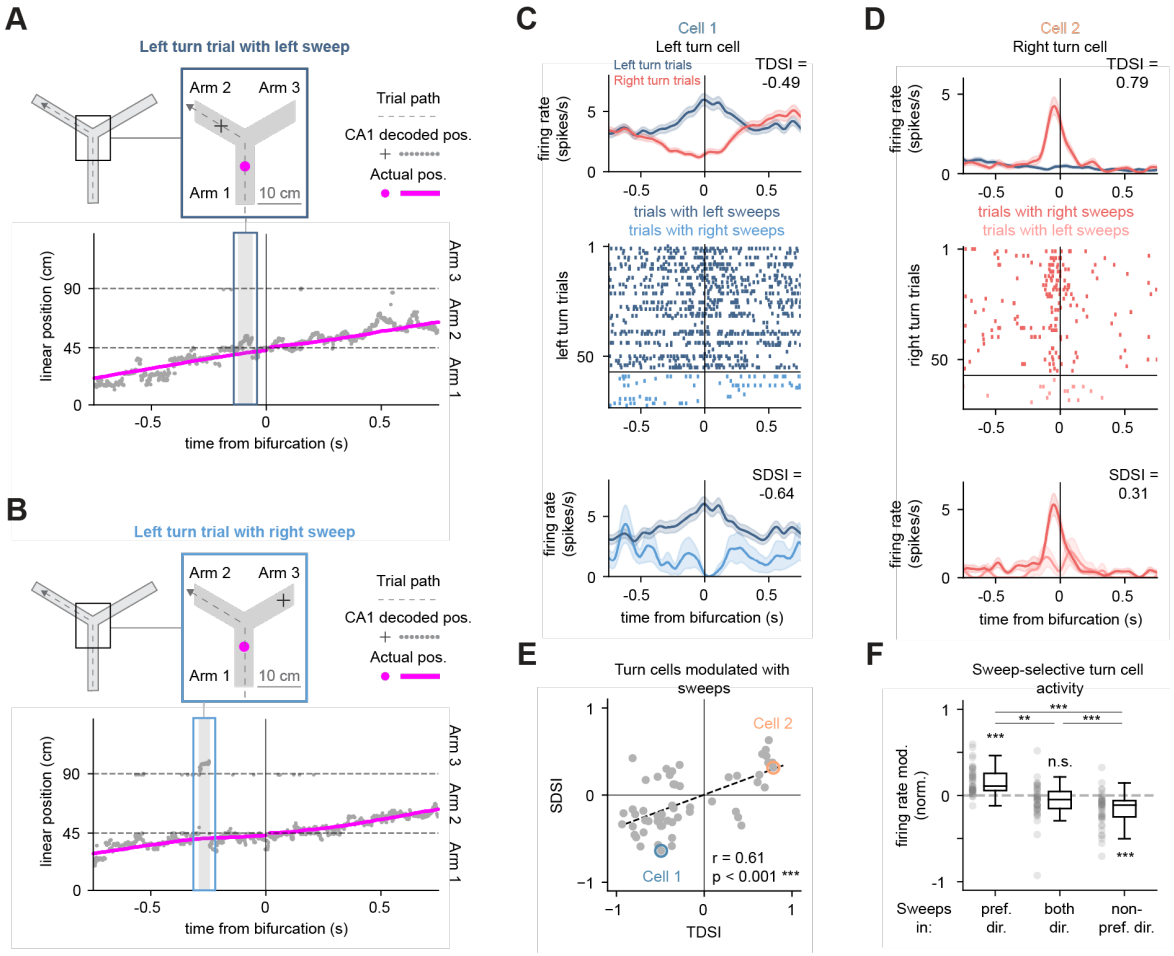

Figure 3.5 Turn cell activity is modulated in coordination with hippocampal sweeps **(A)** Example left turn trial with left hippocampal sweep. Top (expanded view), maze schematic showing a snapshot of the animal's actual position (pink circle) and decoded position (black crosshair) during the sweep. The position of each marker reflects the average linearized position, either actual or decoded, across the time window indicated by the outlined gray band in the bottom plot. Bottom, plot showing the decoded position (gray) and actual position (pink) relative to the maze bifurcation (y-axis, linearized position). Note the decoded position sweeping up into the left arm as the animal approaches the bifurcation. **(B)** Same as in A, but for a left turn trial with a right hippocampal sweep during the same session. **(C)** Top, firing rate profiles of a left turn cell in the dSC (Cell 1). Data taken from the same session as in A and B. Middle, spike raster plot for Cell 1 during left turn trials. Dark blue spikes indicate spikes during left turn trials with left sweeps; light blue spikes indicate spikes during left turn trials with right sweeps. Bottom, firing rate profiles of Cell 1 during left turn trials separated by sweep direction (same color scheme as in middle panel). Note increased firing during left turn trials with left sweeps compared to left turn trials with right sweeps corresponding to a significantly negative Sweep Direction Selectivity Index value (SDSI: $p < 0.01$, permutation test).

(Figure caption continued on the next page)

(Figure caption continued from the previous page)

(D) Same as in C but for a right turn cell (Cell 2) during right turn trials. Data taken from a different session as in A-C. Note increased firing during right turn trials with right sweeps compared to right turn trials with left sweeps corresponding to a significantly positive SDSI value ($p < 0.05$, permutation test). **(E)** Correlation between TDSI and SDSI across all cells whose activity was significantly modulated with sweep direction ($n = 56$ cells, Pearson $r = 0.61$, $p < 0.001$). **(F)** Firing rate modulation of sweep-selective turn cells during trials with sweeps only in the cell's preferred direction, non-preferred direction, or both directions, normalized by the cell's firing during trials without sweeps. Note bidirectional modulation of firing compared to the no sweep condition (preferred/non-preferred only: $p < 0.001$, both: $p > 0.05$, 1-sample t-tests, Bonferroni-corrected). These distributions were significantly different from one another (pref. vs both: $p < 0.01$, pref. vs non-pref: $p < 0.001$, and both vs non-pref: $p < 0.001$, paired t-tests, Bonferroni-corrected).

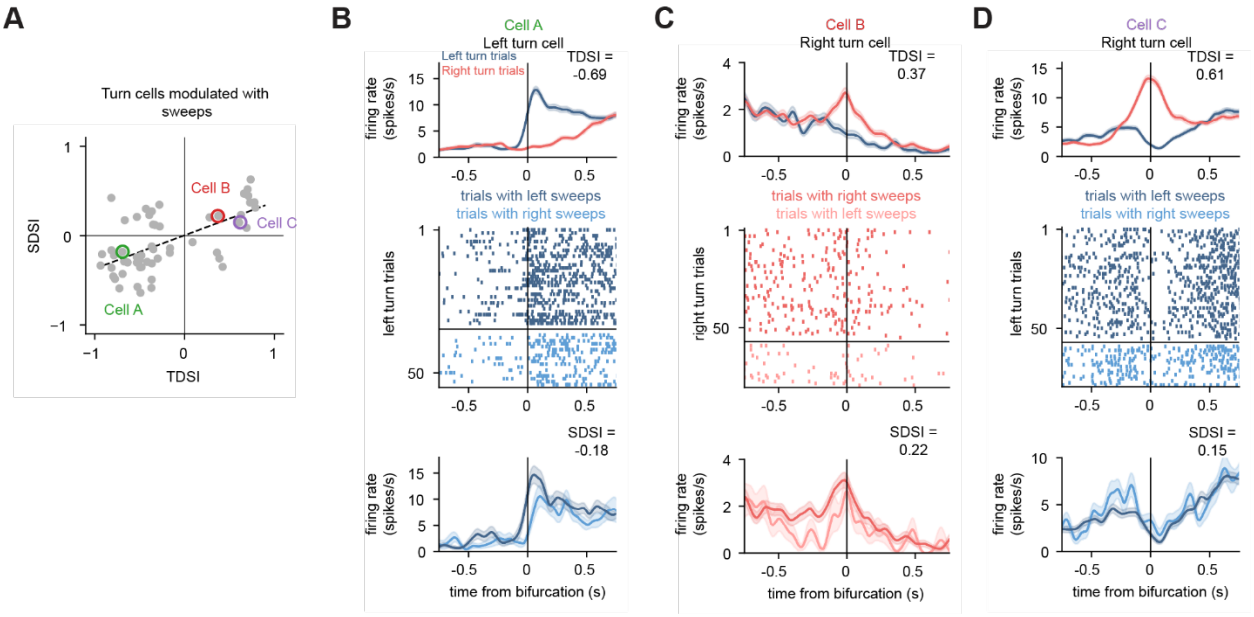

Figure 3.6 Additional examples of sweep-selective turn cells
(A) Same scatter plot as in Figure 3.5E. Markers indicate three additional sweep selective turn cells shown in panels B-D. **(B)** Example of left turn cell firing more during left turns with left sweeps compared to left turns with right sweeps ($p < 0.05$, permutation test). **(C)** Example of right turn cell firing more during right turns with right sweeps compared to right turns with left sweeps ($p < 0.01$, permutation test). **(D)** Example of right turn cell firing more during left turns with right sweeps compared to left turns with left sweeps ($p < 0.05$, permutation test).

3.3 Hippocampal representations of future paths reliably predict subsequent turn cell activity

Hippocampal sweeps can occur at various time points prior to the bifurcation. How early before the bifurcation do sweeps predict the activity of dSC cells at the bifurcation? To address this question, we used generalized linear models (GLMs, see Methods). As sweeps typically occurred in-phase with the hippocampal theta rhythm (**Figure 3.4C**), we divided each trial into theta cycles prior to and at the time of the bifurcation (cycles −4 through −1 and cycle 0, respectively) and, for each of these cycles, assessed whether the presence and direction of sweeps predicted dSC firing at the bifurcation (**Figure 3.7A**).

Strikingly, sweeps occurring up to 4 cycles (~500 ms) before the bifurcation could significantly predict dSC activity at the bifurcation (**Figure 3.7B,** $p < 0.01$, Wald z-tests). Predictive cycles (i.e. theta cycles during which sweeps significantly predicted changes in dSC activity at the bifurcation) were observed for 50% of sweep-selective turn cells and for 7.6% of all possible cycles (**Figure 3.7B**, cells: 21/42, cycles: 32/420), both of which significantly exceeded shuffled controls (**Figure 3.8A**, shuffled data: cells, 29 ± 0.2%, $p = 0.001$; cycles, 4.1 ± 0.03%, $p < 0.001$, permutation tests). Most predictive cycles were driven by sweeps in a cell's preferred turn direction (72%, 23/32). Of these, most cycles predicted increases in activity (**Figure 3.7B, top panels**, 96%, 22/23), whereas, for predictive cycles driven by sweeps in a cell's non-preferred direction (28%, 9/32) most cycles predicted decreases in activity (**Figure 3.7B, bottom panels**, 67%, 6/9 cycles).

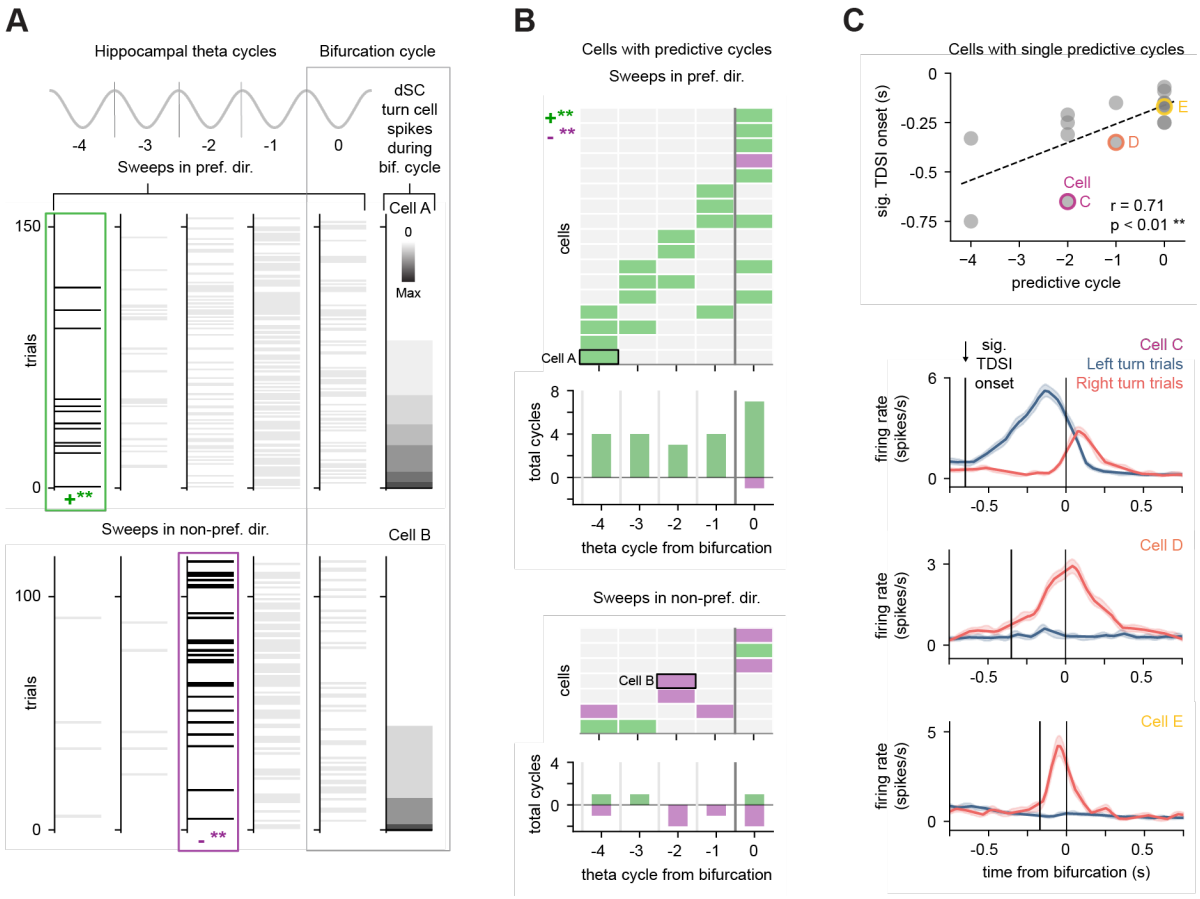

Figure 3.7 Hippocampal sweeps reliably predict future turn cell activity
(A) GLM analysis to assess whether the presence and direction of hippocampal sweeps during individual theta cycles prior to and at the time of the bifurcation (cycles -4 through -1 and cycle 0, respectively) predicts dSC turn cell firing at the bifurcation. Top, GLM analysis for an example dSC turn cell (Cell A). Spike count for Cell A during the bifurcation cycle (cycle 0) is shown at the far right. Trials are sorted by increasing spike counts of Cell A. Hippocampal sweeps in Cell A's preferred turn direction across trials are plotted as horizontal lines during their corresponding theta cycle relative to the bifurcation (cycles -4 through 0). Trials are those in which the animal turns in the cell's preferred turn direction. Note that sweeps occurring during cycle -4 are associated with increases in spiking of Cell A during the bifurcation cycle. Significantly positive (+**) predictive cycle is shown by a green outline ($p < 0.01$, Wald z-tests). Bottom, GLM analysis for another example turn cell (Cell B) in which sweeps in Cell B's non-preferred turn direction are shown. Note that sweeps occurring during cycle -2 across trials are associated with decreases in spiking of Cell B during the bifurcation cycle. Significantly negative (-**) predictive cycle is shown by a purple outline ($p < 0.01$, Wald z-tests). Sweeps occurring during significantly predictive cycles are shown in black to highlight the relationship between sweeps and turn cell firing. Sweeps occurring during non-significantly predictive cycles are shown in gray. **(B)** Top, all cells with predictive cycles for sweeps in the cell's preferred turn direction sorted by theta cycle relative to the bifurcation. Bottom, all cells

(Figure caption continued on the next page)

(Figure caption continued from the previous page)

with predictive cycles for sweeps in the cell's non-preferred turn direction. **(C)** Top, correlation between timing of predictive cycle and onset of significant TDSI across turn cells. This analysis was necessarily done only on cells whose activity was either positively or negatively predicted by sweeps during a single theta cycle (n = 16 cells, Pearson r = 0.71, p < 0.01). Bottom, firing rate profiles of three example turn cells (Cell C, D, and E from top plot) showing progressively later significant TDSI onsets relative to the turn.

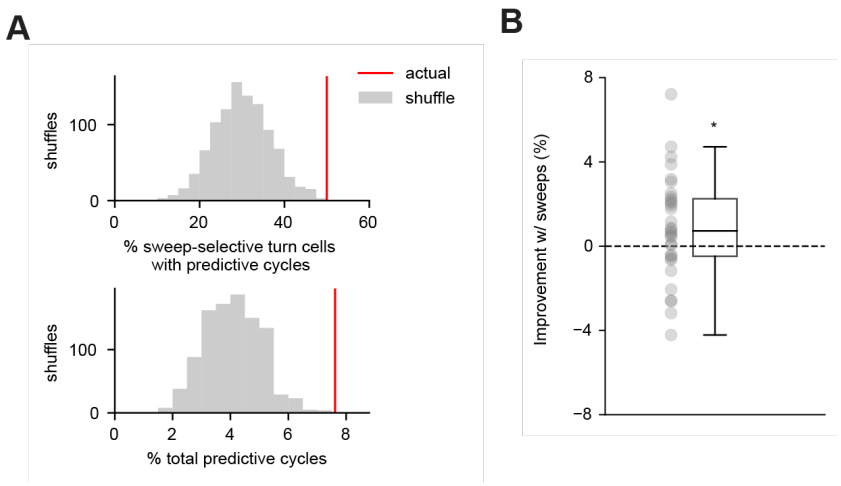

Figure 3.8 GLM shuffle controls and cross-validation for Figure 3.7
(A) Top, distribution of the percentage of sweep-selective turn cells with predictive cycles after shuffling spike counts across trials to disrupt sweep-firing relationships (n = 1000 shuffles, shuffled: 29% ± 0.2%, actual = 50%, p = 0.001: 1 shuffle had a percentage of sweep selective turn cells that exceeded that of the actual data). Bottom, same as top but for percentage of significantly predictive cycles (n = 1000 shuffles, shuffled: 4.1% ± 0.03%, actual = 7.6%, p < 0.001: 0 shuffles had a percentage of predictive cycles that exceeded that of the actual data). **(B)** Model improvement with sweep information compared to turn direction information alone for each significantly predictive cycle (n = 32 cycles from Figure 3.7B, mean: 0.89 ± 0.43 % (s.e.m.), 95% CI [0.054, 1.72] %, p < 0.05, 1-sample t-test compared to 0). Model improvement is defined as percentage reduction in mean absolute error (MAE) when adding sweep predictors (full model) to a turn-only model (reduced model), calculated as: (MAE reduced model - MAE full model) / MAE reduced model × 100. Positive values indicate model improvement with sweeps. For cross-validation, values were calculated and averaged across folds of a 5-fold train-test split.

Distinct dSC turn cells become directionally selective at different times prior to the bifurcation (-248 ± 216 ms, average ± s.d., **Figure 3.3C, top panel**). This raises the possibility that those dSC turn cells that showed earlier directional selectivity would also

be those whose firing, at the bifurcation, is modulated in coordination with early sweeps. This was indeed the case: we found a positive correlation between the time of predictive cycles and time at which turn cells became directionally selective (**Figure 3.7C, top panel**, Pearson $r = 0.72$, $p < 0.01$). In other words, sweeps occurring during earlier theta cycles predicted the activity of turn cells that became directionally selective earlier, and vice versa. Thus, hippocampal sweeps can predict turn-related activity in the dSC, and the timing of this predictability is related to the time at which individual turn cells become directionally selective.

3.4 Turn cell activity does not reliably predict hippocampal representations of future paths

Given that hippocampal sweeps can predict dSC activity at the bifurcation, we next asked whether an interaction in the opposite direction also occurred. That is, can dSC activity prior to the bifurcation predict hippocampal sweeps at the bifurcation? This possibility would be consistent with a direct influence of head turning behavior on hippocampal representations (Redish, 2016). To address this question, we again turned to GLMs (see Methods). Mirroring the GLM analysis above (**Figure 3.7**), we divided each trial into theta cycles prior to and at the time of the bifurcation and, for each of these cycles, assessed whether dSC activity predicted the presence and direction of hippocampal sweeps at the bifurcation.

We identified only a single instance of a significant cycle in which dSC turn cell activity predicted hippocampal sweeps at the bifurcation (**Figure 3.9A**, $p < 0.01$, Wald z-test). Additional analyses using a less conservative significance threshold yielded only weak effects that did not robustly exceed shuffled controls (**Figure 3.9B** and **3.9C**). Thus,

while hippocampal sweeps reliably predict dSC activity at the bifurcation, dSC activity does not reliably predict hippocampal sweeps.

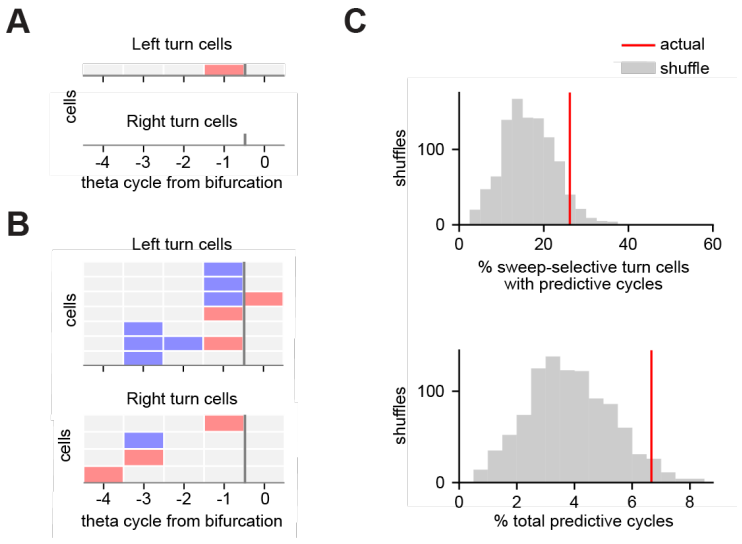

Figure 3.9 Turn cell activity does not reliably predict future hippocampal sweeps
(A) GLM analysis to assess whether dSC turn cell activity during individual theta cycles prior to and at the time of the bifurcation (cycles -4 through -1 and cycle 0, respectively) can predict the presence and direction of hippocampal sweeps at the bifurcation. Shown are all cells with predictive cycles at a $p < 0.01$ threshold (Wald z-tests). Shaded red boxes indicate cycles during which dSC firing predicted rightward sweeps at cycle 0. Shaded blue boxes, if present, indicate cycles during which dSC firing predicts leftward sweeps at cycle 0. Note that only activity for one left turn cell at cycle -1 predicted rightward sweeps at cycle 0, and no right turn cells exhibited predictive cycles. **(B)** All left and right turn cells with predictive cycles at a $p < 0.05$ threshold (Wald z-tests) sorted by theta cycle relative to the bifurcation. Color code is same as in A. Note increased number of cells with predictive cycles (i.e. theta cycles during which dSC activity significantly predicted sweeps at the bifurcation) compared to A. **(C)** Shuffle controls for cells and cycles in B ($p < 0.05$ threshold). Top, distribution of the percentage of sweep-selective turn cells with predictive cycles after shuffling spike counts across trials to disrupt firing-sweep relationships (n = 1000 shuffles, shuffled: 17 ± 0.2%, actual = 26%, $p = 0.079$: 79 out of 1000 shuffles had a percentage of sweep selective turn cells that exceeded that of the actual data). Bottom, same as top but for percentage of significantly predictive cycles (n = 1000 shuffles, shuffled: 3.9 ± 0.04%, actual = 6.7%, $p = 0.047$).

3.5 Hippocampal representations of future paths are associated with deviations in behavioral trajectory and changes in trial duration

dSC activity impacts turning behavior. Given that the direction of hippocampal representations of future paths predicts differences in dSC activity, we asked whether it also predicts differences in the animal's behavior. This was indeed the case.

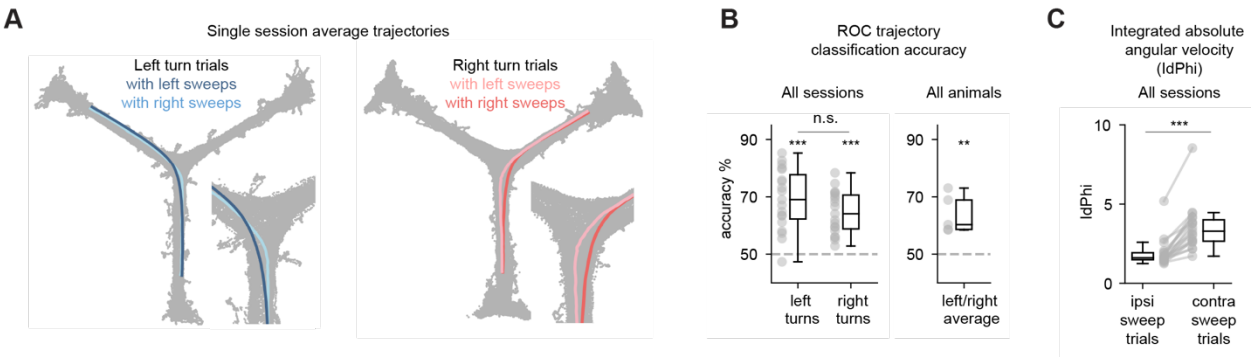

Figure 3.10 Hippocampal sweep direction and deviations in behavioral trajectory around the turn
(A) Left, average left turn trajectories for a single session color coded by sweep direction. Dark blue trajectory indicates average of left turn trials with left sweeps (ipsi sweep trials), light blue trajectory indicates average of left turn trials with right sweeps (contra sweep trials). Session is the same session as in Figure 3.5A, 3.5B, and 3.5C. Note deviation of trajectory for contra sweep trials toward the alternative path. Right, same as in A but for right turn trials. Session is the same session as in Figure 3.5D. **(B)** Left, ROC classification accuracy of sweep direction from deviation in behavioral trajectory from a linear path around the time of turns (See Methods), shown across sessions for both turn directions (n = 19 sessions, left turns: 69 ± 0.02%, right turns: 64 ± 0.02%, left and right turns: $p < 0.001$, 1-sample t-tests compared to 50%, Bonferroni-corrected; left vs. right turns: $p > 0.05$, paired t-test). Right, ROC classification accuracy between ipsi and contra sweep trials, combined across left and right turns per animal (n = 5 animals, 64 ± 0.03%, $p < 0.01$, 1-sample t-test compared to 50%). **(C)** Integrated absolute angular velocity (IdPhi) values calculated across the average trajectories for ipsi vs. contra sweep trials for each session (n = 19 sessions, $p < 0.001$, paired t-test). Values are averaged between left and right turns.

First, for a given turn direction, turns were tighter during ipsi sweep trials compared to contra sweep trials (**Figure 3.10A**). Trajectories during contra sweep trials deviated more from a linear path and exhibited greater cumulative angular change (IdPhi (Andrew

E. Papale et al., 2016)) compared to ipsi sweep trials (**Figure 3.10B** and **3.10C**, see Methods). Second, we observed an effect of sweep presence and direction on trial duration. Trials without sweeps had the shortest duration (median: 1.73 s), followed by ipsi sweep trials (1.83 s), contra sweep trials (1.95s), and trials with sweeps in both directions (2.22 s; **Figure 3.11A**). Consistent with this effect, running speed was highest on trials without sweeps (median: 34.1 cm/s), followed by ipsi sweep trials (32.1 cm/s), contra sweep trials (31.2 cm/s), and trials with sweeps in both directions (27.5cm/s; **Figure 3.11B**). Thus, the movement trajectory of the animal around the turn and its running speed reflect the presence and direction of hippocampal sweeps.

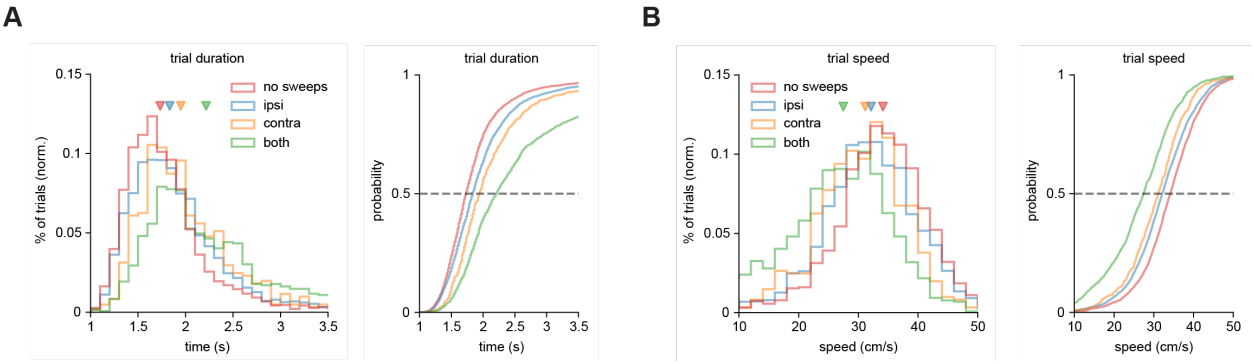

Figure 3.11 Effects of sweep presence and direction on trial duration and speed
(A) Left, trial durations for trials with no sweeps (n = 2810 trials, red), ipsi sweeps (n = 3944, blue), contra sweeps (n = 607, orange), and both ipsi and contra sweeps (n = 1290, green) pooled across sessions and animals (n = 19 sessions, 5 animals). Markers indicate medians of each group (1.73, 1.83, 1.95, and 2.22 s; IQRs: 1.52–2, 1.58–2.18, 1.68–2.35, 1.82–2.95 s, respectively, $p < 0.001$ for all comparisons, Mann-Whitney U tests, Bonferroni-corrected). Right, cumulative plot of each distribution in the left panel. **(B)** Left, trial speeds for trials with no sweeps, ipsi sweeps, contra sweeps, and both ipsi and contra sweeps pooled across sessions and animals as in A. Speed was calculated as a single value across each trial as 2D distance traveled divided by trial duration. Markers indicate medians of each group (34.1, 32.1, 31.2, 27.5 cm/s; IQRs: 29.6-38.9, 27.3-37.2, 26.0-35.4, 21.3-32.7 cm/s, respectively, $p < 0.001$ for all comparisons, Mann-Whitney U tests, Bonferroni-corrected). Right, cumulative plot of each distribution in the left panel.

Discussion

We identified a consistent, predictive relationship between representations of possible future paths in the hippocampus and the activity of midbrain dSC neurons associated with turning behavior. Furthermore, consistent with the role of dSC activity in biasing turns, when the hippocampus represented possible paths that were not ultimately taken, movement trajectories were nonetheless biased toward those paths, demonstrating that animals partially turned toward possible futures that were considered but not selected.

It has long been suggested that the mere idea of a movement, unless inhibited, automatically triggers the movement itself (James, 1890). This suggestion has led to the proposal that all cognitive processes go on in terms of 'faint reinstatements' of overt motor acts (Watson, 1913). Indeed, numerous studies, including ours, have shown that cognitive processes can 'leak' into overt behavior (Calalo et al., 2025; Cazettes et al., 2025; Cowen & McNaughton, 2007; Euston & McNaughton, 2006; Korbisch et al., 2022). We propose that such leakage reflects the engagement of motor circuits by cognitive processes (Craighero & Rizzolatti, 2005; Jeannerod, 2001; Rizzolatti et al., 1987; Tse, 2025), which in turn may enable cognitive representations to guide behavior.

Previous work examining the relationship between hippocampal sweeps and behavior has primarily focused on vicarious trial and error (VTE) wherein animals' heads deviate to the left and/or right as they approach a decision point (Johnson & Redish, 2007; Redish, 2016). VTE is not dependent on the hippocampus (Clark et al., 2005; A. E. Papale, 2015), but whether VTE could be driven by hippocampal activity was unclear. Our results demonstrate a clear relationship between hippocampal representations of

future paths and deviations from ballistic turns that have been associated with VTE, pointing to a potentially direct role of mental simulations of possible futures in altering the microstructure of behavior.

How might such mental simulations be transformed into motor output to guide behavior? Our results provide support for an integration-like mechanism in the dSC related to representations of possible futures. Previous work has demonstrated that integration is a key function of the dSC, wherein inputs related to orienting decisions drive progressive increases in activity that, upon reaching a threshold, drives action (Dorris et al., 1997; Jantz et al., 2013; Paré & Hanes, 2003; Sparks et al., 2000). Our GLM analysis shows that hippocampal sweeps occurring up to 4 theta cycles (~500 ms) before the maze bifurcation can predict dSC activity at the time of the bifurcation (**Figure 3.7A** and **3.7B**). This timing suggests that hippocampal sweeps may be integrated to modulate dSC turning commands, perhaps in a sequential manner aligned with the time at which individual turn cells become directionally selective (**Figure 3.7C**), to bias turns toward behaviorally relevant locations in nearby space (Tang et al., 2025; Vollan et al., 2026; Yu et al., 2025). In this situation, hippocampal input to the dSC could be critical for selecting among possible turn directions.

By contrast, evidence for an interaction in the opposite direction, in which dSC activity influences hippocampal sweeps, was limited (**Figure 3.9**). This asymmetry suggests that, rather than forming a bidirectional loop, hippocampal non-local activity may preferentially influence dSC activity during online behavior. Interestingly, a recent study in mice showed that SC activity is causally related to changes in virtual heading during REM sleep (Senzai & Scanziani, 2024), suggesting that, conversely, SC activity may

preferentially influence internal representations during offline behavior. These results raise the possibility that the direction of information flow between cognitive and motor systems may shift across online and offline states (Buzsáki, 1989; Hasselmo, 1999): during online states, when behavioral control is most critical, cognitive representations may selectively bias motor activity to guide action, whereas during offline states, motor activity may play a greater role in the formation and refinement of internal models (Hobson et al., 2014; Senzai & Scanziani, 2024).

Cognitive abilities such as imagination, planning, and decision-making involve mentally exploring possible options (Comrie et al., 2022; Kay et al., 2020). To guide behavior, these mental explorations must, at some level, influence neural circuits that generate action. Here we show that when the brain simulates a possible future path, it also engages motor commands that actively guide the animal toward that path. We speculate that this engagement may allow cognitive circuits to harness ongoing motor dynamics (Rączaszek-Leonardi, 2023) to steer behavior along internally represented trajectories.

Methods

Experimental model and animals

Neural activity was recorded from five male C57BL/6J mice (Jackson Laboratory #000664, 5-6 months old). All mice were housed on a reversed cycle (light/dark cycle 12/12h) with littermates before experimentation and singly housed in enriched cages during food-restriction and experimentation. All procedures were conducted in accordance with the regulations of the University of California San Francisco Institutional Animal Care and Use Committee (IACUC).

Behavioral training and electrode implantation

Implantations were performed in two phases on two distinct days. First, the implantation of the headplate, and second, the implantation of the silicon probes. Mice were implanted under 2% isoflurane anesthesia. The headplate was placed on the skull with dental cement (Unifast LC, GC America; Optibond Universal, Kerr Dental). After post-operative recovery of five days, mice were deprived of food to 85% of their baseline weight and pretrained to run on a 1 m linear track for liquid food reward (sweetened evaporated soymilk). After pretraining for 1-3 days on the linear track, mice were pretrained on the Y-maze task for 3-5 days (see Y-maze task and trial segmentation) and implanted with silicon probes. Silicon probes were mounted on 3D-printed microdrives to record unilaterally from the superior colliculus (SC) and from the CA1 region of the hippocampus in the opposite hemisphere. The types of probes used included: Single-shank (Diagnostic Biochips (DBC) P64-4), four-shank (DBC P64-1, DBC P128-6), and eight-shank probes (DBC P128-8). Probe shanks were inserted through craniotomies at the coordinates described in the Electrode insertion, electrode

coordinates, histology and recording site assessment section below. The shanks were initially lowered to 0.7-1.2 mm (SC) and 0.6 mm (CA1) below brain surface and the microdrive was then fixed to the headplate. A ground electrode (0.005” diameter stainless wire, A-M systems) was inserted in the cerebellum. After post-operative recovery, mice were placed back on the Y-maze training protocol for 1-5 days while the shanks were lowered to the intermediate and deep SC (dSC) and to CA1 to ensure that peak Y-maze performance coincided with the time at which the recording sites reached their targets. Mice remained on food restriction for the remainder of the experiment.

Electrophysiological recordings and video tracking

The data presented in this paper are from three to four 60-140 min sessions per mouse on the Y-maze task. Electrophysiological data were acquired using an Intan RHD2000 system (Intan Technologies LLC) band-pass filtered between 0.1 Hz and 7.5 kHz and digitized at 20 kHz. Spike sorting was performed semi-automatically, using Kilosort 2.0 and Phy (Pachitariu et al., 2023). Video data was acquired at 60 frames per second using a CMOS camera (Basler acA1300-200um) placed above the maze. A machine-learning algorithm, DeepLabCut (Mathis et al., 2018), was trained to track features of the probe housing and distinct body parts of the mice (microdrive probe base (head), left and right ears, base of the tail). For position analysis and trial segmentation on the Y-maze, the probe base position (head position) was used as the actual position of the mouse.

Y-maze task and trial segmentation

Mice navigated an elevated Y-maze (arm length: 45 cm, arm width: 5 cm) in search of liquid food reward, which was dispensed from two out of three ports at the

ends of each arm. The task consisted of six to eight 50-80 trial blocks, with the locations of the active ports switching in an uncued manner between blocks. The active ports were chosen randomly within each block. Animals could not visit the same port on consecutive trials to receive a reward, so mice learned to alternate between the active ports. For trial segmentation, we used the track_linearization package (LorenFrankLab, 2024) to map the animal's position on the Y-maze to a one-dimensional representation with a corresponding maze arm identifier. We then defined a position threshold at 70% of the length of each maze arm (31.5 cm measured outward from the center of the maze or 13.5 cm measured inward from the end of the arm). Trials were defined as periods from when the animal, after leaving a reward port, crossed the position threshold of one arm, made a turn, and crossed the position threshold of another arm without entering any other arms. The time at which an animal reached the bifurcation was defined as the time at which the animal's linearized head position transitioned from one arm to another at the center of the maze. Animals took ~1.8 seconds to complete each trial (median: 1.85 s, IQR: 1.58-2.23 s, n = 8651 trials across 5 mice).

Head angle relative to the track and time of behavioral divergence

Head angle relative to the track was defined as the angle between the animal's head direction vector (given by the vector perpendicular to the line connecting the ears) and the midline of the track segment from which the animal approached the bifurcation. The time of behavioral divergence was defined as the time at which the animal's head angle relative to the track significantly diverged between left and right turns. To determine the average time of behavioral divergence across sessions and animals (n = 19 sessions, 5 animals, **Figure 3.3B**), we calculated a Behavioral Divergence Index (BDI) as the

difference between session-averaged head angles relative to the track for left and right turn trials. BDI was calculated within 200 ms windows advanced in 20 ms steps from 0.85 s before to 0.85 s after the time at which the animal reached the bifurcation. BDI significance was assessed using a permutation test: for each window, a null distribution was generated by randomly permuting left and right turn labels across sessions (10,000 permutations) and recalculating BDI from the resulting averages. Windows were considered significant only when the observed BDI was more extreme than all shuffled values ($p < 1/10,000$). The time of behavioral divergence was defined as the earliest time window belonging to a continuous sequence of such significant windows.

Electrode insertion, electrode coordinates, histology and recording site assessment

In three mice, the right SC was targeted; and in two mice, the left SC was targeted. Lambda was used as the skull reference for SC craniotomies, while bregma was used for hippocampal craniotomies. The SC was targeted by a craniotomy at AP: 0 mm from lambda, ML: ± 2.5 mm, and the silicon probe was inserted at a 32^{o} angle from vertical along the anterior-posterior axis of the SC. The CA1 region of the hippocampus was targeted in the opposite hemisphere by a craniotomy at AP: -2.0 mm from bregma, ML: ± 1.5 mm, and the silicon probe was inserted vertically at a 45^{o} angle relative to the sagittal plane along the long axis of the hippocampus. Prior to implantation, the backs of all probe shanks were coated with DiI solution (Fisher, V22885) for probe track localization using a fluorescence microscope (**Figure 3.2A**). The shanks were initially lowered to 0.7-1.2 mm (SC) and 0.6 mm (CA1) below the surface of the brain (dorsoventral, DV) and advanced over consecutive days to reach the dSC and cell body layer of CA1. The dSC was targeted using DV coordinates and CA1 was targeted using DV coordinates and

physiological signatures such as sharp-wave ripples. Once the target regions were reached, dSC probes were advanced between sessions (days) to record from different neurons while CA1 probes were slightly advanced between sessions to maintain maximal units for decoding. For the dSC, the average depth for the first recording was DV: -1.51 ± 0.13 mm measured from the topmost channel of the probe while the average depth for the last recording was DV: -2.96 ± 0.06 mm measured from the bottommost channel of the probe (**Figure 3.2B, left panel**). For CA1, average depths were DV: -1.00 ± 0.11 mm and DV: -1.39 ± 0.10, respectively (**Figure 3.2B, right panel**).

For anatomical analysis, mice were perfused transcardially with phosphate-buffered saline (PBS) and then with 4% paraformaldehyde (PFA) in PBS. Brains were extracted, stored in 4% PFA overnight at 4^{o}C and cut with a vibratome to 100 µm thick coronal sections. Slices were mounted in DAPI Vectashield (Vector Laboratories H1500) and fluorescence images were acquired with an Olympus MVX10 MacroView microscope. Probe tracks were identified using the DiI signal.

Turn Direction Selectivity Index (TDSI) and turn cells

Turn selectivity was quantified using a Turn Direction Selectivity Index (TDSI), calculated as the difference between the average firing rates during right and left turns divided by their sum ((Right FR - Left FR) / (Right FR + Left FR)) over a 200 ms window centered on the time of the cell's peak firing rate. Thus, right turn cells were defined by positive values and left turn cells by negative values. To obtain firing rates, spike trains were converted to binary vectors, smoothed with a Gaussian kernel (50 ms), normalized by the kernel width, and averaged across trials. To determine the time window for the TDSI calculation, we first defined a wide window of ± 0.5 s around the time at which the

animal reached the bifurcation and, for each neuron, identified within this window the time of peak firing rate for either left or right turns (whichever was greater) using the neuron's average firing rate across all arms. TDSI was then computed across each arm within a narrow window of ± 0.1 s centered on this peak firing time.

TDSI significance was assessed using a permutation test. For each neuron and maze arm, left and right turn trials were pooled together and randomly reassigned into two groups whose sizes matched the original sample sizes. TDSI was then recomputed within the narrow window centered on the same actual peak firing time. This procedure was repeated 1000 times to generate a shuffled distribution of TDSI values. For right turn cells, the p-value was defined as the fraction of shuffled TDSI values that were greater than or equal to the observed TDSI, or less than or equal to the observed TDSI for left turn cells. Turn cells were defined as neurons whose TDSI retained the same sign and remained significant ($p < 0.05$) across all maze arms.

Instantaneous TDSI and significant TDSI onset

We computed instantaneous TDSI across the entire trial period (Felsen & Mainen, 2008) to determine the time at which turn cells became directionally selective (significant TDSI onset, **Figure 3.3A**). TDSI was calculated within 200 ms windows advanced in 20 ms steps from 0.85 s before to 0.85 s after the time at which the animal reached the bifurcation. TDSI significance was assessed with a permutation test: for each window, left and right turn labels were randomly permuted across trials and TDSI was recomputed. This process was repeated 500 times to generate a null distribution for each window. Windows were considered significant when the observed TDSI was more extreme than all shuffled values ($p < 1/500$). Significant TDSI onset was defined as the earliest time

point at which a turn cell exhibited two consecutive significant TDSI windows in the expected direction (e.g., for a left turn cell, two consecutive significant TDSI windows with negative TDSI).

Spatial decoding from hippocampal activity

We used an established state space algorithm (Denovellis et al., 2021) to decode spatial position from populations of clustered hippocampal neurons. Briefly, for each session we built an encoding model to relate hippocampal spiking to the animal's linearized head position in 1 ms bins. We then decoded position from hippocampal spiking in 0.5 cm linear position bins and 1 ms temporal bins. For cross-validation, we trained the encoding model on 75% of the data in each session and tested it on the remaining 25%, repeating this across four folds. We used a single-state continuous, causal decoding model (Denovellis et al., 2021) in which the continuous state was modeled by a random walk transition matrix with a 9.6 cm movement variance. To obtain the decoded position, the posterior probability distribution of position was first smoothed across spatial bins (i.e., along the position axis) using a 2.5 cm moving window. The decoded position in each time bin was then defined as the location of the peak of this smoothed posterior. For each time bin, we also classified the animal's actual and decoded positions into one of three maze arms.

Identification of hippocampal sweeps from decoded position

Sweep times were identified as times during trial periods (i.e., during locomotion) in which the decoded position was in a maze arm distinct to the animal's actual position for at least 15 consecutive time bins (15 ms). This duration requirement was used to prevent rapid, spurious jumps in the decoded position from being identified as sweeps. Only

sweeps that occurred prior to the bifurcation were analyzed. Sweeps were classified as ipsi sweeps if they proceeded into the maze arm that the animal would eventually take or contra sweeps if they proceeded into the alternative arm. For trial-based analyses, trials were classified as ipsi sweep trials (containing only ipsi sweeps (1 or more)), contra sweep trials (containing only contra sweeps), trials with sweeps in both directions (containing both ipsi and contra sweeps), or trials without sweeps.

To compare the sweeps identified here in mice to those observed in rats, we extracted several key features of ipsi and contra sweeps including their timing relative to the hippocampal theta cycle, how far they swept ahead of the animal, and their density around the time of block switches (**Figure 3.4**). Mirroring hippocampal sweeps observed in rats, ipsi and contra sweeps occurred preferentially during late phases of the theta cycle (0 to π rad., **Figure 3.4C**, (Comrie et al., 2024; Kay et al., 2020; Vollan et al., 2025)) and swept one body length ahead of the animal on average (~9 cm here, **Figure 3.4B**, ~25 cm in rats (Comrie et al., 2024; Vollan et al., 2025)). Furthermore, consistent with a recent report in rats (Comrie et al., 2024), we observed a transient increase in the density of contra sweeps relative to ipsi sweeps after trial block switches (**Figure 3.4D**). Thus, the hippocampal sweeps reported here in mice exhibit strikingly similar features to those in rats.

Sweep direction selectivity index (SDSI)

To investigate the relationship between dSC turn cell firing and sweep direction, we took advantage of the fact that, for a given turn direction, some trials contain ipsi sweeps and others contain contra sweeps. Thus, for trials in a given turn direction, we could assess whether the activity of individual dSC turn cells varied depending on the direction

of hippocampal sweeps. As this analysis necessarily required trials with only ipsi or contra sweeps, we excluded trials with sweeps in both directions and trials without sweeps.

For each dSC turn cell, we then computed a sweep direction selectivity index (SDSI) around the bifurcation separately for all left turn trials and all right turn trials. SDSI was calculated as the difference between the average spike count during all trials with right sweeps and the average spike count during all trials with left sweeps, divided by their sum ((Right sweep spike count - Left sweep spike count) / (Right sweep spike count + Left sweep spike count)), where spike counts were taken from a 200 ms window centered on the time that the animal crossed the bifurcation (t = 0). Thus, for a given turn direction, cells that fired more at the bifurcation during trials with right sweeps were defined by positive SDSI values and cells that fired more during trials with left sweeps by negative SDSI values.

SDSI significance was assessed using a permutation test. For each neuron and turn direction, all trials with right sweeps and all trials with left sweeps were pooled together and randomly reassigned into two groups whose sizes matched the original sample sizes. SDSI was then recomputed. This procedure was repeated 1000 times to generate a shuffled distribution of SDSI values. For cells that fired more during trials with right sweeps, the p-value was defined as the fraction of shuffled SDSI values that were greater than or equal to the observed SDSI, or less than or equal to the observed SDSI for cells that fired more during trials with left sweeps. Thus, each cell was assigned an SDSI value and an associated p-value for each turn direction. SDSI values were deemed significant if their associated p-value was less than 0.05.

Of the turn cells with a significant SDSI value in one or both turn directions (38%, 64/167), the vast majority were selective in only one turn direction (88%, 56/64). We restricted subsequent analyses to this majority population as each cell had a single significant SDSI value that could be directly compared to its TDSI (**Figure 3.5E**). Across this population, most cells fired more during trials with sweeps in their preferred turn direction compared to trials with sweeps in their non-preferred turn direction ('sweep-selective turn cells', 75%, 42/56, bottom left and top right quadrants of **Figure 3.5E**). Of these, most cells (62%, 26/42) exhibited sweep direction selective firing during trials in which the animal turned in the cell's preferred direction (**Figure 3.5C** and **3.5D**, **Figure 3.6B** and **3.6C**) while the rest exhibited selectivity when the animal turned in the cell's non-preferred direction (**Figure 3.6D**). Together, these results reveal that turn cell activity is modulated in coordination with sweeps primarily during trials in which the animal turns in the cell's preferred direction.

Sweep-selective turn cell activity relative to trials without sweeps

To determine whether the activity of sweep-selective dSC neurons can be bidirectionally modulated, that is increase or decrease their firing in coordination with sweep presence and direction, we analyzed the firing rates of sweep-selective turn cells (n = 42) around the time of the bifurcation across three distinct trial types: trials with sweeps 1) only in the cell's preferred direction, 2) only in the cell's non-preferred direction, and 3) in both directions, all relative to trials without sweeps.

For each sweep-selective turn cell, we calculated a normalized firing rate modulation score for each of the three distinct trial types above as the difference between the average spike count during that trial type and the average spike count during trials

without sweeps, divided by their sum ((trial type spike count – no sweep spike count) / (trial type spike count + no sweep spike count)), calculated over the same 200 ms bifurcation window used for SDSI. Accordingly, each sweep-selective turn cell was assigned a modulation score for each trial type (**Figure 3.5F**). Positive values indicate that a cell fired more on average during that trial type compared to no sweep trials, negative if it fires less, and near zero if there is no change.

Generalized linear models for assessing if hippocampal sweeps predict turn cell firing

We built Poisson family generalized linear models (GLMs, logit link function) to determine whether and when hippocampal sweeps prior to the bifurcation could predict dSC activity at the bifurcation across trials (**Figure 3.7**). We included trials with sweeps exclusively in one direction (ipsi or contra) as well as trials without sweeps, excluding trials with sweeps in both directions.

We divided each trial into theta cycles prior to and at the time of the bifurcation (cycles −4 through −1 and cycle 0, respectively) and, for each cycle, extracted three binary predictors across trials: turn direction (left = 1, right = 0), left sweep (1 or 0), and right sweep (1 or 0). For each sweep-selective turn cell (n = 42), the response variable was defined as the spike count across trials during the bifurcation cycle (cycle 0). Importantly, separate GLMs were fit for each cycle (-4 through 0), with predictors drawn from that cycle and the response variable fixed as turn cell spike counts at cycle 0.

For each turn cell, we extracted the beta coefficients for the left and right sweep predictors from each GLM, resulting in 10 beta coefficients per cell (2 sweep directions x 5 theta cycles). The significance of each coefficient was assessed using a Wald z-test. Significant beta coefficients using a conservative threshold ($p < 0.01$) were converted to

their sign (±1), indicating whether sweeps during a given theta cycle significantly predicted increased firing (+1, green-colored cycles in **Figure 3.7**) or decreased firing (-1, purple-colored cycles in **Figure 3.7**) at the bifurcation cycle. Such cycles were deemed 'predictive cycles.'

We performed permutation tests (1000 iterations) to assess whether the observed proportion of turn cells with predictive cycles and the observed proportion of total predictive cycles exceeded chance. For each iteration, spike counts for each turn cell were shuffled separately within left and right turn trials to disrupt sweep-firing relationships. P-values for cells and cycles were calculated as the proportion of shuffles in which the shuffled statistic met or exceeded the observed values. Both the proportion of turn cells with predictive cycles and the proportion of predictive cycles significantly exceeded shuffled controls (**Figure 3.8A**).

To assess whether adding sweep predictors improved model performance for each significantly predictive cycle (n = 32 total cycles, **Figure 3.7B**), we compared a full model (turn direction predictors + sweep predictors) to a reduced model (turn direction predictors only) using 5-fold cross-validation. Model improvement was quantified as percentage reduction in mean absolute error (MAE) between the reduced model and the full model calculated as: (MAE reduced model - MAE full model) / MAE reduced model × 100. The observed positive values averaged across folds indicate that adding sweep predictors improved model prediction beyond turn direction alone (**Figure 3.8B**).

Generalized linear models for assessing if turn cell firing predicts hippocampal sweeps

We built binomial family GLMs (logit link function) to test whether and when dSC turn cell firing prior to the bifurcation could predict the direction of hippocampal sweeps

at the bifurcation across trials (**Figure 3.9**). For this analysis, we included trials with sweeps exclusively in one direction (ipsi or contra), excluding trials with sweeps in both directions as well as trials without sweeps.

As in the previous GLM analysis, we divided each trial into theta cycles spanning cycles −4 through 0 relative to the bifurcation. For each cycle, we extracted a binary turn-direction predictor (left turn = 1, right turn = 0) and spike counts for a given sweep selective turn cell across trials. For the response variable, we identified whether a hippocampal sweep occurred in cycle 0, and, if so, assigned sweep direction as left = 1 and right = 0. Importantly, separate GLMs were fit for each cycle (-4 through 0), with predictors drawn from that cycle and the response variable fixed as sweeps at cycle 0.

For each sweep-selective turn cell (n = 42), we extracted the beta coefficients for the spike-count predictors from cycles −4 through 0 in each GLM. The significance of each coefficient was assessed using a Wald z-test. Significant coefficients ($p < 0.01$) were converted to their sign (±1), indicating whether higher spike counts during a given theta cycle significantly predicted leftward sweeps (+1, blue-colored cycles in **Figure 3.9**) or rightward sweeps (−1, red-colored cycles in **Figure 3.9**) at the bifurcation. Interestingly, at the $p < 0.01$ level as in the previous GLM analysis, we observed only a single cycle in which dSC turn cell activity predicted sweeps at the bifurcation, and this cycle involved activity from a left turn cell predicting rightward sweeps (**Figure 3.9A**). Implementing a less conservative significance threshold ($p < 0.05$), we did observe an increased proportion of cells and cycles in which dSC turn cell activity predicted future sweeps in a directionally consistent manner (**Figure 3.9B**); however, after performing permutation

tests (1000 iterations, as described in the previous GLM analysis), we found that these proportions did not reliably exceed shuffled controls (**Figure 3.9C**).

Quantifying deviations in behavioral trajectory around the turn

We used two approaches to compare animals' behavioral trajectories around the bifurcation between ipsi and contra sweep trials.

The first involved quantifying trajectory divergence from a linear path. To obtain a linear path, we first calculated the average trajectories during ipsi and contra sweep trials for turns a given direction. We did so by interpolating each trial to the same number of samples and rotating them to a common coordinate frame (**Figure 3.10A**). We then defined a band of interest starting with an upper boundary near the bifurcation point of the maze and a lower boundary extending 10 cm from the upper boundary toward the base the maze. This band was chosen to focus on trajectory deviations immediately prior to the bifurcation. The linear path was defined by connecting the average positions at which the ipsi and contra sweep trajectories crossed the upper and lower boundaries of the band, producing a single linear path against which trajectory deviations were measured. We then calculated, within this band of interest, the deviation of each ipsi and contra sweep trial from the linear path as the average perpendicular distance from each sample point to the line, producing a single deviation value per trial.

For the ROC analysis, deviation values for ipsi and contra sweep trials were treated as two distributions, and an ROC curve was computed. The optimal classification threshold was found by minimizing the distance to the top-left corner of the ROC curve. We calculated the balanced classification accuracy (% accuracy, (true positive rate + true negative rate) / 2) to assess ROC performance. For each session, classification accuracy

was calculated separately for left and right turn trials (**Figure 3.10B, left panel).** For each animal, classification accuracies were averaged across turn directions and sessions (**Figure 3.10B, right panel**).

Trajectory deviations between ipsi and contra sweep trials were also quantified using the IdPhi measure (the integrated absolute angular velocity, (Andrew E. Papale et al., 2016)) calculated over the animal's trajectory (**Figure 3.10C**). Briefly, average trajectories for ipsi and contra sweep trials were first smoothed (Gaussian, 1 sample) and heading angle was derived. IdPhi was defined as the sum of the absolute change in heading velocity across each average trajectory, with higher values indicating greater deviations in heading. For each session, IdPhi was averaged across left and right turn trials (**Figure 3.10C**).

Quantification and statistical analysis

All analyses and statistical tests were implemented using custom Python scripts (Python version 3.8.5). Statistical tests used and p-values are provided throughout the text and in figure legends.

References

Basso, M. A., & May, P. J. (2017). Circuits for action and cognition: A view from the superior colliculus. *Annual Review of Vision Science*, *3*, 197–226.

Buzsáki, G. (1989). Two-stage model of memory trace formation: a role for "noisy" brain states. *Neuroscience*, *31*(3), 551–570.

Calalo, J. A., Ngo, T. T., Sullivan, S. R., Strand, K., Buggeln, J. H., Lokesh, R., Roth, A. M., Carter, M. J., Kurtzer, I. L., & Cashaback, J. G. A. (2025). Online movements reflect ongoing deliberation. *The Journal of Neuroscience: The Official Journal of the Society for Neuroscience*, *45*(31), e1913242025.

Campagner, D., Vale, R., Tan, Y. L., Iordanidou, P., Pavón Arocas, O., Claudi, F., Stempel, A. V., Keshavarzi, S., Petersen, R. S., Margrie, T. W., & Branco, T. (2023). A cortico-collicular circuit for orienting to shelter during escape. *Nature*, *613*(7942), 111–119.

Cazettes, F., Reato, D., Augusto, E., Steinfeld, R., Renart, A., & Mainen, Z. F. (2025). Facial expressions in mice reveal latent cognitive variables and their neural correlates. *Nature Neuroscience*, *28*(11), 2310–2318.

Clark, B. J., Hines, D. J., Hamilton, D. A., & Whishaw, I. Q. (2005). Movements of exploration intact in rats with hippocampal lesions. *Behavioural Brain Research*, *163*(1), 91–99.

Comrie, A. E., Frank, L. M., & Kay, K. (2022). Imagination as a fundamental function of the hippocampus. *Philosophical Transactions of the Royal Society of London. Series B, Biological Sciences*, *377*(1866), 20210336.

Comrie, A. E., Monroe, E. J., Kahn, A. E., Denovellis, E. L., Joshi, A., Guidera, J. A., Krausz, T. A., Berke, J. D., Daw, N. D., & Frank, L. M. (2024). Hippocampal representations of alternative possibilities are flexibly generated to meet cognitive demands. In *bioRxiv*. https://doi.org/10.1101/2024.09.23.613567

Cowen, S. L., & McNaughton, B. L. (2007). Selective delay activity in the medial prefrontal cortex of the rat: contribution of sensorimotor information and contingency. *Journal of Neurophysiology*, *98*(1), 303–316.

Craighero, L., & Rizzolatti, G. (2005). The premotor theory of attention. In *Neurobiology of Attention* (pp. 181–186). Elsevier.

Dean, P., Redgrave, P., & Westby, G. W. (1989). Event or emergency? Two response systems in the mammalian superior colliculus. *Trends in Neurosciences*, *12*(4), 137–147.

Denovellis, E. L., Gillespie, A. K., Coulter, M. E., Sosa, M., Chung, J. E., Eden, U. T., & Frank, L. M. (2021). Hippocampal replay of experience at real-world speeds. *eLife*, *10*(e64505). https://doi.org/10.7554/eLife.64505

Dorris, M. C., Paré, M., & Munoz, D. P. (1997). Neuronal activity in monkey superior colliculus related to the initiation of saccadic eye movements. *The Journal of Neuroscience: The Official Journal of the Society for Neuroscience*, *17*(21), 8566–8579.

Euston, D. R., & McNaughton, B. L. (2006). Apparent encoding of sequential context in rat medial prefrontal cortex is accounted for by behavioral variability. *The Journal of Neuroscience: The Official Journal of the Society for Neuroscience*, *26*(51), 13143–13155.

Evans, D. A., Stempel, A. V., Vale, R., Ruehle, S., Lefler, Y., & Branco, T. (2018). A synaptic threshold mechanism for computing escape decisions. *Nature*, *558*(7711), 590–594.

Felsen, G., & Mainen, Z. F. (2008). Neural substrates of sensory-guided locomotor decisions in the rat superior colliculus. *Neuron*, *60*(1), 137–148.

Felsen, G., & Mainen, Z. F. (2012). Midbrain contributions to sensorimotor decision making. *Journal of Neurophysiology*, *108*(1), 135–147.

Franklin, K. B. J., & Paxinos, G. (2007). *The mouse brain in stereotaxic coordinates* (3rd ed.). Academic Press.

Glimcher, P. W., & Sparks, D. L. (1992). Movement selection in advance of action in the superior colliculus. *Nature*, *355*(6360), 542–545.

Hasselmo, M. E. (1999). Neuromodulation: acetylcholine and memory consolidation. *Trends in Cognitive Sciences*, *3*(9), 351–359.

Hobson, J. A., Hong, C. C.-H., & Friston, K. J. (2014). Virtual reality and consciousness inference in dreaming. *Frontiers in Psychology*, *5*, 1133.

Isa, T., Marquez-Legorreta, E., Grillner, S., & Scott, E. K. (2021). The tectum/superior colliculus as the vertebrate solution for spatial sensory integration and action. *Current Biology*, *31*(11), R741–R762.

James, W. (1890). *The Principles of Psychology (Vol. 2)*. Henry Holt & Company.

Jantz, J. J., Watanabe, M., Everling, S., & Munoz, D. P. (2013). Threshold mechanism for saccade initiation in frontal eye field and superior colliculus. *Journal of Neurophysiology*, *109*(11), 2767–2780.

Jeannerod, M. (2001). Neural simulation of action: a unifying mechanism for motor cognition. *NeuroImage*, *14*(1 Pt 2), S103-9.

Johnson, A., & Redish, A. D. (2007). Neural ensembles in CA3 transiently encode paths forward of the animal at a decision point. *The Journal of Neuroscience: The Official Journal of the Society for Neuroscience*, *27*(45), 12176–12189.

Kay, K., Chung, J. E., Sosa, M., Schor, J. S., Karlsson, M. P., Larkin, M. C., Liu, D. F., & Frank, L. M. (2020). Constant sub-second cycling between representations of possible futures in the hippocampus. *Cell*, *180*(3), 552-567.e25.

Korbisch, C. C., Apuan, D. R., Shadmehr, R., & Ahmed, A. A. (2022). Saccade vigor reflects the rise of decision variables during deliberation. *Current Biology*, *32*(24), 5374-5381.e4.

LorenFrankLab. (2024). *track_linearization: 2D to 1D position linearization using HMMs*. https://github.com/LorenFrankLab/track_linearization

Masullo, L., Mariotti, L., Alexandre, N., Freire-Pritchett, P., Boulanger, J., & Tripodi, M. (2019). Genetically defined functional modules for spatial orienting in the mouse superior colliculus. *Current Biology*, *29*(17), 2892-2904.e8.

Mathis, A., Mamidanna, P., Cury, K. M., Abe, T., Murthy, V. N., Mathis, M. W., & Bethge, M. (2018). DeepLabCut: markerless pose estimation of user-defined body parts with deep learning. *Nature Neuroscience*, *21*(9), 1281–1289.

O'Keefe, J. (2025). How the hippocampal cognitive map supports flexible navigation. *Annual Review of Neuroscience*, *48*(1), 331–344.

Pachitariu, M., Sridhar, S., & Stringer, C. (2023). Solving the spike sorting problem with Kilosort. In *bioRxiv*. https://doi.org/10.1101/2023.01.07.523036

Papale, A. E. (2015). *Hippocampal Representations on the Spatial Delay Discounting Task*. University of Minnesota.

Papale, Andrew E., Zielinski, M. C., Frank, L. M., Jadhav, S. P., & Redish, A. D. (2016). Interplay between hippocampal sharp-wave-ripple events and vicarious trial and error behaviors in decision making. *Neuron*, *92*(5), 975–982.

Paré, M., & Hanes, D. P. (2003). Controlled movement processing: superior colliculus activity associated with countermanded saccades. *The Journal of Neuroscience: The Official Journal of the Society for Neuroscience*, *23*(16), 6480–6489.

Rączaszek-Leonardi, J. (2023). What dynamic approaches have taught us about cognition and what they have not: On values in motion and the importance of replicable forms. *Topics in Cognitive Science*. https://doi.org/10.1111/tops.12709

Redish, A. D. (2016). Vicarious trial and error. *Nature Reviews. Neuroscience*, *17*(3), 147–159.

Rizzolatti, G., Riggio, L., Dascola, I., & Umiltá, C. (1987). Reorienting attention across the horizontal and vertical meridians: evidence in favor of a premotor theory of attention. *Neuropsychologia*, *25*(1A), 31–40.

Schiller, P. H., & Stryker, M. (1972). Single-unit recording and stimulation in superior colliculus of the alert rhesus monkey. *Journal of Neurophysiology*, *35*(6), 915–924.

Senzai, Y., & Scanziani, M. (2024). The brain simulates actions and their consequences during REM sleep. In *bioRxiv*. https://doi.org/10.1101/2024.08.13.607810

Sharp, S. L., Shin, J., Martins, D. M., Jones, K., & Niell, C. M. (2025). Neural dynamics in superior colliculus of freely moving mice. *Cell Reports*, *44*(10), 116284.

Sparks, D., Rohrer, W. H., & Zhang, Y. (2000). The role of the superior colliculus in saccade initiation: a study of express saccades and the gap effect. *Vision Research*, *40*(20), 2763–2777.

Tang, W., Mei, X., Harvey, R. E., Carbajal-Leon, E., Netzer, T., Chang, H., Oliva, A., & Fernandez-Ruiz, A. (2025). Goal-directed hippocampal theta sweeps during memory-guided navigation. In *bioRxiv*. https://doi.org/10.1101/2025.08.26.672489

Tse, P. U. (2025). The disencapsulated mind: A premotor theory of human imagination. *Psychological Review*, *132*(4), 895–915.

Vollan, A. Z., Gardner, R. J., Moser, M.-B., & Moser, E. I. (2025). Left-right-alternating theta sweeps in entorhinal-hippocampal maps of space. *Nature*, *639*(8056), 995–1005.

Vollan, A. Z., Schellenberger, M. F., Moser, M.-B., & Moser, E. I. (2026). Attention-like regulation of theta sweeps in the brain's spatial navigation circuit. In *bioRxiv*. https://doi.org/10.64898/2026.01.27.702083

Watson, J. B. (1913). Psychology as the behaviorist views it. *Psychological Review*, *20*(2), 158–177.

Wikenheiser, A. M., & Redish, A. D. (2015). Decoding the cognitive map: ensemble hippocampal sequences and decision making. *Current Opinion in Neurobiology*, *32*, 8–15.

Wilson, J. J., Alexandre, N., Trentin, C., & Tripodi, M. (2018). Three-dimensional representation of motor space in the mouse superior colliculus. *Current Biology*, *28*(11), 1744-1755.e12.

Wurtz, R. H., & Goldberg, M. E. (1971). Superior colliculus cell responses related to eye movements in awake monkeys. *Science (New York, N.Y.)*, *171*(3966), 82–84.

Yu, C., Ji, Z., Ormond, J., O'Keefe, J., & Burgess, N. (2025). Hippocampal theta sweeps indicate goal direction. In *bioRxiv*. https://doi.org/10.1101/2025.08.21.671551

CHAPTER 4: SPATIAL MODULATION AND TRAJECTORY ENCODING IN THE SUPERIOR COLLICULUS

Introduction

Studies in primates and rodents have shown that dSC neurons fire in association with orienting movements of a specific direction and size irrespective of the initial position of the eye (Schiller & Stryker, 1972), head (Zahler et al., 2023), or body in space (**Figure 2.3B,** (Cooper et al., 1998)). Thus, orienting-related activity in the dSC appears to reflect an egocentric, displacement-based motor response.

However, Cooper et al. reported that, in rats on a radial-arm maze, some turn-selective dSC cells exhibited a clear position bias by preferentially firing during turns on some, but not all arms of the maze (Cooper et al., 1998). Furthermore, the authors noted that a large fraction of the recorded dSC neurons (42%, 53/125) fired preferentially based on either the location of the animal on the maze and/or whether the trajectory of the animal on the maze arm was inbound or outbound (Cooper et al., 1998).

These results suggest that, in addition to exhibiting turn-related firing, dSC neurons can also exhibit spatial and trajectory-related firing, similar to hippocampal place cells (Ferbinteanu & Shapiro, 2003; Frank et al., 2000; Wood et al., 2000). This chapter explores spatial and trajectory-related activity in the mouse dSC during the Y-maze task.

Results

4.1 Spatial modulation of turn-related activity in the intermediate and deep SC

While this dissertation has focused exclusively on turn cells (i.e., cells that exhibited significant firing rate modulation at the maze bifurcation consistently in the same direction regardless of which maze arm the animal came from), it is important to note that

more than 70% of the recorded dSC cells were not classified as turn cells (72%, 1060/1471). In other words, most cells in the dSC either exhibited no turn-selective firing at the maze bifurcation or exhibited turn-selective firing that depended on which maze arm the animal came from.

The distribution of response types was as follows: 18% (263/1471) showed no turn-selective firing at the maze bifurcation (**Figure 4.1A**); 25% (374/1471) showed turn-selective firing when leaving one maze arm (**Figure 4.1B**); 25%, (364/1471) showed turn-selective firing when leaving two maze arms, with most (77%, 280/364) showing selectivity in the same turn direction across both arms (**Figure 4.1C**); and 32% (470/1471) showed turn-selective firing when leaving all three maze arms, with most (87%, 411/470) showing selectivity in the same turn direction across all arms (i.e., turn cells, **Figure 4.1D**).

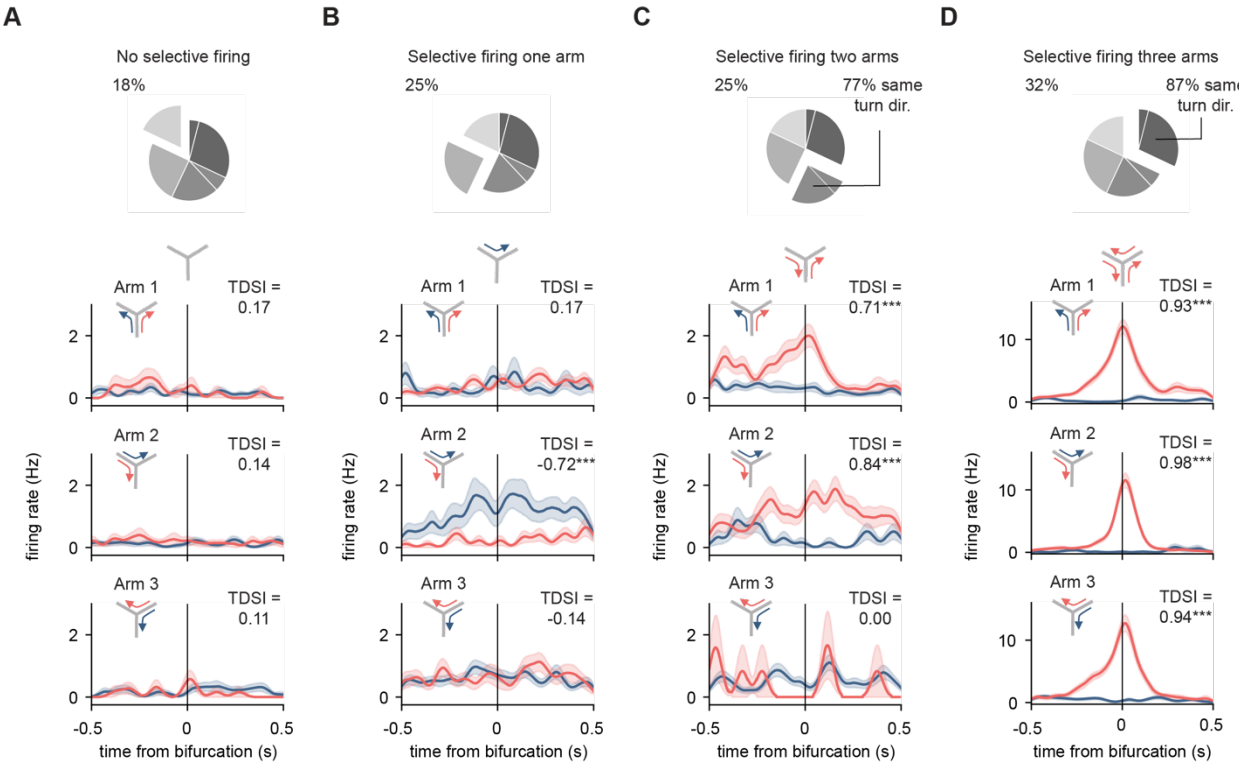

Figure 4.1 Spatial modulation of turn-related activity in the intermediate and deep SC

(Figure caption continued on the next page)

(Figure caption continued from the previous page)

(A) Example cell showing no significant turn-direction selective firing at the bifurcation leaving any of the maze arms. **(B)** Example cell showing selective firing for left turns leaving arm 2 only. **(C)** Example cell showing selective firing for right turns leaving arms 1 and 2 but not arm 3. **(D)** Example cell (same as in Figure 2.3B) showing selective firing for right turns across all maze arms. Pie charts above each panel show the fraction of the recorded population falling into each category (no selective firing, one-arm, two-arm, or three-arm selective); the wedge corresponding to the example cell's category is offset, with its percentage shown above. For (C) and (D), "% same turn dir." indicates the fraction of cells with the same turn-direction preference across arms. Example cells in (C) and (D) are taken from these fractions. All significant TDSI values: $p < 0.001$, permutation tests. Thick lines: average firing rates across trials; shaded bands: s.e.m. Y-maze above each plot represents the trajectory (or trajectories) each cell is selective for.

Thus, among cells showing significant turn-selective firing at the maze bifurcation leaving one or more maze arms (1208 cells), most exhibited firing that was modulated by the animal's starting position on the maze (67%, 807/1208).

4.2 Trajectory encoding in the intermediate and deep SC

Trajectory encoding, which has been well described in hippocampal place cells (Ferbinteanu & Shapiro, 2003; Frank et al., 2000; Wood et al., 2000) and other cortical structures (Miller et al., 2019; Shin et al., 2019; Tang et al., 2021; Vedder et al., 2017), refers to when a cell fires more in a given spatial location depending on the future trajectory of the animal. For example, when a place cell fires more on the center arm of a bifurcating maze when the animal ultimately turns left compared to right. There are clear examples of trajectory-like responses in the dSC, as in **Figure 4.1B**.

The existence of spatial modulation and trajectory-like encoding in the dSC raises the possibility that individual dSC cells may exhibit different turn direction preferences depending on which maze arm the animal came from. Indeed, among the population of cells that showed significant turn-selective firing at the maze bifurcation for two out of the three maze arms, a subset (23%, 84/364, **Figure 4.2A**) exhibited selectivity in opposite

turn directions across maze arms. In other words, these cells 'flipped' their turn direction-selectivity depending on the animal's starting position, resulting in firing that encoded either trajectories between maze arms or trajectories converging on a single arm.

Figure 4.2B shows a cell that fired selectively for trajectories between arms 2 and 3. Interestingly, unlike a turn cell, this cell exhibited increased firing across the full extent of each trajectory. **Figure 4.2C** shows a cell that fired more for trajectories that converged on arm 2. This cell also exhibited increased firing as soon as the animal started locomoting but returned to baseline after the bifurcation. Similarly, **Figure 4.2D** shows a cell that fired more for trajectories that converged on arm 3. This cell exhibited a response more like that of a turn cell, ramping up and peaking around the bifurcation.

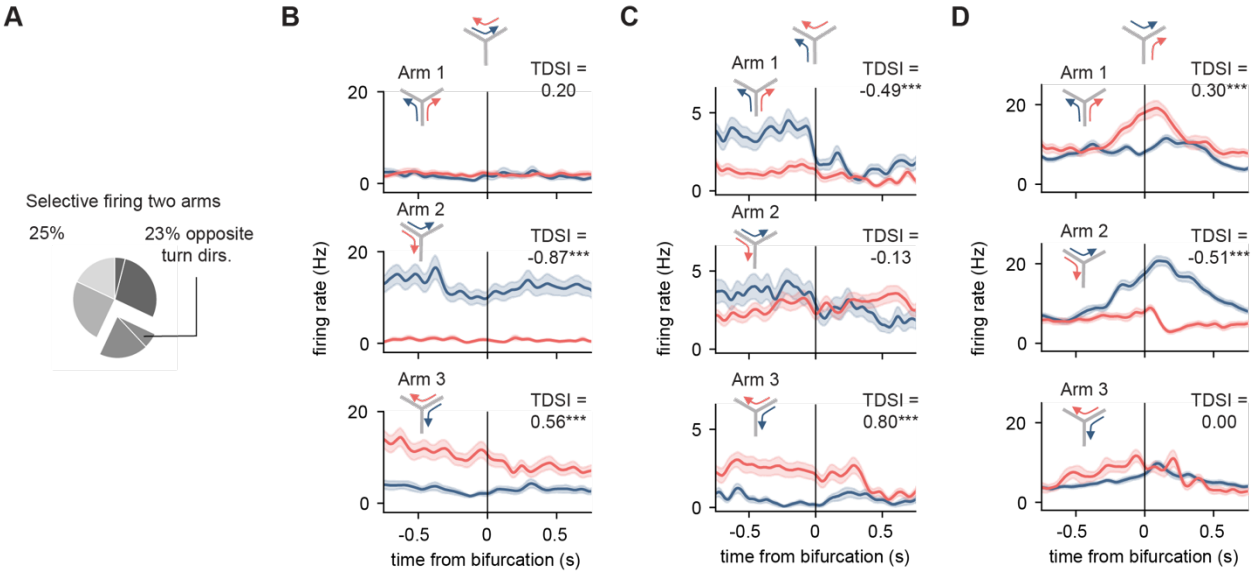

Figure 4.2 Trajectory-related modulation of intermediate and deep SC activity
(A) Pie chart showing the fraction of cells that showed selective firing leaving two out of three maze arms. "% opposite turn dirs." indicates the fraction of cells with opposite turn-direction preference across arms. Examples cells in (B), (C), and (D) are taken from this fraction. **(B)** Example cell showing selective firing for left turn trials leaving arm 2 and right turn trials leaving arm 3. **(C)** Example cell showing selective firing for left turn trials leaving arm 1 and right turn trials leaving arm 3. **(D)** Example cell showing selective firing for right turn trials leaving arm 1 and left turn trials leaving arm 2. Thick lines: average firing rates across trials, shaded bands: s.e.m. Y-maze above each plot represents the trajectories each cell is selective for. All significant TDSI values: $p < 0.001$, permutation tests.

Thus, turn-related activity in the dSC is not only spatially modulated but also shaped by aspects of the animal's trajectory as it moves through space.

Discussion

These results demonstrate that most neurons in the dSC exhibit spatially selective, trajectory-dependent firing that goes beyond simple turn direction selectivity. Rather than signaling a fixed motor output such as 'turn left' or 'turn right', these neurons appear to integrate information about the animal's current position as well as its upcoming trajectory (e.g., 'turn left if leaving arm 2', or 'fire if moving toward arm 3').

This trajectory-dependent modulation in the dSC resembles, in part, the trajectory encoding described in more 'cognitive' areas of the brain such as the hippocampus (Ferbinteanu & Shapiro, 2003; Frank et al., 2000; Wood et al., 2000), prefrontal cortex (Shin et al., 2019; Tang et al., 2021), and retrosplenial cortex (Miller et al., 2019; Vedder et al., 2017), in which a cell fires more in a given spatial location depending on the future trajectory of the animal. In addition to this type of spatial firing (**Figure 4.1B**), dSC neurons also exhibited firing that encoded trajectories between two specific maze arms or trajectories converging on a single maze arm (**Figure 4.2**), as if to represent trajectories across specific segments of the maze or toward specific goals. These results suggest that, beyond issuing simple left-right motor commands, the dSC may construct higher-order representations of where the animal is and where it is going—representations that, if coupled to motor output, could support navigation toward salient locations in space.

How might trajectory-related information arise in the dSC? One possibility is that the SC integrates spatial and trajectory-related inputs from the hippocampus (**Chapter 4**) or retrosplenial cortex (Campagner et al., 2023). Another, more parsimonious,

explanation could be that the observed trajectory-related firing reflects an intrinsic property of the SC. In particular, the dSC has been shown to encode distance to target (i.e., endpoint), rather than displacement (Bergeron et al., 2003; Zahler et al., 2023). Thus, trajectory-dependent firing in the dSC, particularly when it converges toward a single goal location (**Figure 4.1B**, **4.2C** and **4.2D**), may simply reflect the encoding of a spatial target.

In summary, while dSC neurons have been shown to primarily reflect an egocentric, displacement-based motor response, they can also exhibit activity that depends on the animal's initial position on the maze and its upcoming trajectory. Strikingly, dSC neurons can encode trajectories that converge on a single goal arm, analogous to target encoding previously described in the dSC (Bergeron et al., 2003; Zahler et al., 2023). Together, these results suggest that basic forms of spatial and trajectory-dependent activity are already present at the level of the SC, a sensorimotor midbrain structure that is highly conserved across vertebrates. It has been suggested that primitive encoding of spatial information in sensorimotor circuits may have "prepared the way" for the emergence of more abstract spatial representations in cognitive structures (Paillard, 1987, 1991). Understanding the relationship between spatially-modulated activity in sensorimotor structures and spatial representations in cognitive systems is an important direction for future work.

Methods

All methods from this chapter are the same as described in **Chapters 2** and **3**.

References

Bergeron, A., Matsuo, S., & Guitton, D. (2003). Superior colliculus encodes distance to target, not saccade amplitude, in multi-step gaze shifts. *Nature Neuroscience*, *6*(4), 404–413.

Campagner, D., Vale, R., Tan, Y. L., Iordanidou, P., Pavón Arocas, O., Claudi, F., Stempel, A. V., Keshavarzi, S., Petersen, R. S., Margrie, T. W., & Branco, T. (2023). A cortico-collicular circuit for orienting to shelter during escape. *Nature*, *613*(7942), 111–119.

Cooper, B. G., Miya, D. Y., & Mizumori, S. J. (1998). Superior colliculus and active navigation: role of visual and non-visual cues in controlling cellular representations of space. *Hippocampus*, *8*(4), 340–372.

Ferbinteanu, J., & Shapiro, M. L. (2003). Prospective and retrospective memory coding in the hippocampus. *Neuron*, *40*(6), 1227–1239.

Frank, L. M., Brown, E. N., & Wilson, M. (2000). Trajectory encoding in the hippocampus and entorhinal cortex. *Neuron*, *27*(1), 169–178.

Miller, A. M. P., Mau, W., & Smith, D. M. (2019). Retrosplenial cortical representations of space and future goal locations develop with learning. *Current Biology*, *29*(12), 2083-2090.e4.

Paillard, J. (1987). Cognitive Versus Sensorimotor Encoding of Spatial Information. In P. Ellen (Ed.), *Cognitive Processes and Spatial Orientation in Animal and Man* (pp. 43–77). Springer Netherlands.

Paillard, J. (1991). Motor and representational framing of space. In J. Paillard (Ed.), *Brain And Space* (pp. 163–182). Oxford University PressOxford.

Schiller, P. H., & Stryker, M. (1972). Single-unit recording and stimulation in superior colliculus of the alert rhesus monkey. *Journal of Neurophysiology*, *35*(6), 915–924.

Shin, J. D., Tang, W., & Jadhav, S. P. (2019). Dynamics of awake hippocampal-prefrontal replay for spatial learning and memory-guided decision making. *Neuron*, *104*(6), 1110-1125.e7.

Tang, W., Shin, J. D., & Jadhav, S. P. (2021). Multiple time-scales of decision-making in the hippocampus and prefrontal cortex. *eLife*, *10*(e66227). https://doi.org/10.7554/eLife.66227

Vedder, L. C., Miller, A. M. P., Harrison, M. B., & Smith, D. M. (2017). Retrosplenial cortical neurons encode navigational cues, trajectories and reward locations during goal directed navigation. *Cerebral Cortex (New York, N.Y.: 1991)*, *27*(7), 3713–3723.

Wood, E. R., Dudchenko, P. A., Robitsek, R. J., & Eichenbaum, H. (2000). Hippocampal neurons encode information about different types of memory episodes occurring in the same location. Neuron, 27(3), 623–633.

Zahler, S. H., Taylor, D. E., Wright, B. S., Wong, J. Y., Shvareva, V. A., Park, Y. A., & Feinberg, E. H. (2023). Hindbrain modules differentially transform activity of single collicular neurons to coordinate movements. *Cell*, *186*(14), 3062-3078.e20.

CHAPTER 5: CONCLUSIONS AND DISCUSSION

Dissertation summary

The superior colliculus (SC) is a conserved sensorimotor midbrain structure that has long been implicated in the control of orienting movements. However, despite decades of work, it is not yet clear how neural activity in this structure unfolds during freely-moving, internally-driven behaviors like spatial navigation, when orienting movements need to be coordinated with other ongoing behavioral and cognitive processes. The studies reported in this dissertation have added the following items to our knowledge of SC physiology during freely-moving, internally generated behaviors:

1) In mice performing a Y-maze spatial navigation task, about 30% of neurons in the intermediate and deep layers of the SC (dSC) increase their firing when the animal turns either left or right at the maze bifurcation regardless of which maze arm the animal comes from (left- or right-preferring 'turn cells').
2) Turn cells fire primarily for contraversive turns and become directionally selective before the animal's behavior diverges between left and right turns.
3) Peak activity in turn cells propagates posteriorly along the anteroposterior axis of the SC as the animal proceeds through the turn.
4) Turn cell activity is rhythmically modulated during locomotion, firing in-phase with the ongoing stepping cycle of the animal, such that left and right turn cells fire at opposite phases of the stepping cycle.
5) Turn cell activity is modulated in directional coordination with hippocampal representations of possible future paths (hippocampal sweeps).
6) Hippocampal sweeps predict subsequent turn cell activity.

7) Consistent with an influence of hippocampal sweeps on turn cell activity, sweeps are associated with biases in the animal's trajectory toward the represented path.
8) Beyond turn cells, the remaining ~70% of neurons in the dSC either exhibit no turn-selective firing at the maze bifurcation or exhibit turn-selective firing that depends on the animal's starting position on the maze and its upcoming trajectory.
9) Neurons in the dSC can exhibit firing that encodes trajectories between two specific maze arms or trajectories converging on a single maze arm.

Thus, during navigation, neural activity in the motor layers of the SC reflects not only multiple aspects of ongoing behavior—such as turns, steps, and trajectories—but also ongoing cognitive processes, such as mental simulations of possible futures. How might these data fit with proposed theories of SC function, and what might they reveal about the relationship between thought and action?

5.1 The SC as a movement template

In 1970, K.P. Schaefer published a report detailing a series of SC stimulation experiments in rabbits and cats. Schaefer found that, while brief stimulation of the SC elicited discrete eye movements, prolonged stimulation of the SC elicited a sequence of orienting movements involving the ears, head, body, and limbs (Schaefer, 1970). In the same issue, Ingle and Ewert reported similar findings in frogs and toads (Ewert, 1970; Ingle, 1970). Reflecting on these results, Schaefer writes:

> Thus, we interpret the function of the optic tectum in terms of a multimodal 'movement template' which is organized as an entire sequence of goal-directed movements. In this respect, the tectum of the rabbit or cat is very similar to that of the frog or toad, as discussed by Ingle and Ewert in this conference. In agreement with these workers, we believe that the movement-schemata of the tectum are used by higher brain centers for 'intentional' actions, as well as for quick reflexive moments (Schaefer, 1970).

The interpretation that the SC is organized as an entire sequence of goal-directed movements could explain many of the responses observed in the dSC during navigation. Indeed, turns, steps, and trajectories reflect various components, or levels of organization, of a larger movement sequence through space. In this view, the SC plays a role not only in generating discrete orienting movements, but also in integrating them into coordinated sequences of action—like turning while stepping.

Our data also support the idea that these action sequences can be used by higher brain centers for intentional, planned actions. **Chapter 3** shows that hippocampal representations of possible future paths predict turn-related activity in the dSC that guides the animal toward those paths, suggesting that such representations are transmitted to the dSC to bias turning actions. Thus, we speculate that the hippocampal navigation system imposes directional biases on dSC activity, thereby steering ongoing action sequences along planned trajectories.

In summary, Schaefer's interpretation that the SC functions as a movement template captures many of the responses observed in the dSC during navigation, including the encoding of turns, steps, and trajectories. Furthermore, our results suggesting that the hippocampal sweeps bias SC activity to guide turns is consistent with Schaefer's idea that higher brain systems use the SC movement template for intentional actions.

5.2 Thought and action

Chapter 3 shows that when the brain simulates a possible future path, it also engages motor commands that actively guide the animal toward that path. Remarkably,

this occurs even when the simulated path is not ultimately taken, as if the mere thought of a possible future triggers the animal to move toward it.

It has long been suggested that the mere idea of a movement automatically triggers the movement itself. In 1852, William B. Carpenter, writing on the subject of hypnosis, proposed that, just as sensations can evoke movements, 'there is no *a priori* difficulty in believing that *Ideas* may become the sources of muscular movement' (Carpenter, 1852). Carpenter coined the term 'ideo-motor' action, which refers to an action being triggered directly from an idea (Carpenter, 1852). This raises an important question: what does Carpenter mean by an 'idea'?

An idea is merely 'the anticipation of a given result,' which acts as a stimulus that directly prompts the muscular movements that produce that result (Carpenter, 1852). In this way, the anticipated consequences of a movement directly bring about the movement itself.

Carpenter's ideo-motor principle was notably favored by William James at the end of the 19th century. James wrote in *Principles of Psychology Vol. II*, 'We think the act, and it is done' (James, 1890). For James, every idea of a movement automatically 'awakens' the movement itself:

> We may lay it down for certain that every representation of a movement awakens in some degree the actual movement which is its object; and awakens it in a maximum degree whenever it is not kept from so doing by an antagonistic representation present simultaneously to the mind (James, 1890).

In other words, when there are no antagonistic thoughts, 'there is naturally no hiatus between the thought process and the motor discharge' (James, 1890). Thus, in agreement with Carpenter, James holds that the mere idea of a movement, defined as

‘the anticipation of the movement’s sensible effects’ (James, 1890), automatically triggers the movement itself.

A natural consequence of the ideo-motor principle is that all higher-order thought processes are expressed in terms of muscular movements, however faint. James addresses this beautifully:

> A waking man's behavior is thus at all times the resultant of two opposing neural forces. With unimaginable fineness some currents among the cells and fibres of his brain are playing on his motor nerves, whilst other currents, as unimaginably fine, are playing on the first currents, damming or helping them, altering their direction or their speed. The upshot of it all is, that whilst the currents must always end by being drained off through some motor nerves, they are drained off sometimes through one set and sometimes through another; and sometimes they keep each other in equilibrium so long that a superficial observer may think they are not drained off at all. Such an observer must remember, however, that from the physiological point of view a gesture, an expression of the brow, or an expulsion of the breath are movements as much as an act of locomotion is. A king's breath slays as well as an assassin's blow; and the outpouring of those currents which the magic imponderable streaming of our ideas accompanies need not always be of an explosive or otherwise physically conspicuous kind (James, 1890).

Thus, the ideo-motor principle predicts that all higher thought processes, including those that occur during dreams (Max, 1935; Shimizu & Inoue, 1986), go on in terms of faint reinstatements of overt motor acts (Bain, 1855; Watson, 1913).

Importantly, the ideo-motor principle is related to several other action-based views of cognition (Buzsáki et al., 2014; Craighero & Rizzolatti, 2005; Jeannerod, 2001; McNaughton et al., 1996; Tse, 2025), which hold that thought and movement are deeply intertwined. James anticipates these views vividly:

> Every pulse of feeling which we have is the correlate of some neural activity that is already on its way to instigate a movement. Our sensations and thoughts are but cross-sections, as it were, of currents whose essential consequence is motion (James, 1890).

The results presented in **Chapter 3** of this dissertation are consistent with the ideo-motor principle on several accounts. First, hippocampal sweeps can be seen as 'ideas' in the sense of Carpenter and James, in that they encode the *anticipated* spatial consequences of taking particular paths. Second, according to the ideo-motor principle, these ideas are expressed in terms of muscular activity, however faint. In line with this view, when the hippocampus represents a possible future path that is not ultimately taken, the animal's trajectory is nonetheless biased, however subtly, toward that path (**Figure 3.10**). This demonstrates that animals turn toward possible futures that are represented but not selected, possibly reflecting hippocampal biasing of dSC motor commands. Of note, this finding is consistent with numerous studies showing similar 'leakage' of cognitive processes into overt movements during awake behavior and sleep (Calalo et al., 2025; Cazettes et al., 2025; Cowen & McNaughton, 2007; Euston & McNaughton, 2006; Korbisch et al., 2022; Max, 1935; Shimizu & Inoue, 1986). Thus, we speculate that, by engaging dSC activity, hippocampal representations of possible futures (i.e., hippocampal 'ideas') automatically trigger orienting movements toward those futures, in agreement with the ideo-motor principle of action (Carpenter, 1852; James, 1890).

5.3 The SC as an ideo-motor transformation area

The SC has long been established as a sensorimotor structure critical for visually-guided orienting behaviors. Given its visuo-motor map, inputs from specific locations in visual space trigger reflexive orienting movements toward those locations. We propose that, similarly, cognitive inputs to the SC concerning possible or intended future locations may trigger reflexive orienting movements toward those locations. Thus, mirroring its role in visuo-motor processes, the SC may function as an *ideo-motor* reflex structure which

transforms cognitive inputs about intended locations into orienting movements toward those locations.

It is interesting to note that Carpenter initially characterized ideo-motor action as a 'form of reflex' (Carpenter, 1852) and that Ingle viewed the tectal orienting response as a highly stereotyped, reflexive movement sequence (Ingle, 1970). Ingle remarks:

> The efferent role of the tectum seems highly stereotyped, like that of a well-wrought music box from which a few precise melodies can be elicited by setting the correct switches. A large part of the complex 'wiring system' within the tectum probably has more to do with sensory integration, and with inter-tectal or thalamo-tectal modulation than with organization of the response sequence itself (Ingle, 1970).

Thus, the SC generates sequences of highly stereotyped, reflexive movements. We speculate that mental simulations of possible futures, such as hippocampal sweeps, may be transmitted to the dSC to trigger reflexive orienting movements toward those futures. In this way, the tectal orienting response can be 'triggered from above' (Schaefer, 1972), consistent with a role for the SC in transforming ideas into action.

5.4 Outstanding questions

1) Do locomotor rhythmic cells in the dSC constitute a distinct cell-type with specific connectivity patterns?
2) What is the source of stepping-related modulation in the dSC?
3) Do changes in phase-locking strength or phase offset among locomotor rhythmic cells correspond to changes in behavior (i.e., changes in turns, steps, or their coordination)?
4) Our results suggest that hippocampal sweeps preferentially bias dSC activity during navigation. Are there specific times during training or task

performance where sweeps more strongly engage the dSC? Conversely, are there conditions under which dSC activity biases hippocampal sweeps?

5) Like visual inputs, do cognitive inputs ‘map’ onto specific regions or hemispheres of the dSC? How are these inputs integrated to trigger the appropriate orienting response?
6) Sweeps are expressed across multiple regions of the hippocampal-entorhinal network. Do sweeps in these regions also coordinate with ongoing dSC activity?
7) Can the ideo-motor principle be tested experimentally? For example, can internal representations be selectively evoked to automatically trigger orienting movements?

References

Bain, A. (1855). *The senses and the intellect*. John W Parker & Son, West Strand.

Buzsáki, G., Peyrache, A., & Kubie, J. (2014). Emergence of cognition from action. *Cold Spring Harbor Symposia on Quantitative Biology*, *79*, 41–50.

Calalo, J. A., Ngo, T. T., Sullivan, S. R., Strand, K., Buggeln, J. H., Lokesh, R., Roth, A. M., Carter, M. J., Kurtzer, I. L., & Cashaback, J. G. A. (2025). Online movements reflect ongoing deliberation. *The Journal of Neuroscience: The Official Journal of the Society for Neuroscience*, *45*(31), e1913242025.

Carpenter, W. B. (1852). On the influence of suggestion in modifying and directing muscular movement, independently of volition. *Royal Institution of Great Britain*.

Cazettes, F., Reato, D., Augusto, E., Steinfeld, R., Renart, A., & Mainen, Z. F. (2025). Facial expressions in mice reveal latent cognitive variables and their neural correlates. *Nature Neuroscience*, *28*(11), 2310–2318.

Cowen, S. L., & McNaughton, B. L. (2007). Selective delay activity in the medial prefrontal cortex of the rat: contribution of sensorimotor information and contingency. *Journal of Neurophysiology*, *98*(1), 303–316.

Craighero, L., & Rizzolatti, G. (2005). The premotor theory of attention. In *Neurobiology of Attention* (pp. 181–186). Elsevier.

Euston, D. R., & McNaughton, B. L. (2006). Apparent encoding of sequential context in rat medial prefrontal cortex is accounted for by behavioral variability. *The Journal of Neuroscience: The Official Journal of the Society for Neuroscience*, *26*(51), 13143–13155.

Ewert, J. P. (1970). Neural mechanisms of prey-catching and avoidance behavior in the toad (Bufo bufo L.). *Brain, Behavior and Evolution*, *3*(1), 36–56.

Ingle, D. (1970). Visuomotor functions of the frog optic tectum. *Brain, Behavior and Evolution*, *3*(1), 57–71.

James, W. (1890). *The Principles of Psychology (Vol. 2)*. Henry Holt & Company.

Jeannerod, M. (2001). Neural simulation of action: a unifying mechanism for motor cognition. *NeuroImage*, *14*(1 Pt 2), S103-9.

Korbisch, C. C., Apuan, D. R., Shadmehr, R., & Ahmed, A. A. (2022). Saccade vigor reflects the rise of decision variables during deliberation. *Current Biology*, *32*(24), 5374-5381.e4.

Max, L. W. (1935). An experimental study of the motor theory of consciousness. III. Action-current responses in deaf-mutes during sleep, sensory stimulation and dreams. *Journal of Comparative Psychology*, *19*(3), 469–486.

McNaughton, B. L., Barnes, C. A., Gerrard, J. L., Gothard, K., Jung, M. W., Knierim, J. J., Kudrimoti, H., Qin, Y., Skaggs, W. E., Suster, M., & Weaver, K. L. (1996). Deciphering the hippocampal polyglot: the hippocampus as a path integration system. *The Journal of Experimental Biology*, *199*(Pt 1), 173–185.

Schaefer, K. P. (1970). Unit analysis and electrical stimulation in the optic tectum of rabbits and cats. *Brain, Behavior and Evolution*, *3*(1), 222–240.

Schaefer, K. P. (1972). Neuronal elements of the orienting response. Microrecordings and stimulation experiments in rabbits. *Bibliotheca Ophthalmologica: Supplementa Ad Ophthalmologica*, *82*, 139–148.

Shimizu, A., & Inoue, T. (1986). Dreamed speech and speech muscle activity. *Psychophysiology*, *23*(2), 210–214.

Tse, P. U. (2025). The disencapsulated mind: A premotor theory of human imagination. *Psychological Review*, *132*(4), 895–915.

Vollan, A. Z., Gardner, R. J., Moser, M.-B., & Moser, E. I. (2025). Left-right-alternating theta sweeps in entorhinal-hippocampal maps of space. *Nature*, *639*(8056), 995–1005.

Watson, J. B. (1913). Psychology as the behaviorist views it. *Psychological Review*, *20*(2), 158–177.

Publishing Agreement

It is the policy of the University to encourage open access and broad distribution of all theses, dissertations, and manuscripts. The Graduate Division will facilitate the distribution of UCSF theses, dissertations, and manuscripts to the UCSF Library for open access and distribution. UCSF will make such theses, dissertations, and manuscripts accessible to the public and will take reasonable steps to preserve these works in perpetuity.

I hereby grant the non-exclusive, perpetual right to The Regents of the University of California to reproduce, publicly display, distribute, preserve, and publish copies of my thesis, dissertation, or manuscript in any form or media, now existing or later derived, including access online for teaching, research, and public service purposes.

DocuSigned by:
Cameron Willhite
B5069A020EC848C...
Author Signature

05/29/2026
Date